

A numerical study of vector resonant relaxation

Bence Kocsis^{1*} and Scott Tremaine^{1†}

¹ *Institute for Advanced Study, Princeton, NJ 08540, USA*

Received —

ABSTRACT

Stars bound to a supermassive black hole interact gravitationally. Persistent torques acting between stellar orbits lead to the rapid resonant relaxation of the orbital orientation vectors (“vector” resonant relaxation) and slower relaxation of the eccentricities (“scalar” resonant relaxation), both at rates much faster than two-body or non-resonant relaxation. We describe a new parallel symplectic integrator, N-RING, which follows the dynamical evolution of a cluster of N stars through vector resonant relaxation, by averaging the pairwise interactions over the orbital period and periapsis-precession timescale. We use N-RING to follow the evolution of clusters containing over 10^4 stars for tens of relaxation times. Among other results, we find that the evolution is dominated by torques among stars with radially overlapping orbits, and that resonant relaxation can be modelled as a random walk of the orbit normals on the sphere, with angular step size ranging from ~ 0.5 –1 radian. The relaxation rate in a cluster with a fixed number of stars is proportional to the RMS mass of the stars. The RMS torque generated by the cluster stars is reduced below the torque between Kepler orbits due to apsidal precession and declines weakly with the eccentricity of the perturbed orbit. However since the angular momentum of an orbit also decreases with eccentricity, the relaxation rate is approximately eccentricity-independent for $e \lesssim 0.7$ and grows rapidly with eccentricity for $e \gtrsim 0.8$. We quantify the relaxation using the autocorrelation function of the spherical multipole moments; this decays exponentially and the e -folding time may be identified with the vector resonant relaxation timescale.

Key words: Galaxy: centre – Galaxy: nucleus – celestial mechanics

1 INTRODUCTION

Most galaxies harbour a supermassive black hole (SMBH) of mass 10^6 – $10^{10} M_\odot$ at their centres. The SMBH is typically surrounded by a dense stellar system, which is sometimes a distinct cluster and sometimes a smooth inward continuation from larger radii of the galaxy’s stellar distribution.

We focus in this paper on the near-Keplerian region where the gravitational force is dominated by the SMBH. The dynamical behavior of the stars in this region involves the following processes (e.g., Kocsis & Tremaine 2011, hereafter KT11). (i) To a first approximation, the stars follow eccentric Keplerian orbits with orbital periods $P = 1$ – 10^4 yr (for the sake of concreteness, all numerical estimates are for the near-Keplerian region of the Milky Way between 0.001 pc and ~ 1 pc of the central black hole at Sgr A*). (ii) On longer timescales, 10^3 – 10^5 yr, the spherical component of the gravitational field from the stellar system and relativistic effects lead to apsidal precession (retrograde and prograde,

respectively) of the stellar orbits. (iii) Non-spherical components of the gravitational field from the stellar system lead to diffusion in the orientation of the orbits on even longer timescales, 10^5 – 10^7 yr. (iv) Non-axisymmetric torques between individual stellar orbits lead to diffusion of the eccentricities of the orbits on timescales of 10^7 – 10^{10} yr. Processes (iii) and (iv) are called vector and scalar resonant relaxation, respectively (Rauch & Tremaine 1996). (v) Finally, the semimajor axes diffuse due to two-body encounters and dynamical friction on timescales $\gtrsim 10^9$ yr. A review of these and other dynamical processes in galactic nuclei is given in Merritt (2013).

A rough guide to the relevant timescales is obtained by considering a cluster of $N \gg 1$ stars of mass m surrounding a central mass M_\bullet , with $Nm \ll M_\bullet$. If the typical orbital radius is a and the corresponding orbital period is $P = 2\pi(a^3/GM_\bullet)^{1/2}$, then

* bkocsis@ias.edu
† tremaine@ias.edu

- the apsidal precession time is $\sim P M_{\bullet}/(Nm)$;
- the orbital planes are re-oriented on the vector resonant relaxation timescale, $\sim P M_{\bullet}/(m\sqrt{N})$;
- the eccentricities are re-distributed on the scalar resonant relaxation timescale, $\sim P M_{\bullet}/m$;
- the semimajor axes diffuse on the two-body or non-resonant relaxation timescale, $\sim P M_{\bullet}^2/(m^2N)$.

The large number of stars ($\sim 10^7$) and vast range of spatial and temporal scales (10^{-6} – 1 pc and 10 – 10^{10} yr), as well as the long-range spatial and temporal correlations of the forces involved in resonant relaxation, prohibit the accurate dynamical modeling of these environments with the tools used for stellar clusters, namely Fokker–Planck calculations and direct N-body integrations. However, the hierarchy of timescales in near-Keplerian stellar systems leads to adiabatic invariants, and algorithms that enforce their conservation can increase numerical accuracy and decrease computational demands. For example, by averaging over timescales long compared to the orbital period but short compared to the apsidal precession timescale, we obtain Gauss’s method for secular dynamics (Touma et al. 2009), in which each body on an eccentric orbit is replaced by a “wire” on which the linear density is proportional to the corresponding residence time, i.e., inversely proportional to the velocity. On even longer timescales, we can average the wires over the apsidal precession timescale and thereby represent them with annuli. Since these structures are stationary and axisymmetric, the energy and magnitude of the angular momentum of a stellar orbit are conserved but the direction of the angular momentum is not; in other words the geometry of the annulus (periapsis, apoapsis, and surface density) is fixed, but its orientation is not. Vector resonant relaxation (hereafter VRR) is the stochastic process arising from the gravitational interaction of these annuli, leading to relaxation of their orientations.

Here we describe a new symplectic integrator, N-RING, which follows VRR in near-Keplerian stellar systems. First, we derive the surface density of the annulus describing an eccentric stellar orbit by averaging over orbital phase and apsidal angle. Next we derive the corresponding secular Hamiltonian describing the interaction between a pair of stars. The resulting equations of motion for a pair of stars can be solved analytically. We construct a symplectic integrator by combining the effects of the pairwise interactions. We parallelize, refine, and optimize the algorithm by evaluating independent pairs in parallel, and by evaluating the strongest interactions with a smaller timestep than the weaker ones.

We use N-RING to study VRR in spherical near-Keplerian stellar systems containing up to 16k stars. We measure the temporal correlation function of the orbit normals and determine the timescales for relaxation and complete mixing as a function of the semimajor axis, eccentricity, and stellar mass distributions. We construct a simple model of the relaxation process as a Markovian random walk on a sphere and show that this provides a good representation of the numerical results. We also provide empirical formulae that can be used to estimate the VRR timescale in spherical systems.

2 SECULAR EVOLUTION

2.1 Hamiltonian for vector resonant relaxation

We consider a system of N stars, of masses m_i with $i \in \{1, 2, \dots, N\}$, orbiting an SMBH of mass M_{\bullet} located at the origin. We denote the Keplerian orbit by $\mathbf{r}_i(t)$ and the semimajor axis, eccentricity, and period by a_i , e_i , and $P_i \equiv 2\pi/\Omega_i$ with $\Omega_i \equiv (GM_{\bullet}/a_i^3)^{1/2}$. We make the following assumptions:

- (i) the mass in stars is much less than the mass of the SMBH, $\sum_i m_i \ll M_{\bullet}$, although the number of stars $N \gg 1$;
- (ii) there are no binaries (although binaries with semimajor axes much less than the system size can be treated as single stars over the timescales considered here);
- (iii) the stellar system is sufficiently far from the SMBH that each star follows an approximately Keplerian orbit around the SMBH;
- (iv) the apsidal precession time of each orbit is much longer than the longest orbital period in the stellar system;
- (v) the apsidal precession time of each orbit is much shorter than the shortest orbital plane re-orientation time¹;
- (vi) all orbital and apsidal precession periods are incommensurate, so mean-motion and apsidal secular resonances do not play a role;
- (vii) the Newtonian potential of the stellar cluster is the main driver of the re-orientation of orbital planes, as opposed to either Lense–Thirring precession or a massive perturber (e.g., a second black hole, a galactic bar, or a molecular torus).

These assumptions may be satisfied for most stars and compact objects between ~ 0.001 and ~ 0.2 pc in the Galactic center on timescales 10^5 – 10^7 yr (see KT11). In particular, assumption (i) requires that the apoapsides $r_{a,i} = a_i(1 + e_i)$ are much smaller than the radius 1.8 pc where the SMBH mass equals the enclosed stellar mass. The expected binary fraction in galactic nuclei, assumption (ii), is quite uncertain (Alexander et al. 2008; Hopman 2009), but a recent study suggests that $30_{-21}^{+34}\%$ of massive young stars in the Galactic centre may be in binaries (Pfuhl et al. 2014). Assumption (iii) requires that the periapsides $r_{p,i} = a_i(1 - e_i)$ are much larger than the gravitational radius $r_g = GM_{\bullet}/c^2 = 2 \times 10^{-7}$ pc. Assumption (iv) is valid for stars with semimajor axes $\lesssim 1$ pc (see Fig. 1 of KT11). Assumption (v) is generally valid for stars with semimajor axes $\lesssim 1$ pc, except in a narrow range of radii where the prograde general-relativistic apsidal precession cancels the retrograde Newtonian precession, in particular $a(1 - e^2)^{0.54} \simeq 7$ mpc (see

¹ This assumption fails for a small fraction of stars with eccentricity very close to unity, since the angular momentum goes to zero as $e \rightarrow 1$ so even a tiny torque will rapidly re-orient the orbit. More precisely, the apsidal precession rates due to the mean mass distribution and due to general relativity vary as $(1 - e^2)^{1/2}$ and $(1 - e^2)^{-1}$ respectively, while the re-orientation rates due to VRR and due to Lense–Thirring precession vary as $(1 - e^2)^{-1/2}$ and $(1 - e^2)^{-3/2}$.

Merritt et al. 2010; Bar-Or & Alexander 2014, KT11, and Eq. A5 with $s = 1$). Orbits outside this narrow range of radii approximately conserve their eccentricity; during one VRR timescale $\Delta e \sim (t_{\text{VRR}}/t_{\text{RR}})^{1/2} \sim N^{-1/4}$. As for assumption (vii), Lense–Thirring precession is negligible if $r_{p,i}$ is much larger than the rotational influence radius $r_r = [4\chi M_\bullet / (m_{\text{RMS}} \sqrt{N})]^{2/3} r_g \sim 1 \chi^{2/3} \text{ mpc}$ where $0 < \chi < 1$ is the dimensionless spin parameter of the SMBH (see Merritt et al. 2010, Fig. 1 of KT11, and Merritt & Vasiliev 2012). The most prominent known massive perturber in the Galactic Centre is the molecular torus at radii 1.5–7 pc, whose influence is significant outside of ~ 0.2 pc (see KT11 and references therein).

The Keplerian orbits evolve slowly due to the gravitational forces from the other stars. To follow this evolution we first average the gravitational interaction potential between stars i and j over the orbital periods of both stars². This average is

$$\begin{aligned} H_{\text{RR}}^{(ij)} &\equiv \left\langle -\frac{Gm_i m_j}{\|\mathbf{r}_i(t) - \mathbf{r}_j(t')\|} \right\rangle_{t,t'} \\ &= -\frac{1}{P_i P_j} \oint d\mathbf{r}_i \oint d\mathbf{r}_j \frac{Gm_i m_j}{v_i v_j \|\mathbf{r}_i - \mathbf{r}_j\|} \end{aligned} \quad (1)$$

where the subscript “RR” stands for “resonant relaxation” and

$$v = \|\dot{\mathbf{r}}\| = \sqrt{GM_\bullet \left(\frac{2}{\|\mathbf{r}\|} - \frac{1}{a} \right)} \quad (2)$$

is the speed. The integrations run over the Keplerian elliptical trajectories. The interaction energy is that of two elliptical wires with linear density $m/(Pv)$.

We assume that the stellar system is approximately spherical. Then its dominant effect on the orbit of an individual star is apsidal precession. The characteristic precession time is approximately $t_{\text{prec}} = 2\pi \|\boldsymbol{\Omega}_{\text{prec}}\|^{-1} \approx \Omega / [G\rho(a)]$, where $\rho(a)$ is the average stellar mass density in the vicinity of the orbit (see Appendix A). We next average the interaction Hamiltonian $H_{\text{RR}}^{(ij)}$ over the apsidal precession period t_{prec} , so the eccentric wires are replaced by axisymmetric rings or annuli. For each star the mass between radii r and $r + dr$ is $dm = 2m dr / (P|v_r|)$ where v_r is the radial component of the Keplerian velocity. Using $|v_r| = (v^2 - v_\theta^2)^{1/2}$ and the conservation of angular momentum $L = mrv_\theta = m\sqrt{GM_\bullet a(1 - e^2)}$, the surface density becomes

$$\sigma(r) = \frac{dm}{2\pi r dr} = \frac{m}{2\pi^2 a \sqrt{(r_a - r)(r - r_p)}} \quad (3)$$

if $r_p \leq r \leq r_a$ and $\sigma(r) = 0$ otherwise; here $r_a = a(1 + e)$, $r_p = a(1 - e)$ are the apoapsis and periapsis of the orbit. Thus,

$$H_{\text{RR}}^{(ij)} = - \int d\mathbf{r} \int d\mathbf{r}' \frac{G\sigma_i(r)\sigma_j(r')}{\|\mathbf{r} - \mathbf{r}'\|}, \quad (4)$$

where the integration is over the annular surfaces swept out by the rotating ellipses in the range $r_{p,i} \leq r \leq r_{a,i}$ and $r_{p,j} \leq r' \leq r_{a,j}$.

² Note that because of this orbit averaging the net force on the SMBH is zero, so it remains at rest at the origin in this approximation.

We evaluate the integral using a multipole expansion in Appendix B to find (Eqs. B7, B9, B10, and B12)

$$H_{\text{RR}}^{(ij)} = -\frac{Gm_i m_j}{a_{\text{out}}} \sum_{\ell=0}^{\infty} P_\ell(0)^2 s_{ij\ell} \alpha_{ij}^\ell P_\ell(\cos I_{ij}). \quad (5)$$

where I_{ij} is the inclination angle between the orbital planes of star i and j , $P_\ell(x)$ is a Legendre polynomial, and in particular for integer $n \geq 0$

$$P_{2n}(0) = (-1)^n \frac{(2n)!}{2^{2n} (n!)^2}, \quad P_{2n+1}(0) = 0. \quad (6)$$

Furthermore (Eqs. B12, B39)

$$\begin{aligned} s_{ij\ell} &= \frac{1}{\pi^2} \int_0^\pi d\phi \int_0^\pi d\phi' \\ &\times \frac{\min[(1 + e_{\text{in}} \cos \phi), \alpha_{ij}^{-1} (1 + e_{\text{out}} \cos \phi')]}{\max[\alpha_{ij} (1 + e_{\text{in}} \cos \phi), (1 + e_{\text{out}} \cos \phi')]^\ell} \end{aligned} \quad (7)$$

where “out” and “in” label the index i or j with the larger and the smaller semimajor axis, respectively, and $\alpha_{ij} = a_{\text{in}}/a_{\text{out}} < 1$. In Appendix B we show that one of the two integrals in Eq. (7) can be evaluated analytically and we use this result to derive a generating function of $s_{ij\ell}$. Analytic closed expressions are available in special cases: for example, for circular, non-overlapping orbits $s_{ij\ell} = 1$ for all ℓ , and for eccentric radially non-overlapping orbits we have (Eq. B16)

$$s_{ij\ell} = \frac{\chi_{\text{out}}^\ell}{\chi_{\text{in}}^{\ell+1}} P_{\ell+1}(\chi_{\text{in}}) P_{\ell-1}(\chi_{\text{out}}) \quad \text{if } r_{a,\text{in}} < r_{p,\text{out}}, \quad (8)$$

for $\ell > 0$, where χ_i is the aspect ratio of the elliptical orbit of star i , i.e., $\chi_i = a_i/b_i = 1/\sqrt{1 - e_i^2}$, where $b_i = a_i \sqrt{1 - e_i^2}$ is the semiminor axis. The integral $s_{ij\ell}$ in Eq. (7) depends on the four parameters α_{ij} , e_{in} , e_{out} , and ℓ , and can be tabulated on a four-dimensional grid. The integral for all stellar pairs may then be obtained by interpolation on the grid³.

The sum over ℓ in Eq. (5) converges very quickly for radially non-overlapping orbits with $\alpha_{ij} \ll 1$. The convergence is slower for $\alpha_{ij} \sim 1$ or for radially overlapping orbits, but even so the terms in the sum decrease asymptotically as $\ell^{-2} \ell^{-2.5}$ except for a set of measure zero (see Appendix B5 for a thorough discussion of convergence). The first 10 even multipoles are typically sufficient for at least $\sim 1\%$ accuracy. The series converges more slowly if the periapsides or the apoapsides of the two orbits coincide and the orbits are coplanar ($\sim \ell^{-2} \ln \ell$), especially if one of the orbits is circular ($\sim \ell^{-1.5}$), or if the orbits are circular with the same radii but not coplanar ($\sim \ell^{-1.5}$). The sum diverges (terms $\sim \ell^{-1}$) only if the two orbits are circular with the same radii and coplanar ($\alpha_{ij} = 1$ and $e_i = e_j = I_{ij} = 0$).

Since the averaged surface density representing each star is stationary and axisymmetric on the orbital timescale P , and the precession timescale $t_{\text{prec}} \gg P$, the orbits conserve their Keplerian energy and their scalar angular momentum $L = \|\mathbf{L}\|$ as they interact. Thus, the semimajor axes and eccentricities are conserved during the evolution.

³ The grid must be sufficiently dense to resolve the resonance peaks shown in Figure 1 below.

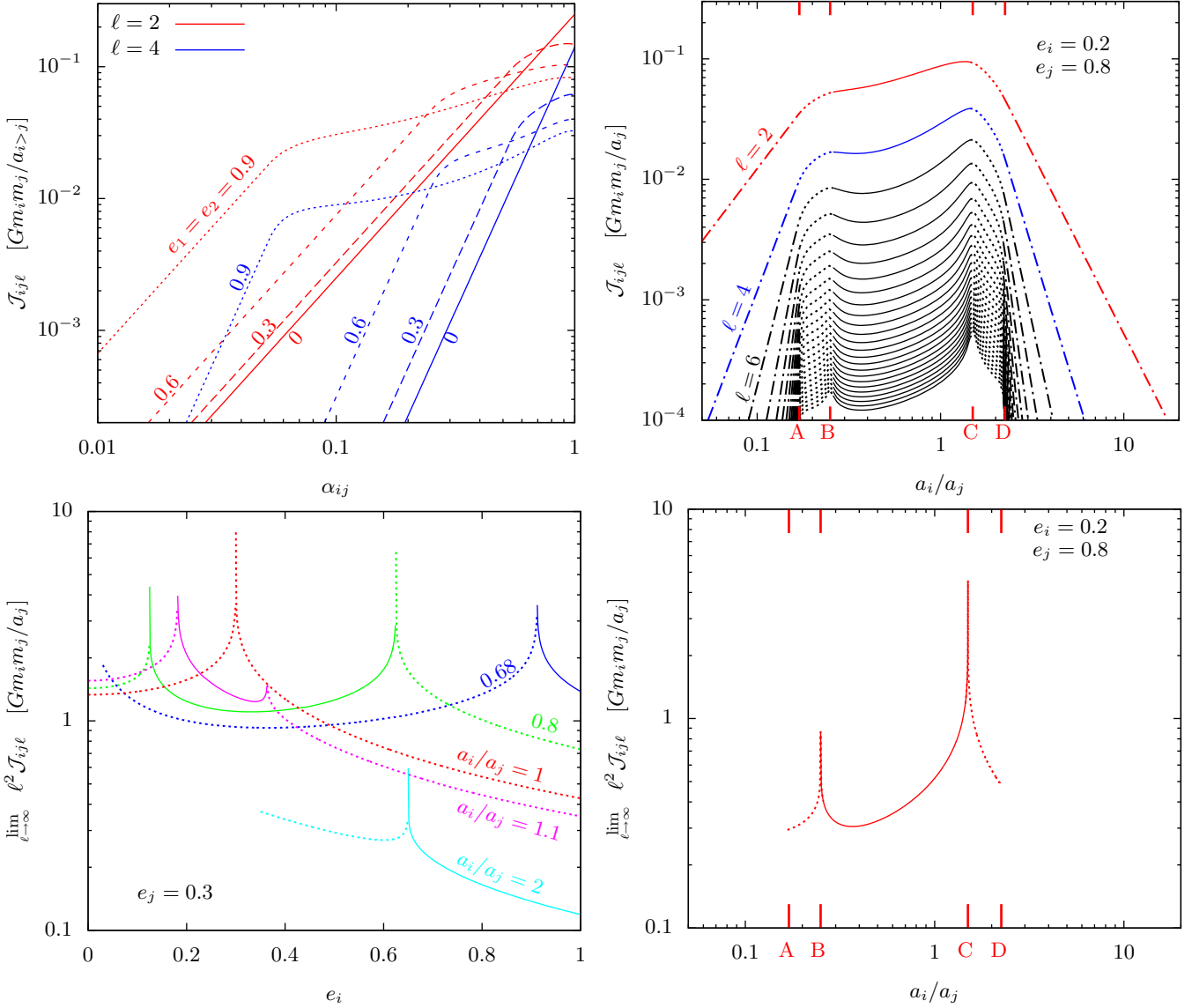


Figure 1. VRR coupling coefficients $\mathcal{J}_{ij\ell}$ (Eqs. 9 and 10). The subscripts i and j label the stars and ℓ labels the (even) multipole order. *Top left panel:* Eccentricities $e_i = e_j = 0$ (solid line), 0.3 (long-dashed), 0.6 (short-dashed), and 0.9 (dotted). The red and blue curves show $\mathcal{J}_{ij\ell}$ for the multipoles $\ell = 2$ and 4, respectively, as a function of the semimajor axis ratio $\alpha_{ij} = \min(a_i, a_j) / \max(a_i, a_j)$. Circular orbits are coupled more strongly than eccentric orbits for comparable semimajor axes ($\alpha \sim 1$), but the coupling falls off more slowly for eccentric orbits in the range $1 \geq \alpha_{ij} \geq (1 - e)/(1 + e)$ where there is radial overlap. *Top right panel:* $e_i = 0.2$ and $e_j = 0.8$. Here additional multipoles up to $\ell = 50$ are shown as a function of the semimajor axis ratio a_i/a_j . Different line styles show different radial regimes, as defined in Appendix B: non-overlapping orbits (dash-dotted), overlapping (dotted), and embedded (solid). The boundaries between these regions are marked with A, B, C, and D which satisfy $a_i/a_j = (1 \pm e_j)/(1 \pm e_i)$. *Bottom panels:* The limiting behavior of $\ell^2 \mathcal{J}_{ij\ell}$ for asymptotically large ℓ , as a function of eccentricity and semimajor axis. In the bottom left panel, $e_j = 0.3$ and $a_i/a_j = 0.68, 0.8, 1, 1.1,$ and 2 for different curves, as labeled. In the bottom right panel $e_i = 0.2$ and $e_j = 0.8$ and a_i/a_j is varied. The limit of $\ell^2 \mathcal{J}_{ij\ell}$ is zero for non-overlapping orbits, finite and non-zero for overlapping (dotted lines) or embedded orbits (solid lines), and divergent if the periapsides or the apoapsides coincide (see Appendix B5).

In summary,

$$H_{\text{RR}} = - \sum_{ij\ell} \mathcal{J}_{ij\ell} P_\ell(\hat{\mathbf{L}}_i \cdot \hat{\mathbf{L}}_j), \quad (9)$$

where the dynamical variables are the unit vectors normal to the orbits, $\hat{\mathbf{L}}_i \equiv \mathbf{L}_i/L_i$, and $\mathcal{J}_{ij\ell}$ are constant coupling coefficients

$$\mathcal{J}_{ij\ell} = \frac{Gm_i m_j}{a_{\text{out}}} P_\ell(0)^2 s_{ij\ell} \alpha_{ij}^\ell. \quad (10)$$

The top panels of Figure 1 show $\mathcal{J}_{ij\ell}$ for $\ell = 2-4$ (top left panel) and 2–50 (top right panel), for a range of semimajor axis ratios a_i/a_j and selected values of the eccentricities e_i and e_j . At all semimajor axes and eccentricities, the interaction energy is dominated by the $\ell = 2$ quadrupolar term and decreases monotonically with ℓ . The coupling declines rapidly with ℓ , as $\alpha_{ij}^\ell (1 + e_{\text{in}})^\ell / (1 - e_{\text{out}})^\ell$, for radially non-overlapping orbits, i.e., for $\alpha_{ij} < (1 - e_{\text{out}})/(1 + e_{\text{in}})$. The coupling coefficients exhibit peaks when the periapsides or

apoapses coincide, which become increasingly prominent as ℓ increases. The bottom panels show the limit of $\ell^2 \mathcal{J}_{ij\ell}$ for large ℓ , as a function of e_i and a_i/a_j , respectively. This quantity is relevant for the torque exerted between inclined orbits as we show below. The limit is zero for non-overlapping orbits, but finite positive for overlapping or embedded orbits (see Appendix B for precise definitions of these terms). Thus, a larger number of multipoles is needed to calculate accurately the torques between overlapping or embedded orbits.

2.2 Equations of motion

We have argued that only the directions of the angular momenta of the stellar orbits change due to the averaged star-star interactions, while the scalar angular momenta $L = \|\mathbf{L}\|$ are conserved. The equations of motion for the angular momenta can be derived using Poisson brackets.

We shall use Greek subscripts to denote Cartesian coordinates (x, y, z) . The Poisson brackets of the angular-momentum vectors satisfy $\{L_{i\alpha}, L_{j\beta}\} = \sum_{\gamma} \delta_{ij} \epsilon_{\alpha\beta\gamma} L_{i\gamma}$; here i and j label the stars, $\delta_{ij} = 1$ if $i = j$ and zero otherwise, and $\epsilon_{\alpha\beta\gamma}$ is the Levi-Civita or antisymmetric tensor. For any complete set of phase space variables $\{X_s\}$ and a function f of phase-space variables, we have

$$\frac{df}{dt} = \{f, H\} = \sum_s \{f, X_s\} \frac{\partial H}{\partial X_s} \quad (11)$$

where H is the Hamiltonian. Using Eqs. (9) and (10) the equations of motion become

$$\begin{aligned} \frac{dL_{i\alpha}}{dt} &= \{L_{i\alpha}, H\} = \sum_{j=1}^N \sum_{\beta=1}^3 \{L_{i\alpha}, L_{j\beta}\} \frac{\partial H}{\partial L_{j\beta}} \\ &= - \sum_{j\ell\beta\gamma} \epsilon_{\alpha\beta\gamma} \frac{L_{i\gamma} L_{j\beta}}{L_i L_j} \mathcal{J}_{ij\ell} P'_\ell(\hat{\mathbf{L}}_i \cdot \hat{\mathbf{L}}_j), \end{aligned} \quad (12)$$

where $P'_\ell(x)$ is the derivative of the Legendre polynomial⁴, and $L = \|\mathbf{L}\|$. This can be expressed more simply as

$$\begin{aligned} \dot{\mathbf{L}}_i &= \boldsymbol{\Omega}_i \times \mathbf{L}_i, \\ \boldsymbol{\Omega}_i &= - \sum_{j\ell} \frac{\mathcal{J}_{ij\ell}}{L_i L_j} P'_\ell(\hat{\mathbf{L}}_i \cdot \hat{\mathbf{L}}_j) \mathbf{L}_j. \end{aligned} \quad (13)$$

The vector $\boldsymbol{\Omega}_i$ is the angular velocity of the precession of the angular-momentum vector of a star i due to its averaged interactions with the other stars.

Using the \mathbf{L}_i as phase-space variables, the phase space has $3N$ dimensions. There are $N + 2$ conserved quantities:

$$\begin{aligned} \frac{d}{dt} E_{\text{RR}} &= - \frac{d}{dt} \sum_{ij\ell} \mathcal{J}_{ij\ell} P_\ell(\hat{\mathbf{L}}_i \cdot \hat{\mathbf{L}}_j) = 0, \\ \frac{d}{dt} \sum_i \mathbf{L}_i &= - \sum_{ij\ell} \frac{\mathcal{J}_{ij\ell}}{L_i L_j} P'_\ell(\hat{\mathbf{L}}_i \cdot \hat{\mathbf{L}}_j) \mathbf{L}_j \times \mathbf{L}_i = 0, \\ \frac{d}{dt} (\mathbf{L}_i \cdot \mathbf{L}_i) &= 0 \quad \text{for all } i \in \{1, \dots, N\}. \end{aligned} \quad (14)$$

The first is the conservation of total energy, which follows because the Hamiltonian H_{RR} (Eq. 9) is independent of time. The second is the conservation of the total angular-momentum vector, which follows from the double sum over

i and j of products of symmetric ($\mathcal{J}_{ij\ell} = \mathcal{J}_{ji\ell}$) and antisymmetric terms ($\hat{\mathbf{L}}_j \times \hat{\mathbf{L}}_i$). The third is the conservation of the scalar angular momentum of each star, $L_i = m_i \sqrt{GM_\bullet a_i (1 - e_i^2)}$, due to the orthogonality of \mathbf{L}_i and $\dot{\mathbf{L}}_i$ in Eq. (13). The first two conservation laws are valid for the original N-body system, but the third holds only after we average over the orbital period P and apsidal precession time t_{prec} .

3 NUMERICAL INTEGRATOR

3.1 Pairwise evolution

Since the Hamiltonian H_{RR} is a sum of pairwise interaction terms it is useful to first examine the evolution under a single such term and then superimpose the effects of all the pairs.

The interaction between a single pair of stars leads to uniform precession of their angular momenta around their common total angular-momentum vector. Because of this simple behavior, the equations of motion can be integrated analytically, as we now show. Eq. (13) implies that

$$\begin{aligned} \frac{d\mathbf{L}_i}{dt} &= - \sum_{\ell=2}^{\infty} \frac{\mathcal{J}_{ij\ell}}{L_i L_j} P'_\ell(\hat{\mathbf{L}}_i \cdot \hat{\mathbf{L}}_j) \mathbf{L}_j \times \mathbf{L}_i, \\ \frac{d\mathbf{L}_j}{dt} &= - \frac{d\mathbf{L}_i}{dt}. \end{aligned} \quad (15)$$

Introduce new variables $\mathbf{J}_{ij} = (\mathbf{L}_i + \mathbf{L}_j)/2$ and $\mathbf{K}_{ij} = (\mathbf{L}_i - \mathbf{L}_j)/2$. Then the equations become

$$\frac{d\mathbf{J}_{ij}}{dt} = 0 \quad \text{and} \quad \frac{d\mathbf{K}_{ij}}{dt} = \boldsymbol{\Omega}_{ij} \times \mathbf{K}_{ij}, \quad (16)$$

where

$$\boldsymbol{\Omega}_{ij} = - \sum_{\ell=2}^{\infty} \frac{2\mathcal{J}_{ij\ell}}{L_i L_j} P'_\ell \left(\frac{J_{ij}^2 - K_{ij}^2}{L_i L_j} \right) \mathbf{J}_{ij} = \text{const}. \quad (17)$$

The magnitudes of \mathbf{J}_{ij} and \mathbf{K}_{ij} are both conserved. Thus $\boldsymbol{\Omega}_{ij}$ is conserved, so \mathbf{K}_{ij} rotates uniformly with angular velocity $\boldsymbol{\Omega}_{ij}$, and we have

$$\begin{aligned} \mathbf{J}_{ij}(t) &= \mathbf{J}_{ij0} \\ \mathbf{K}_{ij}(t) &= \cos[\Omega_{ij}(t - t_0)] \mathbf{K}_{ij0} \\ &\quad + \sin[\Omega_{ij}(t - t_0)] \hat{\boldsymbol{\Omega}}_{ij} \times \mathbf{K}_{ij0} \\ &\quad + \{1 - \cos[\Omega_{ij}(t - t_0)]\} (\mathbf{K}_{ij0} \cdot \hat{\boldsymbol{\Omega}}_{ij}) \hat{\boldsymbol{\Omega}}_{ij} \end{aligned} \quad (18)$$

where $\mathbf{K}_{ij0} = \mathbf{K}_{ij}(t_0)$ and $\mathbf{J}_{ij0} = \mathbf{J}_{ij}(t_0)$ denote the initial conditions.

The angular momenta are fixed if \mathbf{L}_i and \mathbf{L}_j are parallel, antiparallel, or perpendicular. Nearly perpendicular angular momenta precess with nearly zero angular velocity, but nearly parallel angular momenta with mutual inclination $I_{ij} \ll 1$ precess with a nonzero angular speed $\Omega_{ij} \approx \sum_{\ell \text{ even}} \ell J_1(\ell I_{ij}) \mathcal{J}_{ij\ell} (\mathbf{L}_i + \mathbf{L}_j) / (I_{ij} L_i L_j)$ in a retrograde direction relative to $\mathbf{L}_i + \mathbf{L}_j$; here J_1 is a Bessel function (see Eq. B74). For overlapping or embedded orbits, $\ell^2 \mathcal{J}_{ij\ell}$ approaches a finite limit (Eq. B71) shown in Figure 1, thus the angular velocity tends asymptotically to

$$\begin{aligned} \boldsymbol{\Omega}_{ij} &\approx - \lim_{\ell \rightarrow \infty} (\ell^2 \mathcal{J}_{ij\ell}) \sum_{\ell \text{ even}} \frac{J_1(\ell I_{ij})}{\ell I_{ij}} \frac{\mathbf{L}_i + \mathbf{L}_j}{L_i L_j} \\ &\approx - \lim_{\ell \rightarrow \infty} (\ell^2 \mathcal{J}_{ij\ell}) \frac{\mathbf{L}_i + \mathbf{L}_j}{2I_{ij} L_i L_j}, \end{aligned} \quad (19)$$

⁴ Note that $P'_n(x) = n[P_{n-1}(x) - xP_n(x)]/(1 - x^2)$.

where the sum has been approximated by an integral in the last equation. Thus the precession speed $\|\dot{\mathbf{L}}_i\| = \|\boldsymbol{\Omega}_{ij} \times \mathbf{L}_i\|$ approaches a finite non-zero limit for $I_{ij} \rightarrow 0$ for overlapping or embedded orbits. The bottom panels of Figure 1 show that $\lim_{\ell \rightarrow \infty} \ell^2 \mathcal{J}_{ij\ell}$ is singular when the periapsides or apoapsides of the two orbits coincide, so the precession speed is singular in this case. Furthermore, since the torque is non-zero when either eccentricity tends to unity, $\boldsymbol{\Omega}_{ij}$ tends to infinity as $\hat{\mathbf{L}}_j I_{ij}^{-1} (1 - e_i^2)^{-1/2}$ when $e_i \rightarrow 1$; thus very eccentric orbits precess very rapidly. Similar remarks apply for nearly antiparallel angular momenta. We derive the asymptotic angular velocity for arbitrary inclinations in Appendix B6 (Eq. B83).

3.2 Symplectic integrator

A system of N stars has $\frac{1}{2}N(N-1)$ pairwise interactions. Clearly, we can integrate this system numerically by advancing the angular momentum of each pair of stars in turn using the results of the previous subsection. However, there is some advantage to deriving this result in a more systematic and general way.

The evolution is governed by the first-order differential equations (13). We may write these as

$$\dot{\mathbf{L}} = \mathfrak{G}\mathbf{L} \quad (20)$$

where $\mathbf{L} \equiv (\mathbf{L}_1, \dots, \mathbf{L}_N)$ and \mathfrak{G} is the operator defined by

$$\mathfrak{G}\mathbf{L} = (\boldsymbol{\Omega}_1 \times \mathbf{L}_1, \dots, \boldsymbol{\Omega}_N \times \mathbf{L}_N). \quad (21)$$

The operator \mathfrak{G} can be written as a sum over pairs,

$$\mathfrak{G} = \sum_{i=1}^N \sum_{j>i} \mathfrak{G}_{ij} \quad (22)$$

where \mathfrak{G}_{ij} operates only on the pair of angular momenta $\mathbf{L}_i, \mathbf{L}_j$ as described in Section 3.1. Thus the commutator $[\mathfrak{G}_{ij}, \mathfrak{G}_{mn}]$ is zero if and only if the pairs ij and mn have no member in common. Since $\boldsymbol{\Omega}_i$ depends explicitly on \mathbf{L} , \mathfrak{G}_{ij} is a nonlinear operator.

The solution to the equations of motion (20) is formally

$$\mathbf{L}(t) = \exp(\Delta t \mathfrak{G})\mathbf{L}(t_0) = \sum_{n=0}^{\infty} \frac{\Delta t^n}{n!} \mathfrak{G}^n \mathbf{L}(t_0), \quad \Delta t \equiv t - t_0. \quad (23)$$

Since \mathfrak{G} is a sum of operators \mathfrak{G}_{ij} that do not all commute, the exponential of \mathfrak{G} is not simply the product of the exponentials \mathfrak{G}_{ij} . The Zassenhaus formula shows that to second order in Δt (see Casas et al. 2012, and references therein)

$$\exp(\Delta t \mathfrak{G}) = \left(\prod_J \exp(\Delta t \mathfrak{G}_J) \right) \times \left(\prod_{J<K} \exp\left(-\frac{1}{2}\Delta t^2 [\mathfrak{G}_J, \mathfrak{G}_K]\right) \right). \quad (24)$$

Here $J, K = 1, 2, \dots, N(N-1)/2$ are indices labeling all of the particle pairs in an arbitrary order. Assuming that the first product of exponentials is evaluated in this order $[\exp(\Delta t \mathfrak{G}_1) \exp(\Delta t \mathfrak{G}_2) \dots]$, the second product can be evaluated in any order so long as $J < K$ in each commutator $[\mathfrak{G}_J, \mathfrak{G}_K]$.

In the following we keep only the first product which corresponds to a composition of the actions of independent

pairwise interactions generated by Hamiltonians $H_{\text{RR}}^{(ij)}$. The state vector of the system $\mathbf{L} = (\mathbf{L}_1, \mathbf{L}_2, \dots, \mathbf{L}_N)$ then follows as

$$\mathbf{L}(t) = \prod_{i,j}^{i>j} \mathbf{O}_{ij}(\Delta t) \mathbf{L}(t_0), \quad \text{where } \mathbf{O}_{ij}(\Delta t) = \exp(\Delta t \mathfrak{G}_{ij}). \quad (25)$$

In Section 3.1 we have derived the analytic solution to the pairwise interaction: $\mathbf{O}_{ij}(\Delta t)$ rotates \mathbf{L}_i and \mathbf{L}_j around their common total angular-momentum vector by a finite angle $\boldsymbol{\Omega}_{ij} \Delta t$, keeping all other \mathbf{L}_k fixed.

The integrator given by Eq. (25) is symplectic since each component operator $\mathbf{O}_{ij}(\Delta t)$ is the exact solution of the equations of motion for the Hamiltonian $H_{\text{RR}}^{(ij)}$. However it is only first-order accurate, i.e., the truncation error after a fixed integration time $\Delta T = n\Delta t$ varies as Δt or as n^{-1} . Errors arise due to the non-commutativity of different interaction pairs and the effects of higher order interactions in Eq. (24). Convergence may be improved either by using a higher order integrator or by choosing a particular ordering of the evaluation of the \mathbf{O}_{ij} . We discuss these and other improvements to the numerical algorithm in the following subsections.

3.3 Higher order accuracy

A simple way to improve the integrator to second-order (error of order $(\Delta t)^2$ after a fixed integration time) is to choose a time-reversible ordering of terms, e.g.,

$$\mathbf{L}(t) = \prod_{i=2}^N \prod_{j=1}^{i-1} \mathbf{O}_{ij}(\Delta t/2) \times \prod_{i=N}^2 \prod_{j=i-1}^1 \mathbf{O}_{ij}(\Delta t/2) \mathbf{L}(t_0) \quad (26)$$

Products are ordered from the initial to final values (shown on the bottom and top of the product symbols) here and below if not stated otherwise. Since each term is time-reversible, i.e., $\mathbf{O}_{ij}(\Delta t)\mathbf{O}_{ij}(-\Delta t) = \mathbf{I}$ is the identity operator for arbitrary Δt , their reversible composition is time-reversible. Hence, the truncation error after a fixed time interval must be even in the timestep Δt and so must be at least of order $(\Delta t)^2$.

Higher order algorithms can be constructed by varying Δt in successive iteration steps (Yoshida 1990; Suzuki 1990). For example, if we label the second-order operator on the right side of Eq. (26) $\mathbf{O}^{(2)}(\Delta t)$, an eighth-order integrator is

$$\mathbf{O}^{(8)}(\Delta t) = \prod_{s=0}^{14} \mathbf{O}^{(2)}(r_s \Delta t) \quad (27)$$

where (Suzuki 1994)

$$\begin{aligned} r_0 &= r_{14} = 0.74167036435061295344822780 \\ r_1 &= r_{13} = -0.4091008258000315939973001 \\ r_2 &= r_{12} = 0.19075471029623837995387626 \\ r_3 &= r_{11} = -0.57386247111608226665638773 \\ r_4 &= r_{10} = 0.29906418130365592384446354 \\ r_5 &= r_9 = 0.33462491824529818378495798 \\ r_6 &= r_8 = 0.31529309239676659663205666 \\ r_7 &= -0.79688793935291635401978884. \end{aligned} \quad (28)$$

Note that here 15 evaluations are required for each Δt , i.e. the execution time of $\mathbf{O}^{(8)}(15\Delta t)$ is equivalent to that

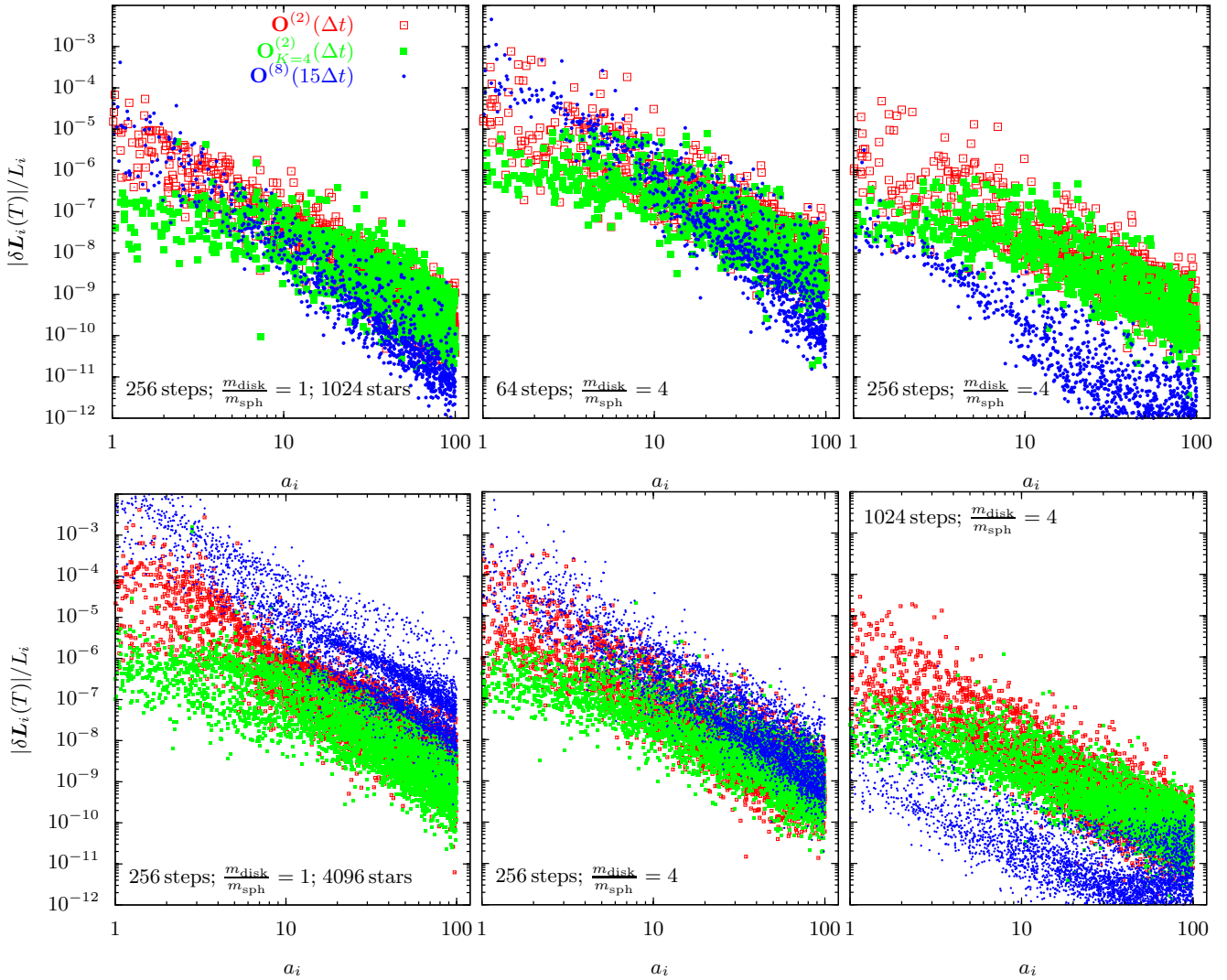


Figure 2. Angular-momentum convergence errors $\|\delta \mathbf{L}\|/L \equiv \|\mathbf{L} - \mathbf{L}^{\text{true}}\|/L$ after a fixed time T , as a function of semimajor axis a . The cluster has $N = 1024$ and 4096 stars in the top and bottom rows, respectively. The number of simulation steps varies across the panels as marked; the reference angular momentum \mathbf{L}^{true} is determined by integrating with 4096 timesteps. Three different integrators are shown: (i) the open red squares show the second-order integrator $\mathbf{O}^{(2)}(\Delta t)$ (Eq. 26); (ii) the filled green squares show the same integrator, but with the timestep for the innermost $N/4$ stars reduced by a factor of 16; (iii) the small blue circles show the eighth-order integrator $\mathbf{O}^{(8)}(15\Delta t)$ (Eq. 27; the factor 15 is chosen so that the second-order and eighth-order integrators have the same number of function evaluations per unit time). All simulations neglect multipoles beyond $\ell_{\text{max}} = 20$. The stars are initially distributed spherically and in a disk with root mean square (RMS) inclination 0.1; the two components have the same total mass in all panels. In the left panel, the sphere and disk stars have equal mass, in the middle and right panels the disk stars are 4 times as massive as the stars in the spherical component. The total simulated time interval corresponds to a VRR timescale of the inner edge of the cluster $t_{\text{vrr}} = M_{\bullet}/(m_{\text{RMS}}\sqrt{N})P_{\text{min}}$, $m_{\text{RMS}} = \langle m^2 \rangle^{1/2}$, $P_{\text{min}} = 2\pi a_{\text{min}}^{3/2}/(GM_{\bullet})^{1/2}$ (Eq. 79). For both the disk and the sphere the initial conditions are $n(a) \propto a^{-2.4}$, $a_{\text{max}}/a_{\text{min}} = 100$, $dN/de \propto e$ for $e \leq 0.9$.

of $\mathbf{O}^{(2)}(\Delta t)$ repeated 15 times. The truncation error of $\mathbf{O}^{(8)}(15\Delta t)$ is much smaller than that of $\mathbf{O}^{(2)}(\Delta t)$ for sufficiently small Δt as shown in the right panels of Figure 2.

3.4 Timestep refinement

As seen in Figure 2, the integration errors of the innermost stars in a cluster typically greatly exceed those of the outer stars. This is not surprising, since the coupling coefficients satisfy $\mathcal{J}_{ij\ell} \propto 1/a_{\text{out}}$ (Eq. 10), and from Eq. (12) the characteristic timescale for changes in the angular momentum of star i is $\Delta t_{\text{int}} \approx L_i/(a^3 n(a) \mathcal{J}_{ij\ell}) \propto a^{\gamma-1.5}$ where $n(a) \propto a^{-\gamma}$

is the number density of stars in the cluster⁵. Thus, stars at smaller semimajor axes require a smaller timestep Δt for the same integration accuracy. The errors may be efficiently reduced by implementing a block timestep procedure that preserves the symplectic and time-reversible properties

⁵ The interaction is often strongest for a stellar disk component even if it is subdominant in mass. The observed disk of young stars in the Galactic Centre has $\gamma = 2.4$ – 2.9 and the spherical component of old stars has $\gamma = 1.2$ – 1.75 (Bartko et al. 2009, 2010).

(Tuckerman et al. 1992; Saha & Tremaine 1994). We reduce the timestep to $\Delta t/k$ for a block containing the innermost N/K stars, and calculate the mutual interactions of the stars within the block k times before calculating their interactions with the rest of the stars. Thus, the integrator can be written as

$$\mathbf{O}_{\text{in,in}}(\Delta t, k) \mathbf{O}_{\text{in,out}}(\Delta t) \mathbf{O}_{\text{out,out}}(\Delta t) \quad (29)$$

where

$$\mathbf{O}_{\text{in,in}}(\Delta t, k) = \left[\prod_{\substack{j < i \leq N/K \\ i, j}} \mathbf{O}_{ij}(\Delta t/k) \right]^k, \quad (30)$$

$$\mathbf{O}_{\text{in,out}}(\Delta t) = \prod_{\substack{j \leq N/K < i \\ i, j}} \mathbf{O}_{ij}(\Delta t), \quad (31)$$

$$\mathbf{O}_{\text{out,out}}(\Delta t) = \prod_{\substack{N/K < j < i \\ i, j}} \mathbf{O}_{ij}(\Delta t). \quad (32)$$

The two-level timestep refinement procedure reduces the truncation errors of the stars in the inner block by a factor $\sim k^n$ for a method that converges as $\mathcal{O}(\Delta t^n)$. If the algorithm execution time is proportional to N^2 , the calculation of the inner block is approximately the same cost as the calculation of the rest of the system when $k = K^2$.

Figure 2 shows the effects of the two-level timestep refinement procedure for a cluster with $a_{\text{max}}/a_{\text{min}} = 100$. The red squares show the errors when a single timestep is used, and the green squares show the errors when using the two-level timestep procedure (with $K = 4$ and $k = 16$). The errors are indeed improved by close to $K^4 = 256$ at the smallest semimajor axes. The optimal value of K may be set according to the radial range of the simulated cluster and the number density exponent γ .

The errors may be further decreased using a Trotter decomposition in which the combined action of the operators e^A and e^B is represented as $e^{A/2} e^B e^{A/2}$ (Trotter 1959; Tuckerman et al. 1992). For $e^A \equiv \mathbf{O}_{\text{in,in}}(\Delta t, k)$ and $e^B \equiv \mathbf{O}_{\text{in,out}}(\Delta t) \mathbf{O}_{\text{out,out}}(\Delta t)$, Eq. (29) becomes

$$\mathbf{O}_{\text{in,in}}\left(\frac{1}{2}\Delta t, \frac{1}{2}k\right) \mathbf{O}_{\text{in,out}}(\Delta t) \mathbf{O}_{\text{out,out}}(\Delta t) \mathbf{O}_{\text{in,in}}\left(\frac{1}{2}\Delta t, \frac{1}{2}k\right). \quad (33)$$

The algorithm may be made time-reversible and hence second-order accurate as discussed in Section 3.3 by evaluating all operators in the reverse order in successive timesteps. An improved variant with even smaller errors is obtained by making each $\mathbf{O}_{\text{in,in}}\left(\frac{1}{2}\Delta t, \frac{1}{2}k\right)$ term in Eq. (33) time-reversible by choosing the reverse order of the pairwise operators \mathbf{O}_{ij} for steps $2, 4, \dots, \frac{1}{2}k$.

The operators $\mathbf{O}_{\text{in,out}} \mathbf{O}_{\text{out,out}}$ may be further Trotter decomposed or time-symmetrized but we find that this does not improve convergence significantly. The left and middle panels of Figure 4 show how the errors change for various implementations of the two-level timestep refinement.

Figure 2 shows that even after the two-level timestep refinement, the convergence errors vary systematically by three orders of magnitude over a factor 100 in semimajor axis. To obtain more uniform convergence, we may choose a larger inner block (i.e., smaller K) and implement a multi-level refinement by recursively refining the innermost block of stars. To start, set the 0th refinement level to be the whole cluster of stars $N_0 \equiv N$. Then set the stars in the n^{th} refinement level to be the innermost $N_n \equiv N_{n-1}/K_n$ stars,

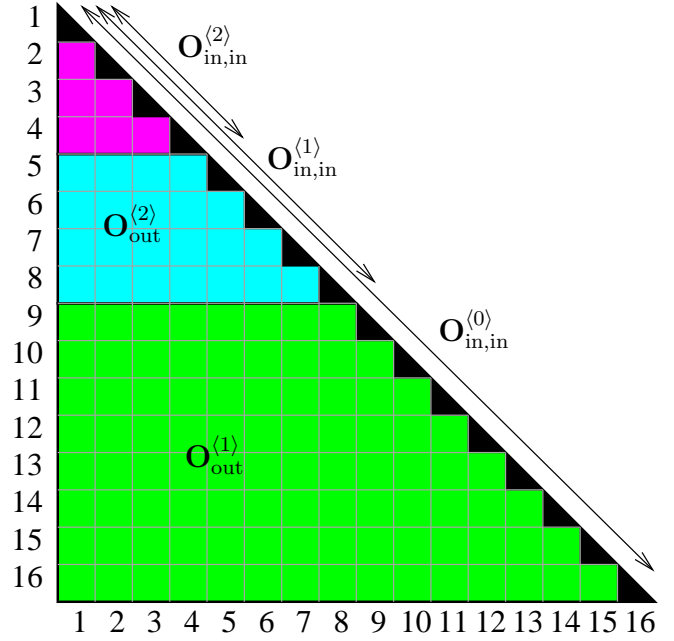


Figure 3. Timestep refinement scheme of the symplectic integrator, shown for a three-level refinement with $K_1 = K_2 = 2$ for a cluster of $N = 16$ stars. We depict the operators as elements of a lower triangular matrix as shown. The algorithm for an arbitrary number of refinement levels runs recursively as follows. In each refinement level $n < n_{\text{max}}$ a block of N_n stars is grouped in two sets based on their specific angular momentum: the $(n+1)^{\text{st}}$ “inner block” of $N_{n+1} \equiv N_n/K_{n+1}$ stars and the $(n+1)^{\text{st}}$ “outer block” of $N_n(K_{n+1}-1)/K_{n+1}$ stars. For each refinement level, the inner block is further refined and the refined operators are executed $2k_{n+1}$ times with timestep $\Delta t_{n+1} \equiv \Delta t_n/(2k_{n+1})$ each, while the interactions among the outer stars and the interactions of the inner stars with the outer stars are executed only twice with timestep $\frac{1}{2}\Delta t_n$. The algorithm starts with $\mathbf{O}_{\text{in,in}}^{(0)}$ for $N_0 = N$, which includes all stars in the inner block.

where K_n is an integer. In each refinement step, we execute the operators corresponding to interactions among these N_n stars with a reduced timestep $\Delta t_n \equiv \Delta t_{n-1}/(2k_n)$; each such operator is applied $2k_n$ times, as follows. In the n^{th} level refinement, we define the operators within the inner block recursively as

$$\begin{aligned} \mathbf{O}_{\text{in,in}}^{(n)}(\Delta t_n) &= \left[\mathbf{O}_{\text{in,in}}^{(n+1)}\left(\frac{\Delta t_n}{2k_{n+1}}\right) \right]^{\frac{1}{2}k_{n+1}} \\ &\times \mathbf{O}_{\text{out}}^{(n+1)}\left(\frac{\Delta t_n}{2}\right) \left[\mathbf{O}_{\text{in,in}}^{(n+1)}\left(\frac{\Delta t_n}{2k_{n+1}}\right) \right]^{k_{n+1}} \\ &\times \mathbf{O}_{\text{out}}^{\prime(n+1)}\left(\frac{\Delta t_n}{2}\right) \left[\mathbf{O}_{\text{in,in}}^{(n+1)}\left(\frac{\Delta t_n}{2k_{n+1}}\right) \right]^{\frac{1}{2}k_{n+1}}. \end{aligned} \quad (34)$$

where

$$\mathbf{O}_{\text{out}}^{\langle n+1 \rangle} \left(\frac{\Delta t_n}{2} \right) = \mathbf{O}_{\text{in,out}}^{\langle n+1 \rangle} \left(\frac{\Delta t_n}{2} \right) \mathbf{O}_{\text{out,out}}^{\langle n+1 \rangle} \left(\frac{\Delta t_n}{2} \right), \quad (35)$$

$$\mathbf{O}_{\text{in,out}}^{\langle n+1 \rangle} \left(\frac{\Delta t_n}{2} \right) = \prod_{\substack{j \leq N_{n+1} < i \leq N_n \\ i,j}} \mathbf{O}_{ij} \left(\frac{\Delta t_n}{2} \right), \quad (36)$$

$$\mathbf{O}_{\text{out,out}}^{\langle n+1 \rangle} \left(\frac{\Delta t_n}{2} \right) = \prod_{\substack{N_{n+1} < j < i \leq N_n \\ i,j}} \mathbf{O}_{ij} \left(\frac{\Delta t_n}{2} \right). \quad (37)$$

Here the index inside the angle brackets $\langle \cdot \rangle$ labels the refinement level, and primed operators use the reverse-order composition of the unprimed operator (as in the operators on either side of the \times in Eq. 26). The recursion ends at the final level of refinement n_{max} for which

$$\begin{aligned} \mathbf{O}_{\text{in,in}}^{\langle n_{\text{max}} \rangle} (\Delta t_{n_{\text{max}}}) &= \prod_{\substack{j < i \leq N_{n_{\text{max}}} \\ i,j}} \mathbf{O}_{ij} \left(\frac{\Delta t_{n_{\text{max}}}}{2} \right) \\ &\times \left[\prod_{\substack{j < i \leq N_{n_{\text{max}}} \\ i,j}} \mathbf{O}_{ij} \left(\frac{\Delta t_{n_{\text{max}}}}{2} \right) \right]' \end{aligned} \quad (38)$$

In practice, the simulation is advanced by Δt by running

$$\mathbf{O}_{\text{simulation}}(\Delta t) = \mathbf{O}_{\text{in,in}}^{\langle 0 \rangle}(\Delta t) \quad (39)$$

where $\mathbf{O}_{\text{in,in}}^{\langle \cdot \rangle}(\cdot)$ is defined by Eq. (34). It is instructive to verify that $\mathbf{O}_{\text{simulation}}(\Delta t)$ executes each \mathbf{O}_{ij} operator for a total interval of Δt . To see this, note that Eqs. (34)–(37) imply that $\mathbf{O}_{\text{in,in}}^{\langle 0 \rangle}(\Delta t)$ executes the interactions among the outer stars of the first refinement level ($N_1 = N/K_1 < j \leq N$) for a total time Δt , via two operations of timestep $\frac{1}{2}\Delta t$. These operators will not be executed any more during this simulation step. Furthermore $\mathbf{O}_{\text{in,in}}^{\langle 0 \rangle}(\Delta t)$ executes $\mathbf{O}_{\text{in,in}}^{\langle 1 \rangle}(\frac{1}{2}\Delta t/k_1)$ for $2k_1$ times. When doing so Eq. (34) is invoked again, each time executing the interactions among the outer stars of the second refinement level twice with timestep $\frac{1}{4}\Delta t/k_1$ each, thus in total for $4k_1$ times. Thus every outer operator of the second refinement level is run for a total time of Δt ; these operators are not executed any more during this simulation step. The recursion continues until the maximum refinement level is reached; at this stage each of the inner operators is applied twice with timestep $\frac{1}{2}\Delta t_{n_{\text{max}}}$. The maximum refinement level has $\Delta t_{n_{\text{max}}} = \Delta t / (2^{n_{\text{max}}} k_1 k_2 \dots k_{n_{\text{max}}})$. Figure 3 shows the subdivisions of the operators for a three-level refinement with $K_0 = 1$, $K_1 = 2$, and $K_2 = 2$.

Note that the reverse-order composition of operators, denoted by primes, has been invoked in Eqs. (34) and (38) to make the algorithm time-reversible. For an overview, suppressing the arguments, the refinement scheme may be summarized as

$$\begin{aligned} \mathbf{O}_{\text{in,in}}^{\langle n \rangle} &= (\mathbf{O}_{\text{in,in}}^{\langle n+1 \rangle})^{\frac{1}{2}k_{n+1}} \mathbf{O}_{\text{in,out}}^{\langle n+1 \rangle} \mathbf{O}_{\text{out,out}}^{\langle n+1 \rangle} (\mathbf{O}_{\text{in,in}}^{\langle n+1 \rangle})^{k_{n+1}} \\ &\times \mathbf{O}_{\text{out,out}}^{\langle n+1 \rangle} \mathbf{O}_{\text{in,out}}^{\langle n+1 \rangle} (\mathbf{O}_{\text{in,in}}^{\langle n+1 \rangle})^{\frac{1}{2}k_{n+1}}. \end{aligned} \quad (40)$$

With this algorithm $\mathbf{O}_{\text{in,in}}^{\langle n \rangle} = \mathbf{O}_{\text{in,in}}^{\prime \langle n \rangle}$ at all refinement levels n . Alternatively, we may time-symmetrize according to any

of the following schemes,

$$(\mathbf{O}_{\text{in,in}}^{\langle n+1 \rangle})^{k_{n+1}} \mathbf{O}_{\text{in,out}}^{\langle n+1 \rangle} \mathbf{O}_{\text{out,out}}^{\langle n+1 \rangle} \mathbf{O}_{\text{out,out}}^{\prime \langle n+1 \rangle} \mathbf{O}_{\text{in,out}}^{\prime \langle n+1 \rangle} (\mathbf{O}_{\text{in,in}}^{\langle n+1 \rangle})^{k_{n+1}}, \quad (41)$$

$$(\mathbf{O}_{\text{in,in}}^{\langle n+1 \rangle})^{k_{n+1}} \mathbf{O}_{\text{out,out}}^{\langle n+1 \rangle} \mathbf{O}_{\text{in,out}}^{\langle n+1 \rangle} \mathbf{O}_{\text{in,out}}^{\prime \langle n+1 \rangle} \mathbf{O}_{\text{out,out}}^{\prime \langle n+1 \rangle} (\mathbf{O}_{\text{in,in}}^{\langle n+1 \rangle})^{k_{n+1}}, \quad (42)$$

$$(\mathbf{O}_{\text{in,in}}^{\langle n+1 \rangle})^{k_{n+1}} \mathbf{O}_{\text{in,out}}^{\langle n+1 \rangle} \mathbf{O}_{\text{in,out}}^{\prime \langle n+1 \rangle} \mathbf{O}_{\text{out,out}}^{\langle n+1 \rangle} \mathbf{O}_{\text{out,out}}^{\prime \langle n+1 \rangle} (\mathbf{O}_{\text{in,in}}^{\langle n+1 \rangle})^{k_{n+1}}. \quad (43)$$

Figure 4 shows the convergence errors for Eqs. (40)–(43) labeled by sA, sAB, sAC, and sABC, respectively. All four methods employ a three-level timestep refinement with $K = (1, 2, 2)$. The repetition factors are $k = (1, 8, 4)$ for sA and $k = (1, 4, 4)$ for the other three methods. The execution times are comparable for each algorithm with 64 simulation steps and for the two-level timestep algorithms with 256 steps in Figure 4. The sABC method (Eq. 43) has the most homogeneous errors and smallest maximum errors. This algorithm has the most number of time-reversible factors, including the inner and outer blocks of stars and the mutual interactions between the two.

3.5 Grouping terms in blocks

The accuracy of the integrator can be significantly improved by choosing a particular order in which the interactions in Eq. (26) are calculated. One way to achieve this is by grouping the stars into blocks such that the most strongly coupled stars are mostly in the same block. Since the interactions are much weaker if the semimajor axes are widely separated, $\alpha_{ij} \ll 1$, and the precession rate is slower for less eccentric orbits, it is natural to define the blocks using criteria based on the semimajor axes or specific angular momenta $L_i/m_i \propto \sqrt{a_i(1-e_i^2)}$ of the stars. A specific assignment procedure is described in the next subsection. After defining the blocks, we evaluate the interactions block-by-block, first evaluating all the interactions within each block then the interactions between blocks,

$$\prod_{a=1}^B \prod_{b=1}^a \mathbf{O}^{a,b} \times \text{reverse order} \quad (44)$$

where $\mathbf{O}^{a,b}$ denotes the product of all pairwise interaction terms between blocks a and b , and “reverse order” denotes the time-reversed composition of operators.

3.6 Parallelization

The main bottleneck of the symplectic integrator outlined above is the steep scaling with the number of stars, at least $\mathcal{O}(N^2)$. Each timestep requires the calculation of $N(N-1)/2$ interactions. Furthermore, errors arise due to the noncommutativity of different terms which further increase with N . The steep scaling with N makes it unfeasible to simulate clusters with a realistic number of stars on a single processor. Here we show how to parallelize the algorithm to reduce the execution time.

Since the symplectic algorithm outlined above uses a composition of operators in a particular order, it is not immediately obvious whether it is possible to run the algorithm on parallel threads. Fortunately, we may realize that each

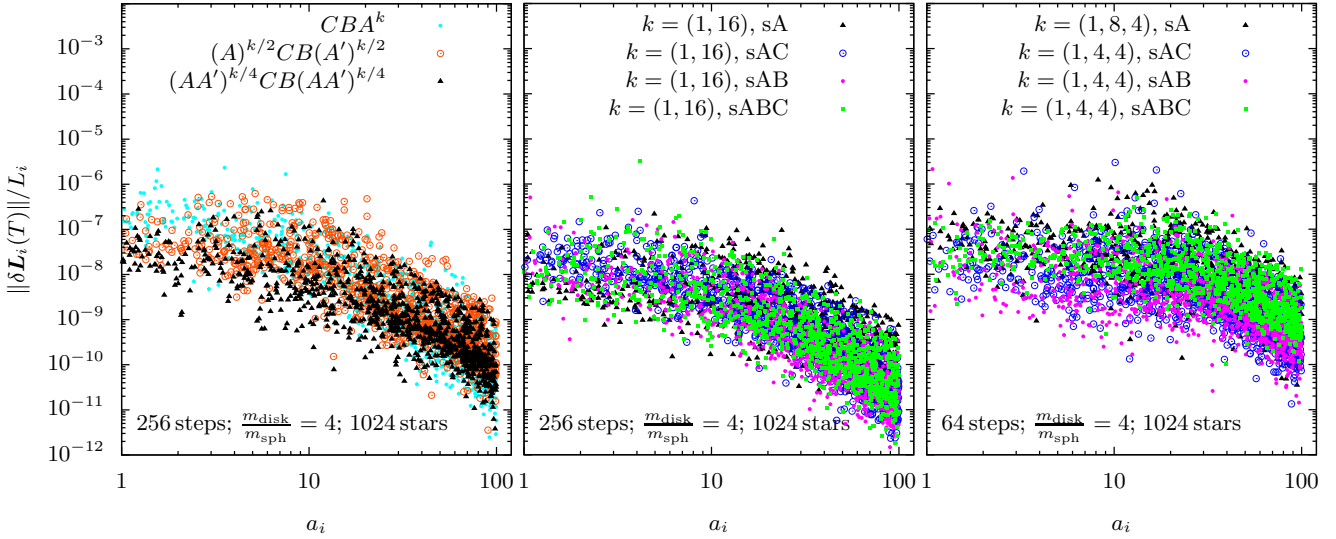


Figure 4. Angular-momentum convergence errors for simulations with different refinement methods. The left and middle panels show different algorithms with a two-level timestep refinement, the right panel shows a three-level timestep refinement. *Left panel:* The operators are labeled as follows: A represents the interactions among the members of the inner block of N/K stars (with semi-latus rectum $a_i(1 - e_i^2) \leq 8$), followed with timestep $\Delta t/k$ where $K = 4$ and $k = 16$; B is the mutual interaction between the members of the inner and outer blocks followed with timestep Δt , B is the interactions among the members of the outer block of $N - (N/K)$ stars (with $a_i(1 - e_i^2) > 8$) followed with timestep Δt . Primed operators use the reverse-order composition of the operators in the corresponding unprimed operators. The simulation parameters are the same as in the top right panel of Figure 2. The legend shows the order in which the operators are evaluated for a single simulation step from right to left. All refinement schemes employ the reverse order of operators for every second simulation step. The simplest refinement method CBA^k improves the errors by a factor ~ 40 relative to an integrator with no refinement (cf. open red squares in Figure 2). The Trotter decomposition $A^{k/2}CB(A')^{k/2}$ helps to decrease errors further by a factor ~ 4 – 5 . The inner-symmetric Trotter decomposition $(AA')^{k/4}CB(AA')^{k/4}$ method is even better, by another factor ~ 2 – 3 . *Middle panel:* Different variants of the inner-symmetric Trotter decomposition given by Eqs. (40)–(43) labeled sA, sAB, sAC, and sABC, respectively. All variants show comparable errors. *Right panel:* Three-level $K = 2$ refinement using the same algorithms and timestep as in the middle panel. The *sABC* method produces the most uniform errors, and smallest maximum errors. The two-level timestep-refined simulations execute 256 steps in $\sim 50\%$ more time than the three-level timestep-refined algorithms with 64 simulation steps.

operator \mathbf{O}_{ij} affects only \mathbf{L}_i and \mathbf{L}_j and the strict sequential ordering of \mathbf{O}_{ij} and \mathbf{O}_{kl} is not necessary if i and j are different from k and l . In particular if we split the stars into two disjoint blocks, the self-interactions of the blocks may be calculated in parallel by two threads, followed by a sequential calculation of the mutual interaction between blocks. More generally, we may split the operators into many segments of the form $\mathbf{O}_{i_1, i_2} \mathbf{O}_{i_3, i_4} \dots \mathbf{O}_{i_{N-1}, i_N}$ where (i_1, i_2, \dots, i_N) is a permutation of $(1, 2, \dots, N)$. Then all of these $N/2$ operators commute within this sequence, and can be evaluated independently on parallel threads (we show how to do this below).

With this background in mind, we construct a parallel method for $N = 2^n$ stars as shown in Figure 5. We depict the operators as elements of a lower triangular matrix, and group them into tiles of size 2^t with $t = 0, 1, \dots, n-1$ as shown for $N = 16$. We construct the tiling by recursively removing square tiles of size $2^t \times 2^t$ starting with the largest, $t = n-1$. Removing this submatrix leaves two lower triangular matrices, half the size of the original. Next we remove the $2^{t-1} \times 2^{t-1}$ square matrices from the two triangular matrices, leaving two smaller triangular matrices each. We repeat this iteration down to $t = 0$, thereby covering the matrix completely. This gives 2^{n-t-1} square tiles of size 2^t . The elements of tile $k = 0, 1, \dots, 2^{n-t-1} - 1$ of size 2^t are \mathbf{O}_{ij} where $1 \leq i - (2k+1)2^t \leq 2^t$ and $1 \leq j - (2k)2^t \leq 2^t$. All tiles of a given size represent interactions between distinct

groups of stars (i.e., the tiles of a given color in Figure 5 do not overlap horizontally or vertically). Thus, different tiles of the same size commute.

Next we discuss the commutativity of operators within a given tile. Note that the operators in any diagonal within a tile commute. This leads to a parallelization scheme based on diagonals, which is best described by an example. In the top green square in Figure 5, $(n, t, k) = (4, 2, 0)$, we may choose the following ordering

$$(\mathbf{O}_{51} \mathbf{O}_{62} \mathbf{O}_{73} \mathbf{O}_{84})(\mathbf{O}_{52} \mathbf{O}_{63} \mathbf{O}_{74} \mathbf{O}_{81}) \\ \times (\mathbf{O}_{53} \mathbf{O}_{64} \mathbf{O}_{71} \mathbf{O}_{82})(\mathbf{O}_{54} \mathbf{O}_{61} \mathbf{O}_{72} \mathbf{O}_{83}). \quad (45)$$

The terms in each parenthesis commute and can be evaluated in parallel, but synchronization is required between the parentheses. In summary, we may evaluate the action of all the \mathbf{O}_{ij} as follows

$$\prod_{i=0}^{n-1} \prod_{d=1}^{2^t} \left(\prod_{i=1}^{2^t} \prod_{k=0}^{2^{n-t-1}-1} \mathbf{O}_{(2k+1)2^t+i, (2k)2^t+[(i+d) \bmod 2^t]} \right) \quad (46)$$

where the terms in the large parentheses commute and can be run on independent threads.

More generally, instead of diagonals, we may choose any 2^t long cycle of permutations of $(1 \dots 2^t)$, labelled $Z_{(2^t)}$, to

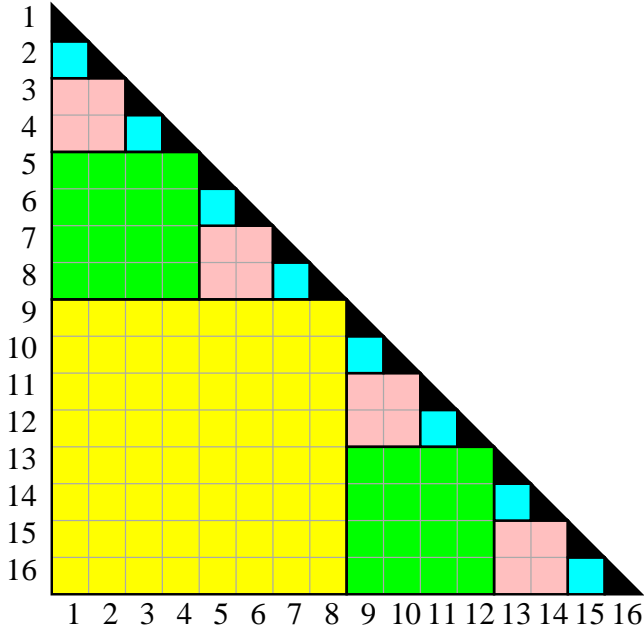


Figure 5. Parallelization scheme of the symplectic integrator. The interaction is calculated as the composition of the effects of pairwise interaction terms. We depict the interaction terms between stars i and j as elements of a lower triangular matrix and group them in tiles of size 2^t as shown. Tiles of the same size commute, and can be executed in parallel. Further, interactions within a diagonal of a given tile also commute, but different diagonals within a given tile do not, nor do different size tiles. Thus, synchronization is necessary between executing the interactions of different diagonals within a given tile and between different size tiles. For an unlimited number of processors, the algorithm execution time is $\mathcal{O}(N)$. If the number of available processors P is less than $N/2$, the parallel algorithm run-time scales as $\mathcal{O}[(N(N-1)/2P)]$ and requires exactly $2P$ synchronizations independent of N .

cover all elements of a tile

$$\prod_{t=0}^{n-1} \prod_{\sigma \in Z_{(2^t)}} \left(\prod_{i=1}^{2^t} \prod_{k=0}^{2^{n-t-1}-1} \mathbf{O}_{(2k+1)2^t+i, (2k)2^t+\sigma_i} \right). \quad (47)$$

Choosing random instead of fixed permutations for different simulation steps helps to decrease systematic errors that arise due to the noncommutativity of terms.

With at least $N/2$ processors, each parenthesis in Eqs. (46)–(47) can be evaluated in a time τ_e , where τ_e denotes the execution time corresponding to a single \mathbf{O}_{ij} operator. Different threads need to synchronize data between evaluations of non-commuting operators, and we denote the corresponding time overhead by τ_s . The execution time of one timestep of the simulation is then $\sum_{t=0}^{n-1} \sum_{d=1}^{2^t} (\tau_e + \tau_s) = (N-1)(\tau_e + \tau_s)$, so the parallelized simulation time scales as N . For a limited number of processors $P = 2^p \leq N/2$, the time for evaluating the operators in one timestep without synchronizations is $N(N-1)\tau_e/(2P)$. In this case the optimal processor allocation that provides the minimum number of synchronizations is determined as follows. First split the stellar system into $B = 2P$ blocks of stars, and calculate all of the interactions within a block on the same processor. Next, to calculate the $B(B-1)/2$ mutual interactions between blocks, we tile the blocks according to the same bi-

nary tree scheme as shown in Figure 5. The interactions of different tiles of the same size commute. Therefore we can evaluate the mutual interactions between blocks in the order given by Eqs. (46)–(47). The calculation requires synchronization after each diagonal of the tiles and after calculating the self-interactions of blocks: $2P$ synchronizations in total, independent of N . Thus, the execution time for $P < N/2$ is $N(N-1)\tau_e/(2P) + 2P\tau_s$.

The parallelization scheme outlined above applies for an arbitrary indexing of stars. In practice we may also employ all of the improvements discussed in Sections 3.3–3.4 to further speed up the calculation. The multilevel refinement outlined in Section 3.4 is commensurate with this parallelization scheme as long as the K refinement levels are powers of 2. When the timestep is decreased by a factor k , the execution time increases by the same factor for the corresponding $(N/K)^2$ operators. However, the number of synchronization steps increases significantly for each refinement level since that is independent of N .

3.7 Summary

First we summarize the algorithm for the eighth-order integrator (27), but without timestep refinement; the description for the second-order integrator is an obvious simplification of this one:

1. Calculate and store the coupling coefficients $\mathcal{J}_{ij\ell}$ for all i and j and for $\ell = 2, 4, \dots, \ell_{\max}$.
2. Order stars according to semimajor axis or specific angular momentum and divide into tiles as illustrated in Figure 5.
3. Choose a random permutation for each tile. Set the timestep to $\Delta t_s = r_s \Delta t$ for the eighth-order integrator (Eq. 27). Repeat the following for $s = 0, \dots, 14$ to advance all pairs of stars i and j by substeps Δt_s :
 - (a) Starting with the smallest tile size ($t = 0$ in Eq. 47), use parallel processors to operate on the elements of a given permutation within a tile and the different tiles of the same size [the products over k and i in Eq. (47)].
 - (b) Repeat this process for the different permutations of a given tilesize [the product over σ in Eq. (47)].
 - (c) Repeat this for the different size tiles ($t = 1, \dots, n$).
 - (d) Repeat the previous three steps in reverse order.

In the algorithm with a two-level timestep refinement and second-order integrator, iterations 3.(a)–3.(c) go as follows:

- (i) Advance the innermost N/K stars (those with the smallest indices) with a reduced timestep $\Delta t_s/k$ for a total time interval $\Delta t_s/2$, by repeating iterations 3.(a)–3.(c) $k/2$ times. In every second iteration we reverse the ordering of the operators.
- (ii) Evolve the rest of the interactions among the outer $N(K-1)/K$ stars and the mutual interactions between the inner and outer stars with a timestep $\Delta t_s/2$ and then in the reverse order for $\Delta t_s/2$.

(iii) Repeat step (i) to evolve the inner block again for a total time interval $\Delta t_s/2$.

Note that each operator is evaluated for a total Δt_s after each iteration (i)–(iii). Methods with higher order refinements decompose the inner cluster further and repeat steps (i)–(iii) for each level of refinement.

The cluster composition (in particular the mass and radius distribution of the stars) and the error tolerance determine the optimal K and repetition factors k and the most efficient order for the integrator (see Figures 2 and 4). The value of ℓ_{\max} is chosen such that $\ell_{\max} = \pi/(2I_{\min})$ where I_{\min} is the minimum inclination that must be resolved by the simulation (see Appendix B5).

4 VECTOR RESONANT RELAXATION AS A STOCHASTIC PROCESS

As an application of these results, we examine VRR of a spherical stellar cluster around a SMBH (Rauch & Tremaine 1996; Hopman & Alexander 2006; Gürkan & Hopman 2007; Eilon et al. 2009; Kocsis & Tremaine 2011; Gürkan 2011; Madigan et al. 2011; Merritt & Vasiliev 2011). As discussed in Section 1, VRR is the stochastic process arising from the torques between the annuli that represent stellar orbits that have been averaged over the orbital period and apsidal precession time. The adjective “vector” refers to the fact that such torques change the orientation of the angular-momentum vector but not the scalar angular momentum (Eq. 14).

In the standard (Chandrasekhar) model of two-body relaxation in stellar systems (e.g., Binney & Tremaine 2008), each star undergoes a random walk in Cartesian velocity space due to encounters with stars passing nearby. In the incoherent phase of VRR, each star undergoes a random walk in $\hat{\mathbf{L}}$ on the unit sphere due to torques from other stars. Two-body relaxation can be approximated as Brownian motion, that is, most of the relaxation is due to a large number of encounters of short duration. In contrast, in VRR the stochastic motion of the orbit normals cannot be divided into discrete steps occurring at a fixed and very short time interval Δt . In other words, VRR is unlike Brownian motion or diffusion in that the angular momenta move in a coherent, spatially correlated manner until their directions change substantially and they exhibit incoherent, stochastic evolution only over much longer times. For this reason, the correlation function of angular momentum vector directions *cannot* be expressed as $\|\mathbf{L}_i(t_0 + \tau) - \mathbf{L}_i(t_0)\|/\|\mathbf{L}_i(t_0)\| = (\tau/t_{\text{VRR}})^{1/2}$ in the incoherent evolutionary phase, and the definition of the vector resonant relaxation timescale t_{VRR} must be revised.

In Section 4.1, we introduce a simple stochastic model to describe incoherent VRR in a spherical stellar cluster, in which the angular momentum vector directions undergo an isotropic random walk on a spherical surface with a step size which is not infinitesimal and which is drawn from a probability distribution function (PDF). For any given PDF, we show that the stochastic evolution may be solved analytically and that the multipole moments of the correlation function with $\ell > 0$ decay exponentially (Eq. 53). We use this property to define the VRR timescale (Eq. 77) and construct moments of the stellar distribution (Eq. 65) that evolve linearly in time (Eq. 70). In Section 4.2, we analyse

the results of our numerical simulations in this framework, and in Section 4.3, we compare results in the literature for the coherent evolutionary phase of VRR with those in this study.

4.1 Random walk on the sphere – general theory

In general, a random walk on a sphere can be described as follows (Roberts & Ursell 1960; see also Debye 1929; Coffey & Kalmykov 2012). Suppose that the probability distribution for the initial position of a point \mathbf{r}_0 on the spherical surface of unit radius, S_2 , is $\rho_0(\mathbf{r})$. At step n , \mathbf{r} moves an angle $\alpha_n = \cos^{-1} \mu_n$ on the sphere in a random direction with probability $p(\mu_n)d\mu_n$. Therefore, the probability density after the n^{th} step is set by the probability density of the preceding step as⁶

$$\rho_n(\mathbf{r}) = \frac{1}{2\pi} \int_{S_2} d\mathbf{r}' \delta(\mathbf{r} \cdot \mathbf{r}' - \mu_n) \rho_{n-1}(\mathbf{r}'). \quad (48)$$

This equation is linear in ρ and can be solved using the eigenbasis of the corresponding linear operator. In Appendix C, we show that the eigenfunctions are the spherical harmonics⁷ $Y_{\ell m}(\mathbf{r})$ with eigenvalues $P_\ell(\mu_n)$. Expanding the initial distribution in this basis as

$$\rho_0(\mathbf{r}) = \sum_{\ell, m} a_{\ell m, 0} Y_{\ell m}(\mathbf{r}), \quad (49)$$

the distribution after a single step is

$$\rho_1(\mathbf{r}) = \sum_{\ell, m} P_\ell(\mu_1) a_{\ell m, 0} Y_{\ell m}(\mathbf{r}), \quad (50)$$

and after the n^{th} step it is

$$\rho_n(\mathbf{r}) = \sum_{\ell, m} a_{\ell m, n} Y_{\ell m}(\mathbf{r}) \quad (51)$$

where

$$a_{\ell m, n} = \prod_{k=1}^n P_\ell(\mu_k) a_{\ell m, 0}. \quad (52)$$

The expectation value of the (ℓ, m) spherical multipole moment in the n^{th} step is

$$\langle a_{\ell m, n} \rangle = \langle P_\ell(\mu) \rangle^n a_{\ell m, 0} \quad (53)$$

where $\langle F(\mu_k) \rangle = \int_{-1}^1 F(\mu_k) p(\mu_k) d\mu_k$ for any function $F(\mu_k)$. The RMS fluctuations around the mean are given by

$$\sigma^2 \equiv \langle a_{\ell m, n}^2 \rangle - \langle a_{\ell m, n} \rangle^2 = \left\{ \langle [P_\ell(\mu)]^2 \rangle^n - \langle P_\ell(\mu) \rangle^{2n} \right\} a_{\ell m, 0}^2 \quad (54)$$

and the cross-correlation of $a_{\ell m, n}$ and $a_{\ell' m', n}$

$$C_{\ell' m'}^{\ell m} \equiv \langle a_{\ell m, n} a_{\ell' m', n} \rangle - \langle a_{\ell m, n} \rangle \langle a_{\ell' m', n} \rangle \quad (55)$$

$$= \left\{ \langle P_\ell(\mu) P_{\ell'}(\mu) \rangle^n - \langle P_\ell(\mu) \rangle^n \langle P_{\ell'}(\mu) \rangle^n \right\} a_{\ell m, 0} a_{\ell' m', 0}. \quad (56)$$

⁶ We define the distribution function of \mathbf{r} as a random field $\rho_n(\mathbf{r}) \equiv \rho_n[\mathbf{r}; \rho_{n-1}(\mathbf{r}'), \mathbf{r}' \in S_2, \mu_n] \equiv \rho_n[\mathbf{r}; \rho_0(\mathbf{r}'), \mathbf{r}' \in S_2, \mu_1, \dots, \mu_n]$ using Eq. (48). Here the μ_i are independent random variables for all i and $\rho_0(\mathbf{r}')$ is a given initial distribution for $\mathbf{r}' \in S_2$.

⁷ See definition in Eq. (B1).

Since $|\langle P_\ell(\mu) \rangle| \leq 1$ for $\ell > 0$, each multipole moment with $\ell > 0$ decays exponentially in the number of steps as $|a_{\ell m, n}|/|a_{\ell m, 0}| = \exp[n \ln |\langle P_\ell(\mu) \rangle|]$; the system ‘‘isotropizes’’ with a decay time of $-\Delta t / \ln |\langle P_\ell(\mu) \rangle|$ where Δt is the timestep.

Since $x \equiv |a_{\ell m, n}/a_{\ell m, 0}|$ is an n -element product of independent and identically distributed positive random variables for any ℓ and m , the distribution of $\ln x$ for $n \gg 1$ follows from the central limit theorem, and we find that the probability density function of x is approximately

$$\varphi(x) \approx \frac{1}{\sqrt{2\pi n x \sigma_0}} \exp\left[-\frac{(\ln x - n\nu)^2}{2n\sigma_0^2}\right] \quad (57)$$

where

$$\nu \equiv \langle \ln |P_\ell(\mu)| \rangle, \quad \sigma_0^2 \equiv \langle [\ln |P_\ell(\mu)|]^2 \rangle - \langle \ln |P_\ell(\mu)| \rangle^2. \quad (58)$$

Note that the mean and RMS of $a_{\ell m, n}$ are given generally by Eqs. (53)–(54), while Eqs. (57)–(58) are approximate statements valid only when $n \gg 1$.

The Green’s function corresponding to an initial density ρ_0 that is concentrated at the $\theta = 0$ pole corresponds to $a_{\ell m, 0} = \sqrt{(2\ell + 1)/(4\pi)}\delta_{m, 0}$. Thus the probability distribution function for the angle θ between the initial and final position after n steps is given by

$$p_n(\theta) = 2\pi\rho_n(\mathbf{r}) \sin\theta = \sum_{\ell=0}^{\infty} \frac{2\ell+1}{2} \prod_{k=1}^n P_\ell(\mu_k) P_\ell(\cos\theta) \sin\theta, \quad (59)$$

which implies that⁸

$$\overline{P_\ell(\cos\theta)} \equiv \int_0^\pi P_\ell(\cos\theta) p_n(\theta) d\theta = \prod_{k=1}^n P_\ell(\mu_k) \quad (60)$$

where overbar denotes the average over $p_n(\theta)$. Thus after averaging over all μ_k and $p_n(\theta)$ we get

$$\overline{\langle P_\ell(\cos\theta) \rangle} = \langle P_\ell(\mu) \rangle^n. \quad (61)$$

In a planar random walk with step α , the RMS distance traveled after n steps is $\sqrt{n}\alpha$. This formula does not apply to the random walk on a sphere unless $\sqrt{n}\alpha \ll 1$, since the geometry is not planar (for example, the maximum angular distance between any two points on a sphere is π). To generalize some of the concepts of planar random walks to the sphere, we first consider the limiting case of Brownian motion, in which the angular step $\alpha = \cos^{-1}\mu$ and the timestep Δt both approach zero with $\alpha^2 \sim \Delta t$. In this limit $P_\ell(\mu) \approx \exp[-\frac{1}{4}\ell(\ell+1)\alpha^2]$, and so Eqs. (51)–(52) become⁹

$$\rho_n(\mathbf{r}) = \sum_{\ell, m} a_{\ell m, 0} Y_{\ell m}(\mathbf{r}) e^{-\frac{1}{4}\ell(\ell+1)v_n} \quad (63)$$

where $v_n = \sum_{k=1}^n \alpha_k^2$, so that $\langle v_n \rangle = n\langle \alpha^2 \rangle = \langle \alpha^2 \rangle t / \Delta t$ is

⁸ This quantity is related to the autocorrelation function of the spherical multipole moments since $\overline{P_\ell(\cos\theta)} = 4\pi(2\ell+1)^{-1} \sum_{m=-\ell}^{\ell} a_{\ell m, n} a_{\ell m, 0}^*$.

⁹ Brownian motion on the sphere also satisfies the diffusion equation (Debye 1929)

$$\frac{d\rho}{dt} = \frac{1}{4} \nabla \cdot \frac{\langle \alpha^2 \rangle}{\Delta t} \nabla \rho. \quad (62)$$

where ∇ is the gradient operator on the unit sphere.

the variance of the corresponding planar Brownian motion. The analog of Eq. (60) is

$$\overline{P_\ell(\cos\theta)} = e^{-\frac{1}{4}\ell(\ell+1)v_n}. \quad (64)$$

Motivated by the results above, we define the quantity

$$V_\ell(t) \equiv -\frac{4}{\ell(\ell+1)} \ln \left| \frac{1}{N'} \sum_{i=1}^{N'} \frac{1}{T} \int_0^T dt_0 P_\ell[\cos\alpha_i(t, t_0)] \right| \quad (65)$$

which we call the angular variance; here $\alpha_i(t, t_0)$ is the angular distance traversed by the orbit normal $\hat{\mathbf{L}}_i$ between time t_0 and time $t_0 + t$, i.e.,

$$\cos\alpha_i(t, t_0) \equiv \hat{\mathbf{L}}_i(t + t_0) \cdot \hat{\mathbf{L}}_i(t_0). \quad (66)$$

In Eq. (65), we have averaged $P_\ell(\cos\alpha_i)$ over both the cluster index and the reference time to reduce statistical noise. The ensemble average is either over the full population ($N' = N$) or over a subset of the stars ($N' < N$, e.g., over stars within a restricted range of mass, eccentricity, and semimajor axis). For Brownian motion $V_\ell(t_n)$ is an estimator of the variance v_n for all ℓ so long as $v_n \ll 1$, and for a general random walk it estimates $-4\ell^{-1}(\ell+1)^{-1}n \ln |\langle P_\ell(\mu) \rangle|$. In either case $V_\ell(t)$ grows linearly with time over timescales long compared to the timestep Δt until the ℓ^{th} multipole becomes completely mixed. Complete mixing occurs when the level of anisotropy becomes less than the stochastic variations which arise due to the finite number of stars. Thus for a single component cluster, complete mixing occurs when $V_\ell \approx V_{\ell, \text{sat}}$ with $\ell \geq 1$ and

$$\begin{aligned} \exp\left[-\frac{1}{4}\ell(\ell+1)V_{\ell, \text{sat}}\right] &\equiv \frac{1}{\sqrt{N}} \langle [P_\ell(\cos\alpha)]^2 \rangle^{1/2} \\ &= \frac{1}{\sqrt{N(2\ell+1)}}; \end{aligned} \quad (67)$$

in the last line we assumed that α is drawn from an isotropic distribution. Solving for $V_{\ell, \text{sat}}$ gives

$$V_{\ell, \text{sat}} = \frac{2 \ln [(2\ell+1)N]}{\ell(\ell+1)}. \quad (68)$$

In summary, for Brownian motion, the angular variance is expected to follow

$$V_\ell(t) = \begin{cases} \frac{t}{\Delta t} \langle \alpha^2 \rangle & \text{if } \langle \alpha^2 \rangle^{1/2} \ll 1 \text{ and } V_\ell < V_{\ell, \text{sat}}, \\ \text{stochastic variations around } V_{\ell, \text{sat}} & \text{otherwise,} \end{cases} \quad (69)$$

and for a general random walk

$$V_\ell(t) = \begin{cases} -\frac{4}{\ell(\ell+1)} \frac{t}{\Delta t} \ln |\langle P_\ell(\mu) \rangle| & \text{if } V_\ell < V_{\ell, \text{sat}}, \\ \text{stochastic variations around } V_{\ell, \text{sat}} & \text{otherwise.} \end{cases} \quad (70)$$

Complete mixing occurs when all multipole moments are completely mixed. We find below that in general the dipole moment is the slowest to mix, so complete mixing occurs after approximately $n_{\text{sat}} = -\ln 3N / (2 \ln |\langle \mu \rangle|)$ timesteps. For small angular steps $n_{\text{sat}} = \ln 3N / \langle \alpha^2 \rangle$.

4.2 Application to resonant relaxation

We now apply these results to VRR. In the incoherent phase of VRR, each star undergoes a random walk in $\mathbf{r} \equiv \hat{\mathbf{L}}$ on the unit sphere due to torques from other stars.

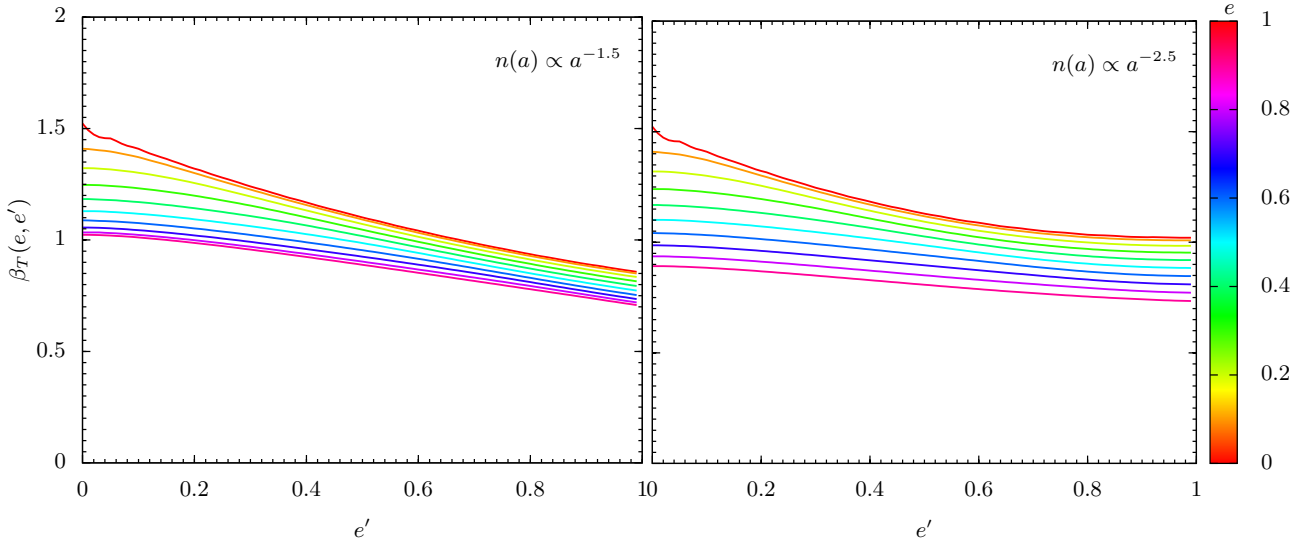


Figure 6. The dimensionless coherent torque parameter β_T (Eqs. 74 and D5) for a star with eccentricity e , orbiting in a spherical population of stars with a fixed eccentricity e' and a distribution of semimajor axes $n(a) \propto a^{-1.5}$ (left panel) and $\propto a^{-2.5}$ (right panel). The colored curves have $e = 0, 0.1, \dots, 0.9$ from top to bottom, and e' is varied on the horizontal axis.

We introduce a decoherence time t_ϕ : over time intervals much less than the decoherence time the stochastic torque on a star is temporally correlated¹⁰ (“coherent evolution”), while the torques at times separated by much more than the decoherence time are temporally uncorrelated (“incoherent evolution”). Of course, the decoherence time will depend on the eccentricity and semimajor axis of the star and the properties of the stellar cluster of which it is a member. We first determine the RMS torque that characterizes the coherent evolutionary phase, then we use the stochastic model of the previous section to characterize the incoherent evolution. We analyse our numerical simulations in this framework and determine how the model parameters depend on the physical parameters of the stellar orbits in the two regimes.

A second parameter that characterizes the evolution of a star i during VRR is related to the RMS torque that it experiences. For a cluster composed of stars of similar semimajor axes a , and a distribution of eccentricities and masses,

$$\begin{aligned} T_{\text{RMS},i} &= \langle \mathbf{T}_i^2 \rangle^{1/2} \simeq \frac{\beta_T}{2\pi} \frac{G\sqrt{N}m_{\text{RMS}}m_i}{a} \\ &= \beta_T \frac{\sqrt{N}m_{\text{RMS}}}{M_\bullet} \frac{m_i\sqrt{GM_\bullet a}}{P}, \end{aligned} \quad (71)$$

where $P = 2\pi(a^3/GM_\bullet)^{1/2}$ is the orbital period, $m_{\text{RMS}} = (N^{-1}\sum_i m_i^2)^{1/2}$, β_T is a dimensionless constant of order unity, and averaging is over the distribution of the other stars in a spherical cluster, $\hat{\mathbf{L}}_{j \neq i}$. Similarly, the RMS rate of change of the orbit normal for star i is

$$\Omega_{\text{RMS},i} = \left\langle \left(\frac{d\hat{\mathbf{L}}_i}{dt} \right)^2 \right\rangle^{1/2} = \left\langle \frac{\mathbf{T}_i^2}{L_i^2} \right\rangle^{1/2} \simeq \beta_\Omega \frac{\sqrt{N}m_{\text{RMS}}}{M_\bullet P}. \quad (72)$$

¹⁰ In practice we identify the decoherence time with the time over which the torque is approximately constant.

Using the notation of Eqs. (9) and (13),

$$\begin{aligned} \beta_T &= \frac{2\pi a}{Gm_i m_{\text{RMS}}} \left[\frac{1}{N} \sum_{j,k=1}^N \sum_{\ell,n} \mathcal{J}_{ij\ell} \mathcal{J}_{ikn} P'_\ell(\cos I_{ij}) \right. \\ &\quad \left. \times P'_n(\cos I_{ik}) (\cos I_{jk} - \cos I_{ij} \cos I_{ik}) \right]^{1/2}, \end{aligned} \quad (73)$$

and $\beta_\Omega = \beta_T(1 - e_i^2)^{-1/2}$. We simplify this expression in Appendix D. We find that the series in ℓ converges very quickly, and so the coherent torques in a spherical cluster are predominantly quadrupolar. The torque is a Gaussian random variable with zero mean and dispersion set by β_T .

More generally, if there is a range of semimajor axes with $dN = 4\pi a^2 n(a) da$ stars in the semimajor axis interval $a \rightarrow a + da$, we can replace N by $dN/d \ln a = 4\pi a^3 n(a)$ in all these equations where $a \equiv a_i$. For example, Eqs. (71) and (72) become

$$\begin{aligned} T_{\text{RMS},i} &\simeq \beta_T \frac{\sqrt{dN/d \ln a} m_{\text{RMS}}}{M_\bullet} \frac{m_i \sqrt{GM_\bullet a}}{P}, \\ \Omega_{\text{RMS},i} &\simeq \beta_\Omega \frac{\sqrt{dN/d \ln a} m_{\text{RMS}}}{M_\bullet P}. \end{aligned} \quad (74)$$

In Appendix D, we show that with this definition β_T is independent of a if the distribution of a is a power law, and independent of the distribution of stellar masses. We evaluate the average in Eq. (73) as integrals over orientation, eccentricity, and semimajor axis (Eq. D5) for $n(a) \propto a^{-1.5}$ and $\propto a^{-2.5}$. Figure 6 shows β_T for an orbit with eccentricity e , assuming that all stars in the cluster have a fixed eccentricity e' . The Figure shows that $0.7 \lesssim \beta_T \lesssim 1.5$ and that β_T is a decreasing function of both e and e' . Thus we may generally conclude that β_T must be a decreasing function of e for an arbitrary eccentricity distribution, with values in the same range 0.7–1.5. In particular Figure 7 shows β_T and β_Ω for a star cluster with a thermal eccentricity distribution $dN = 2e de$ and number density proportional to $a^{-\gamma}$ where

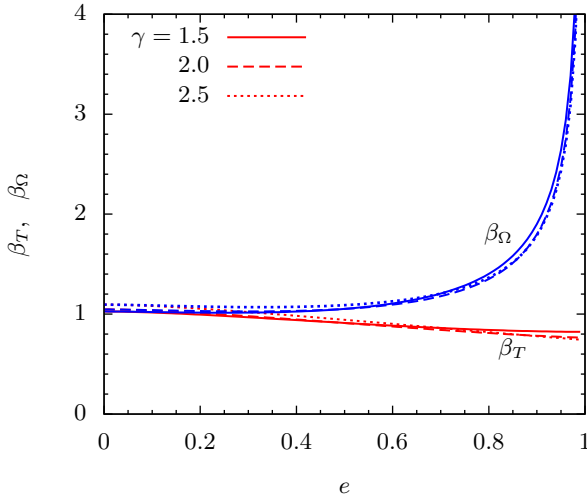


Figure 7. The dimensionless parameters β_T and β_Ω (Eq. 74) describing the RMS coherent torque and precession rate for a star with eccentricity e due to a spherical population of stars with a thermal distribution of eccentricity $dN = 2ede$ and a distribution of semimajor axes $n(a) \propto a^{-\gamma}$, where $1.5 \leq \gamma \leq 2.5$ as labeled. The evaluation is done using Eq. (D5).

$1.5 < \gamma < 2.5$. Simple fitting formulae are¹¹

$$\beta_T(e) \simeq 1.05 - 0.3e, \quad \beta_\Omega(e) \simeq \frac{1.05 - 0.3e}{(1 - e^2)^{1/2}}. \quad (75)$$

Thus we find that the angular-momentum re-orientation timescale is approximately independent of the semimajor axis distribution (i.e., the exponent γ), and is also independent of the eccentricity for $0 \leq e \leq 0.75$, to within 20% accuracy. The angular momenta of highly eccentric stars are re-oriented much more rapidly. RMS-averaging over both e and e' for a thermal distribution yields $\langle \beta_T^2 \rangle^{1/2} = 0.85$.¹²

Pursuing the analogy to the random walk on the sphere, the decoherence time t_ϕ takes the place of the timestep and $\Omega_{\text{RMS}} t_\phi$, which we call the angular coherence length, takes the place of the RMS angular displacement per timestep $\langle \alpha^2 \rangle$. On timescales short compared to the decoherence time, the orbit normals move in the mean field of the cluster at a rate $d\hat{\mathbf{L}}/dt$ which is approximately constant¹³, and the angular variance is

$$V_\ell(t) = -\frac{4}{\ell(\ell+1)} \ln \left| \left\langle P_\ell[\hat{\mathbf{L}}_i(t+t_0) \cdot \hat{\mathbf{L}}_i(t_0)] \right\rangle \right|, \quad t \lesssim t_{\phi,\ell} \\ = \Omega_{\text{RMS}}^2 t^2, \quad (76)$$

where the quadratic approximation in the second line holds so long as the angular displacement is small ($V_\ell(t) \ll 1$). On timescales long compared to the decoherence time, the

¹¹ This result disagrees with the eccentricity dependence reported by Gürkan & Hopman (2007), for reasons given in Section 4.3 below.

¹² The RMS average of β_Ω over both e and e' in a thermal eccentricity distribution is logarithmically divergent, $\langle \beta_\Omega^2 \rangle^{1/2} \propto \ln(1 - e_{\text{max}})$ for $e_{\text{max}} \rightarrow 1$.

¹³ As long as the mean-field potential is constant in time, $\hat{\mathbf{L}}$ moves with angular velocity $\partial H_{\text{RR}}/\partial \mathbf{L}$ along a closed path on the unit sphere that is a contour of constant H_{RR} , see Eq. (13).

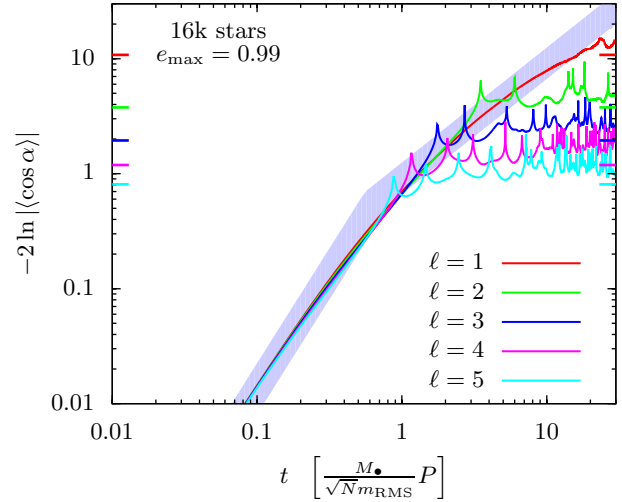


Figure 8. The evolution of the angular variance $V_\ell = -4\ell^{-1}(\ell+1)^{-1} \ln \left| (NT)^{-1} \int_0^T dt_0 \sum_{i=1}^N P_\ell[\cos \alpha_i(t, t_0)] \right|$ in a simulation with 16,384 stars. Here $\alpha_i(t, t_0)$ is the angular distance between the angular-momentum vector of star i at time t_0 and time $t+t_0$. The stars are initially spherically distributed with nearly the same semimajor axis and a uniform distribution in the square of the eccentricity for $e \lesssim 0.99$ (i.e., uniform distribution on the energy surface in phase space). The angular variance is expected to grow quadratically at early times (coherent torques) and linearly at later times (random walk on a sphere) until the mode is fully mixed, as marked by short coloured lines on the vertical axis (Eq. 68). The shaded region shows $\min[(\beta_\Omega t_{\text{VRR}}/t_{\text{VRR}})^2, t/t_{\text{VRR}}]$ for reference where $t_{\text{VRR}} = f_{\text{VRR}} [M_\bullet / (\sqrt{N} m_{\text{RMS}})] P$, $0.9 \leq \beta_\Omega \leq 1.5$, and $0.8 \leq f_{\text{VRR}} \leq 1.5$.

orbital vectors execute a random walk, where

$$V_\ell(t) = \frac{t}{t_{\text{VRR},\ell}}, \quad t \gtrsim t_{\phi,\ell}, \quad (77)$$

which defines the VRR time for the ℓ^{th} harmonic $t_{\text{VRR},\ell}$. We identify the decoherence time with the transition from quadratic to linear growth of $V_\ell(t)$, that is,

$$t_{\phi,\ell} = \frac{1}{\Omega_{\text{RMS}}^2 t_{\text{VRR},\ell}}. \quad (78)$$

For a single-component spherical cluster of stars, the torques are comparable for different stars and constant for a characteristic time $\sim \Omega_{\text{RMS}}^{-1}$, and therefore one might expect $t_\phi \sim \Omega_{\text{RMS}}^{-1}$, so the angular coherence length is $\Omega_{\text{RMS}} t_\phi \sim 1$. In this case the formulae above yield $t_{\text{VRR}} \sim \Omega_{\text{RMS}}^{-1}$ so we write

$$t_{\text{VRR}} = f_{\text{VRR}} \frac{M_\bullet}{\sqrt{N} m_{\text{RMS}}} P, \quad (79)$$

where f_{VRR} is a dimensionless constant of order unity. With these definitions the decoherence time is¹⁴

$$t_\phi = \frac{1}{f_{\text{VRR}} \beta_\Omega^2} \frac{M_\bullet}{\sqrt{N} m_{\text{RMS}}} P. \quad (80)$$

For a range of semimajor axes, the relaxation time

¹⁴ Using the notation of Eilon et al. (2009), the decoherence time is parameterized by the dimensionless constant A_ϕ as $t_\phi = A_\phi [M_\bullet / (\sqrt{N} m_{\text{RMS}})] P$.

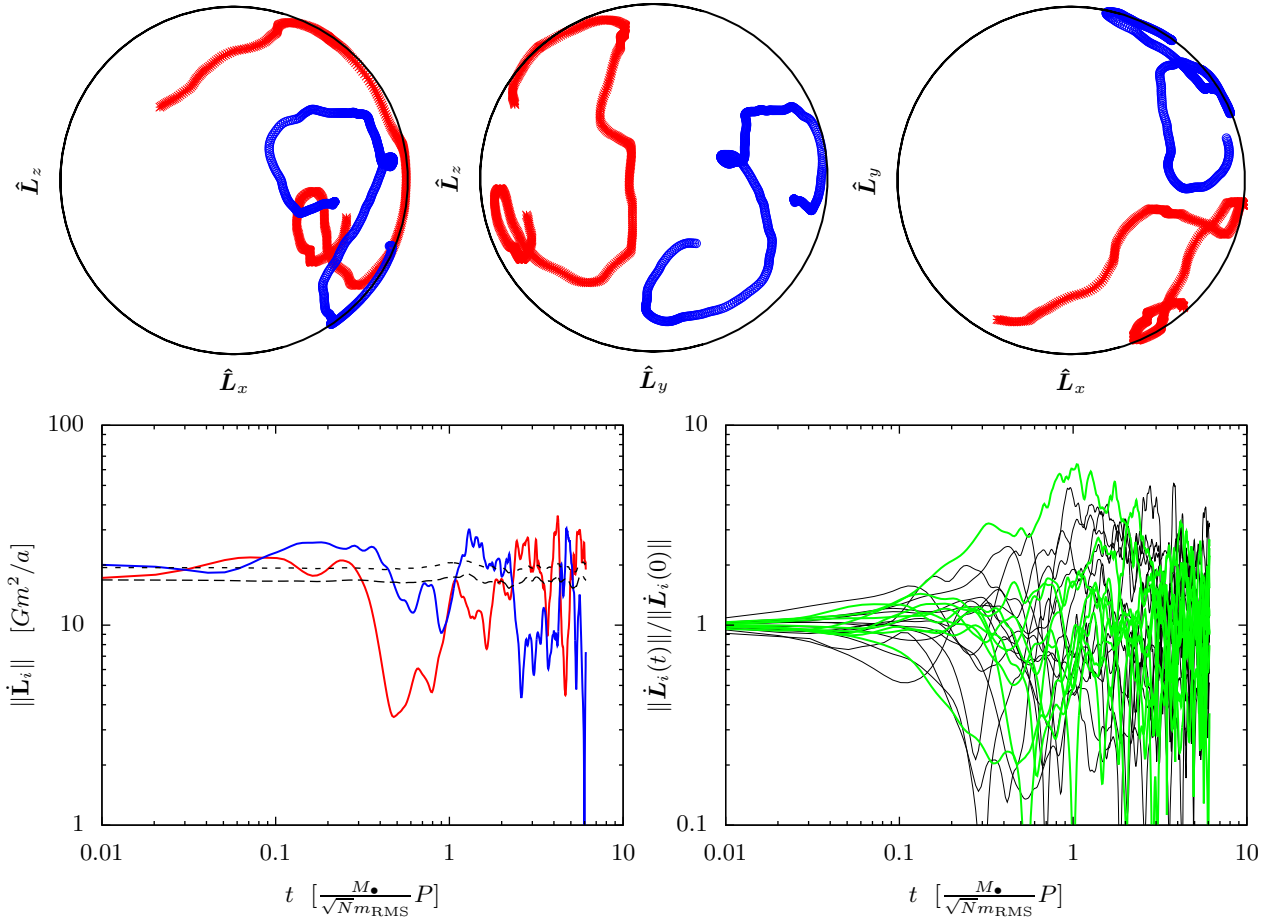


Figure 9. *Top panels:* The evolution of the normalized angular-momentum vectors for two representative stars from a simulation similar to Figure 8. The three panels show orthogonal projections on the x - z , y - z , and x - y planes. The two stars were randomly selected from a subset of stars with roughly the mean eccentricity of the cluster $\langle e \rangle = 0.58$. The motion is shown for a time interval $t = 7 \Omega_{\text{RMS}}^{-1}$. *Bottom panels:* The evolution of the torque as a function of time. The bottom left panel shows the two stars for which the trajectories are shown in the top panels. The long-dashed and short-dashed lines show the mean of $\|\mathbf{T}_i\|$ and $T_{\text{RMS},i}$ of the cluster, respectively. In the bottom right panel, the solid green and black curves in the right panel show stars with nearly the mean eccentricity, and stars from the whole eccentricity range. The decoherence time is approximately independent of eccentricity.

Eq. (79) becomes

$$t_{\text{VRR}}(a) = f_{\text{VRR}} \frac{M_\bullet}{\sqrt{4\pi a^3 n(a) m_{\text{RMS}}}} P(a). \quad (81)$$

We measure the dimensionless parameters β_Ω and f_{VRR} using numerical simulations, from the behavior of $V_\ell(t)$ at small and large times.

Figure 8 shows $V_\ell(t)$ measured in a simulation of a spherical cluster with 16,384 stars with nearly the same semimajor axes and masses. The figure shows that indeed all V_ℓ grow quadratically at first (coherent torques) and then linearly (random walk), until eventually they saturate and thereafter execute random variations. The dipole ($\ell = 1$) mixes most slowly, higher harmonics mix sooner. The curves with different ℓ approximately overlap before they saturate; this behavior is in agreement with Eq. (69) for Brownian motion even though the angular coherence length is of order unity so the Brownian approximation is questionable. The shaded region shows the model described by Eqs. (76)–(79) with $0.9 \leq \beta_\Omega \leq 1.5$ and $0.8 \leq f_{\text{VRR}} \leq 1.5$, the best-fit dimensionless torque and VRR factors are $\beta_\Omega \approx 1.2$ and $f_{\text{VRR}} \approx 1.2$. The linear evolution corresponding to a random

walk starts where $V_\ell(t_\phi) = \beta_\Omega^{-2} f_{\text{VRR}}^{-2} \approx 0.5$ for $1 \leq \ell \leq 5$. The angular coherence length is $\langle \alpha^2 \rangle^{1/2} = \Omega_{\text{RMS}} t_\phi \approx \beta_\Omega^{-1} f_{\text{VRR}}^{-1} \approx 0.7 \approx 39$ deg. The horizontal lines show the expected saturated level of V_ℓ based on Eq. (68), which is consistent with the curves. Thus, our approximate treatment of the stochastic motion as a random walk appears to provide a consistent model of the evolution shown in Figure 8.

To show an example of the actual motion of angular-momentum vectors, the top panel of Figure 9 shows a time interval $\sim 7 \Omega_{\text{RMS}}^{-1}$ of the $\hat{\mathbf{L}}_i$ trajectory for two stars in a simulation similar to Figure 8. The two stars are chosen to have close to the mean eccentricity of the cluster. In this case, our model approximates their motion as ~ 10 steps of a random walk with an average step size of 30° . The time interval shown corresponds to ~ 3 relaxation timescales, and ~ 0.25 of the complete mixing timescale for $\ell = 1$. The bottom left panel of Figure 9 shows the torque as a function of time in units of $M_\bullet P / (\sqrt{Nm_{\text{RMS}}}) = \beta_\Omega \Omega_{\text{RMS}}^{-1} \approx \Omega_{\text{RMS}}^{-1}$ for the same stars. The bottom right panel of Figure 9 shows the torque as a function of time for a larger sample of stars: green curves show stars with nearly the median eccentricity,

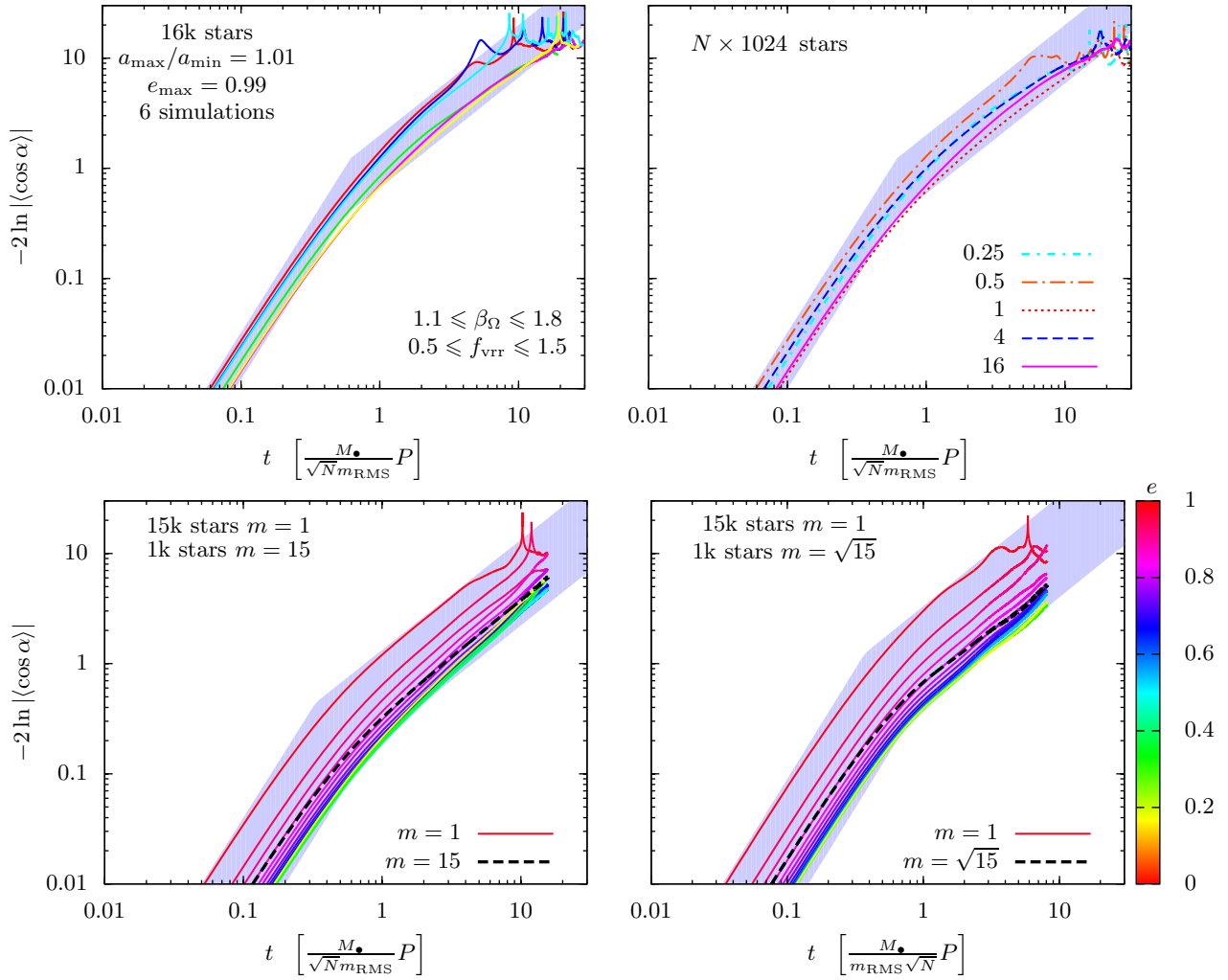


Figure 10. The angular variance $V_\ell(t)$ as in Figure 8, but for $\ell = 1$ and different initial conditions (top left), different numbers of stars (top right) and different RMS masses (bottom panels). *Top left:* Different curves show the range spanned by six simulations with different initial conditions. *Top right:* The number of stars N is varied between 256 and 16384, the legend shows $N/1024$. *Bottom left:* The stellar cluster is comprised of 15k low-mass and 1k high-mass stars (left) so the total mass Nm is the same for both groups. The curves show V_1 for stars grouped in subsets containing 1k members, sorted by mass and eccentricity (curves are colored by eccentricity as shown on the right); solid and dashed lines have different stellar masses as labeled. *Bottom right:* Similar to bottom left, but with heavy stars $\sqrt{15}$ × more massive than light stars. The shaded regions show $1.1 \leq \beta_\Omega \leq 1.8$ and $0.5 \leq f_{\text{vrr}} \leq 1.5$ (top panels), $0.5 \leq \beta_\Omega \leq 2$ and $0.75 \leq f_{\text{vrr}} \leq 4.5$ (bottom left), and $0.7 \leq \beta_\Omega \leq 3.0$ and $0.3 \leq f_{\text{vrr}} \leq 2.5$ (bottom right).

black curves show stars from the full range of eccentricities ($0 \leq e < 0.99$). The torques vary substantially from their initial values after a decoherence time $t_\phi \sim (0.3\text{--}0.7) \Omega_{\text{RMS}}^{-1}$, which is consistent with our earlier estimate from the angular variance. The decoherence time is similar for stars of all eccentricities.

Figure 10 shows $V_\ell(t)$ in simulations with different initial conditions, numbers of stars, and distributions of stellar masses. In these simulations we continue to assume that all stars have nearly the same semimajor axis, a spherical distribution in angular-momentum space, and a thermal distribution of eccentricities as in Figure 8. We find that Eq. (79) describes well the dependence of the relaxation timescale t_{vrr} on the number of stars, although the fitted value of f_{vrr} can vary by 30–40% for different initial conditions. In particular, in the upper right panel we vary the number of stars by a factor 64 but the variation in scaled time at a fixed value of

V_1 is less than a factor of two, and shows no systematic trend with N . Complete mixing occurs when the angular variance saturates, which in these simulations occurs at $t_{\text{sat}} \sim 10\text{--}30 t_{\text{vrr}}$. Note however that some of the curves do not display a perfectly linear growth during incoherent evolution; in various runs $V_\ell(t)$ exhibits time dependence both shallower and steeper than linear. Similar anomalous diffusion is often observed in chaotic systems near phase transitions, in random walks where the probability distribution of step size is top-heavy, and in systems with long-term memory (Latora et al. 1999; Kumar et al. 2010; Gottwald & Melbourne 2013; see also Gürkan 2011 and Bar-Or et al. 2013 for related findings in scalar resonant and two-body relaxation, respectively).

The simulations in the bottom panels contain two groups of stars with the same total mass Nm (bottom left panel) and the same value of $\sqrt{N}m$ (bottom right panel); the RMS masses in the clusters are $m_{\text{RMS}} = 3.87$ and 1.40

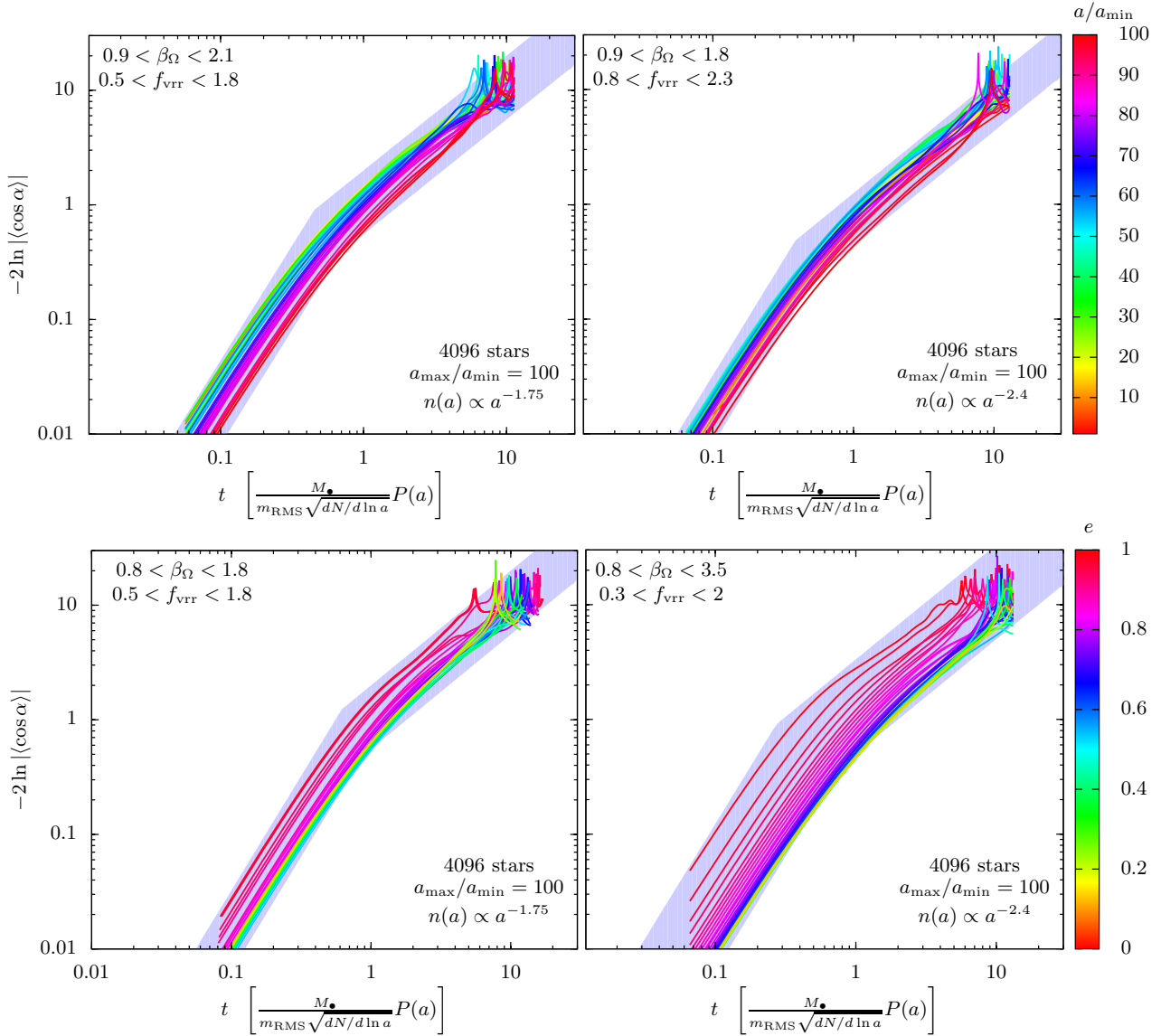


Figure 11. VRR in a stellar cluster with a range of eccentricity $0 \leq e \leq 0.99$ ($dN = 2ede$) and semimajor axis $a_{\max}/a_{\min} = 100$ with number density $n(a) \propto a^{-1.75}$ (left panels) and $r^{-2.4}$ (right panels). We sort the stars with respect to their semimajor axis (top panels) and eccentricity (bottom panels) and group them into 32 bins containing 128 stars each. The 32 curves in each panel shows $V_1 = -2 \ln |\cos \alpha_i|$ as in Figure 10 for the stars in the corresponding bins where α_i is the angular distance traversed by star i in dimensionless time $\tau = t/[M_\bullet m_{\text{RMS}}^{-1} (dN/d \ln a)^{-1/2} P(a)]$ from some reference time t_0 . We average over i and t_0 for each τ . The evolution of this quantity is quadratic in the initial coherent phase and linear during incoherent random mixing. The curves are colored according to the semimajor axis (top) or eccentricity (bottom panels) as shown on the right. The main systematic effect with semimajor axis is well captured by the relaxation time formula, the curves nearly overlap in these units despite a range of a factor of 56 (left panels) or 250 (right panels) in $t_{\text{VRR}}(a)$. Residual variations are probably due to edge effects: stars near a_{\min} and a_{\max} relax slower. Since the curves nearly overlap for $e < 0.7$, stars with small to moderately large eccentricities relax at nearly the same rate given by $t_{\text{VRR}}(a)$. However highly eccentric orbits $e > 0.8$ relax by up to a factor 4–8 faster. The eccentricity dependence in the coherent phase of the simulation is in perfect agreement with the direct calculation shown in Figure 7.

respectively. Here $V_1(t)$ is shown for 1k element bins sorted by mass and eccentricity, with solid curves showing the low-mass stars, colors representing eccentricity as shown on the right, and dashed black curves showing the high-mass stars. We find that the predicted scaling with m_{RMS} captures the mass dependence well. The relaxation is approximately eccentricity independent for $e \lesssim 0.8$, and it is systematically faster for more eccentric orbits, but the decoherence time is roughly independent of eccentricity even for very eccentric

orbits. This is consistent with the observation that the mean field of the cluster is dominated by stars with $e \lesssim 0.8$ (64% of stars have $e < 0.8$) and the torque decreases weakly with eccentricity; thus the torque is approximately constant until the stars with $e \lesssim 0.8$ are re-oriented.

Next let us relax the assumption of a fixed semimajor axis. We distribute the orbits between $a_{\max}/a_{\min} = 100$, and integrate for ~ 10 relaxation times at the outer edge of the cluster or $\sim 10^3$ relaxation times at the inner edge of the

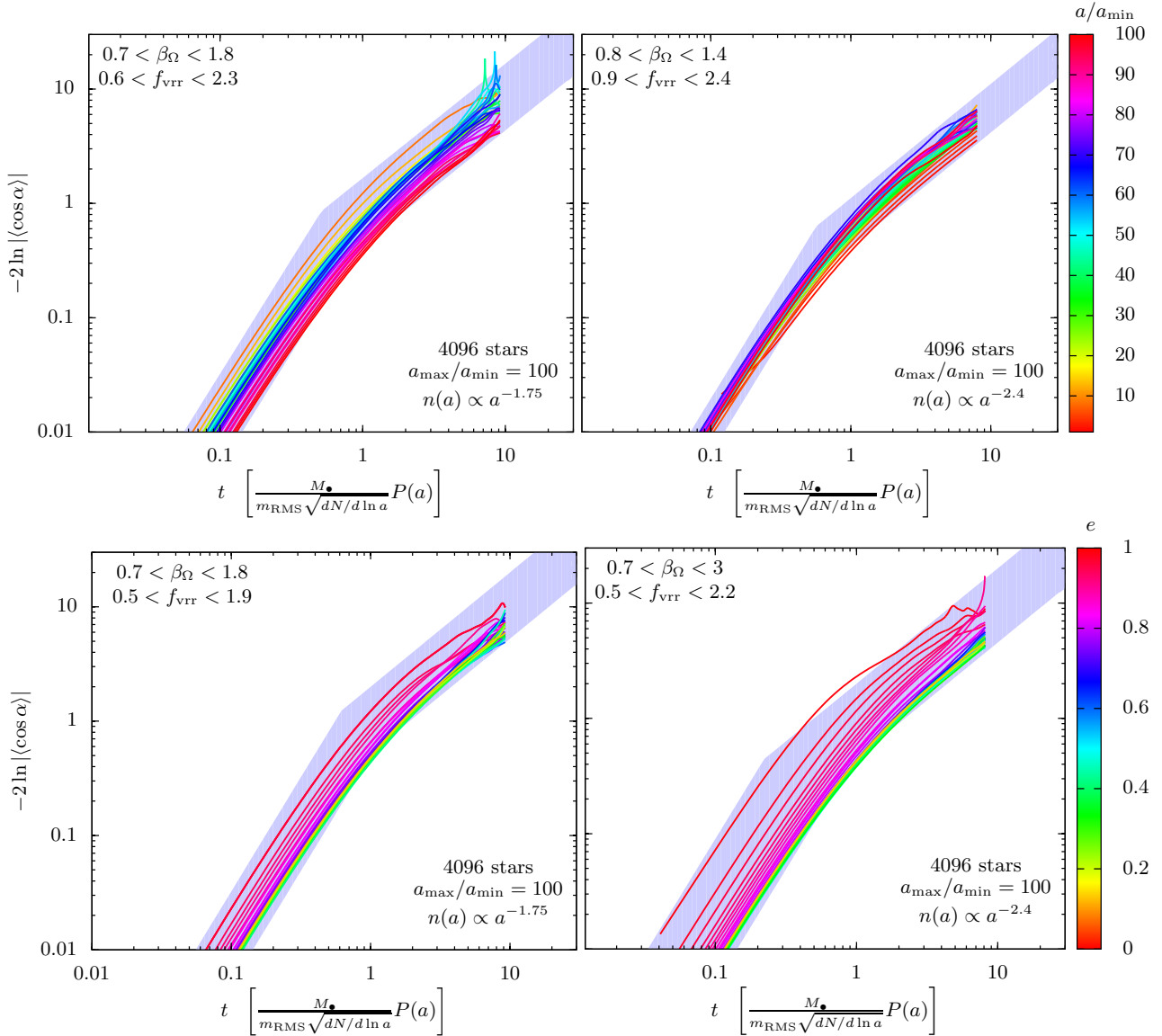


Figure 12. Same as Figure 11 but with an eccentricity distribution that is thermal below $e = 0.4$ and flat at higher eccentricities, $dN \propto e de$ for $e < 0.4$ and $dN \propto de$ otherwise. The trends are very similar. The interaction calculation $J_{ij\ell}$ was truncated above multipole harmonic index $\ell_{\max} = 20$ in this figure, and above 50 in Figure 11.

cluster. To maintain numerical accuracy for such a large dynamic range, we reduce the number of stars to 4 thousand. Each star has the same mass and a thermal distribution of eccentricity ($dN = 2e de$). We bin the stars according to semimajor axis or eccentricity to look for systematic effects in the relaxation time. Figure 11 shows the result of two simulations with number density profiles $n(r) \propto r^{-1.75}$ and $r^{-2.4}$ respectively, which correspond to the observed distribution of B-stars and Wolf-Rayet/O stars, respectively (Bartko et al. 2010). We find that the dependence of the relaxation time $t_{\text{vrr}}(a)$ on semimajor axis a is given approximately by Eq. (81). Indeed, despite a range of a factor of $(0.3\text{--}6) \times 10^4$ in the number density as a function of semimajor axis, there is less than a factor ~ 3 variation in the angular variance $V_1(t)$ when time is measured in units of $t_{\text{vrr}}(a)$ as given by Eq. (79). This is only a little larger than the factor ~ 2 variation seen for different realizations of the

initial conditions (cf. top left panel of Figure 10). Moreover most of this variation is seen for stars with semimajor axes near the cutoffs at a_{\max} and a_{\min} , and so are probably due to “edge effects”.

The bottom panels of Figure 11 show the dependence of the relaxation rate on eccentricity: the rate is nearly independent of eccentricity for $e \lesssim 0.7$, but orbits with $e \gtrsim 0.8$ relax faster on average, by as much as a factor of 4–8. This behavior is in good agreement with the direct calculation of β_T and β_Ω shown in Figure 7. Highly eccentric orbits have a much larger β_Ω ; therefore they are re-oriented more rapidly and have a larger angular coherence length. However, the decoherence time is roughly independent of eccentricity since the torques are dominated by stars with $e \lesssim 0.7$ which have similar β_Ω and therefore are re-oriented at similar rates. Figure 12 shows the evolution in the case where the number of high-eccentricity stars is smaller, but the re-

sults are very similar. The figures show that $\beta_\Omega = 0.95 \pm 0.1$ and $f_{\text{VRR}} = 1.9 \pm 0.2$ for $e < 0.7$, while for orbits with $e > 0.8$ β_Ω and f_{VRR} are larger and smaller by up to factors of ~ 3.5 and 5, respectively.

4.3 Comparison with previous results

In this paper, we have explored an idealized model of how orbits in a spherical stellar system undergo re-orientation due to torques from other orbits. Our model is based on the approximation that the rate of apsidal precession is much faster than the rate at which the orbital planes change their orientation. This approximation is valid because the ratio of the re-orientation time to the apsidal precession time in a cluster of $N \gg 1$ stars scales as \sqrt{N} (see Section 1) which is likely to be valid for most stars in the Galactic center with semimajor axes between ~ 0.003 pc and ~ 1 pc (see Section 2.1 and Figure 1 of KT11).

There are many previous studies of resonant relaxation (Rauch & Tremaine 1996; Hopman & Alexander 2006; Gürkan & Hopman 2007; Eilon et al. 2009; Perets et al. 2009; Gualandris & Merritt 2009; Merritt et al. 2010; Gürkan 2011; Madigan et al. 2011; Merritt et al. 2011; Merritt & Vasiliev 2011; Sabha et al. 2012; Antonini & Merritt 2013). Some of these studies only computed the torques between fixed Kepler ellipses, which are not relevant in the regime considered here where the apsidal precession is faster than the re-orientation of the ellipse. Some employed direct N-body simulations, which in principle are more accurate than the approximations used here. However, due to the computational cost of studying slow processes such as VRR with direct N-body simulations, earlier studies were restricted to either (i) small- N systems, in which the vector and scalar resonant relaxation timescales are not well-separated, or (ii) following the N-body system for less than the apsidal precession period, so the torque parameters β_T and β_Ω (Eq. 74) were measured for Keplerian ellipses rather than annuli. Thus, either they did not measure the long-term average values of β_T and β_Ω that are relevant for VRR, or they did not measure the coefficient f_{VRR} (Eq. 79) that parametrizes incoherent VRR. We believe that the simulations in this paper provide the first detailed study of VRR that represents both the coherent and incoherent evolution for systems with a large number of stars.

When comparing with earlier studies, we must account for definitions of β in these papers that are slightly different from ours:

- Rauch & Tremaine (1996) defined β^{RT} using $\langle \|\mathbf{T}_i\| \rangle = \beta^{\text{RT}} (2\pi)^{-1} \sqrt{NGm^2}/a_i$ where N denotes the total number of stars. They carried out N-body simulations with $64 \leq N \leq 8192$ and a range of semimajor axes $a_{\text{max}}/a_{\text{min}} = 10$, with $n(a) \propto a^{-\gamma}$, $\gamma = 2$, and a thermal distribution of eccentricities for $e \leq e_{\text{max}} = 0.8$. Only 64 “active” stars interacted self-consistently; the rest exerted torques on the active stars but followed fixed orbits in either a point-mass or an isochrone potential (the isochrone was used to experiment with the effect of rapid apsidal precession). They measured β^{RT} as $\beta^{\text{RT}} \equiv \langle 2\pi a_i \|\mathbf{T}_i\| \rangle / (\sqrt{NGm^2}) = (M_\bullet / \sqrt{Nm}) \langle \|\mathbf{T}_i\| P_i / L_{c,i} \rangle_i$, where $L_{c,i} = m\sqrt{GM_\bullet a_i}$ is the angular momentum of a cir-

cular orbit. To compare this to our β_T we must make two corrections. First, for a two-dimensional Gaussian distribution (\mathbf{T} perpendicular to \mathbf{L}) $\langle \|\mathbf{T}\| \rangle = \frac{1}{2}\pi^{1/2} T_{\text{RMS}}$. Second, we measure β_T using $dN/d \ln a$ whereas they use N ; to make the conversion we note from Appendix D that in a power-law density distribution β_T and hence $a \|\mathbf{T}\| / \sqrt{dN/d \ln a}$ is independent of a , so we have $\langle a_i \|\mathbf{T}_i\| \rangle / \sqrt{N} = (a_i \|\mathbf{T}_i\| / \sqrt{N}) \langle \sqrt{dN/d \ln a} \rangle / \sqrt{dN/d \ln a_i}$. Then for the assumed number density profile ($\gamma = 2$, $a_{\text{max}}/a_{\text{min}} = 10$), we have $\beta^{\text{RT}} = \frac{1}{2} f_e \pi^{1/2} \beta_T \int_{a_{\text{min}}}^{a_{\text{max}}} dN (dN/d \ln a)^{1/2} / (N^{1/2} \int_{a_{\text{min}}}^{a_{\text{max}}} dN) = 0.670 f_e \beta_T$, where $f_e \simeq 1.2$ is a correction arising because Rauch & Tremaine did not have any stars with $e > e_{\text{max}} = 0.8$ (cf. Fig. 6). They measured $\beta^{\text{RT}} = 1.8 \pm 0.1$ in the Kepler case where the background stars had no apsidal precession due to the unperturbed potential, and $\beta^{\text{RT}} = 0.7 \pm 0.1$ in the isochrone case with rapid apsidal precession, corresponding to $\beta_T = 2.2 \pm 0.1$ and $\beta_T = 0.9 \pm 0.1$, respectively.

- Gürkan & Hopman (2007) defined β^{GH} using $\langle \|\mathbf{T}_i\| \rangle = \beta^{\text{GH}} \sqrt{N(< 2a_i) Gm^2}/a_i$, where $N(< 2a_i)$ denotes the number of stars with semimajor axis less than $2a_i$. They calculated the orbit-averaged torques for fixed Keplerian wires using $N = 10,000$ stars with density $n(a) \propto a^{-\gamma}$ and $\gamma = 1.4$. They found that the mean absolute torque along the minor axis of the orbit increased with eccentricity and conversely along the major axis, such that the total torque increased with eccentricity as $\beta^{\text{GH}} = 1.76(e^2 + 0.5)/2\pi$ with an average over the eccentricity distribution ($dN/de \propto 2e$) $\langle \beta^{\text{GH}} \rangle = 1.76/2\pi$ and an RMS $\langle (\beta^{\text{GH}})^2 \rangle^{1/2} = 1.83/2\pi$. For a power-law density distribution our definition of the torque parameter is related to theirs as $2\pi \beta^{\text{GH}} = \pi^{1/2} (3-\gamma)^{1/2} 2^{(\gamma-5)/2} \beta_T$. For $\gamma = 1.4$ this yields $2\pi \beta^{\text{GH}} = 0.64 \beta_T$, so their result implies $\beta_T = 2.7(e^2 + 0.5)$. Averaging over a thermal distribution of eccentricities yields $\langle \beta_T \rangle = 2.6$ and $\langle \beta_T^2 \rangle^{1/2} = 2.9$.
- Eilon et al. (2009) defined β^{EAK} using a similar definition as Rauch & Tremaine (1996), $\langle \|\mathbf{T}_i\| \rangle = \beta^{\text{EKA}} (2\pi)^{-1} \sqrt{NGm^2}/a$. They conducted a number of N-body simulations with $N = 200$ and a variety of semimajor axis distributions, number density $n \propto a^{-\gamma}$ with $1 \leq \gamma \leq 1.75$. They noted that the torque perpendicular to $\hat{\mathbf{L}}$ was mostly along the instantaneous minor axis of the orbit, as in Gürkan & Hopman (2007). Using the same arguments as for Rauch & Tremaine (1996), we get that $\beta^{\text{EKA}} = 0.68 \beta_T$ and $0.69 \beta_T$ for $\gamma = 1.75$ and $\gamma = 1$, respectively. Measuring the re-orientation correlation function for a few precession times, they found $\beta^{\text{EKA}} = 1.83 \pm 0.03$, which implies $\beta_T = 2.7$.

For comparison, our calculations yield $\beta_T \simeq 0.85 \pm 0.1$ (Eq. 75 and Fig. 7), which is a factor 3 smaller than the results reported by Rauch & Tremaine (1996), Gürkan & Hopman (2007), and Eilon et al. (2009). The systematically higher value of β_T found in these investigations arises because the torque on an orbit was averaged over a timescale short compared to the apsidal precession period¹⁵. As shown by these studies, the largest component of the

¹⁵ The rate of re-orientation, as measured by β_T , can be even more rapid on timescales shorter than or comparable to the orbital period (Merritt et al. 2010; Sadeghian & Will 2011; Sabha et al. 2012).

torque is parallel to the minor axis of the Keplerian orbit; as the orbit precesses, the direction of the largest torque precesses as well so the mean torque averaged over a precession period is smaller than the mean torque averaged over the orbital period. The use of torques averaged over the apsidal precession period rather than the orbital period is necessary to estimate the rate of VRR on timescales longer than the apsidal precession period, so long as apsidal precession is much faster than nodal precession. This requirement is satisfied for stars of small to moderate eccentricity at all radii in the Galactic centre (see Fig. 1 of KT11), but can fail for nearly radial orbits at large or small radii (see footnote 1).

An observation that supports this argument is that our estimate $\beta_T \simeq 0.85 \pm 0.1$ matches the estimate $\beta_T = 0.9 \pm 0.1$ reported by Rauch & Tremaine (1996) for the isochrone potential, in which the stars are subject to rapid apsidal precession. Furthermore, a similar rate of vector resonant relaxation was found using direct N-body simulations, which looked at the long term behavior of orbits close to the SMBH including relativistic corrections (Kupi & Alexander, private communication¹⁶). Their rate of re-orientation may be fitted by $\|\Delta \mathbf{L}\|/L = c_0(\beta_{T,0} + \beta_{T,1})t/t_\omega$ if $t \lesssim t_\omega$, and $c_0[\beta_{T,0}(t/t_\omega)^{1/2} + \beta_{T,1}(t/t_\omega)]$ if $t_\phi \gtrsim t \gtrsim t_\omega$, where $\beta_{T,0} + \beta_{T,1} \simeq 2.7$, $\beta_{T,1} \simeq 0.9$, t_ω is the apsidal precession time, and c_0 is a constant. Thus, part of the initial coherent torque becomes incoherent over timescales longer than the apsidal precession time t_ω , leaving a much smaller coherent component thereafter.

An additional limitation of earlier studies is that they could not accurately characterize the properties of the random walk for the direction $\hat{\mathbf{L}}_i$ during the incoherent phase of VRR (i.e., the parameter f_{vrr} of Eq. 79), mainly due to the computational cost of long N-body integrations. Furthermore, previous simulations were restricted to a small number of self-consistently interacting stars (between 50 and 200) in which complete mixing sets in much earlier (Eqs. 69)–(70) which makes the measurement of the parameters of the incoherent phase more difficult.¹⁷ Finally, previous analyses used the simplified model $\langle \|\mathbf{L}(t + t_0) - \mathbf{L}(t_0)\|/L \rangle \propto (t/t_{\text{vrr}})^{1/2}$ to characterize VRR, which is not appropriate if the angular coherence length is of order unity; it is for this reason that we developed the analysis in Section 4.1 based on the random walk on the sphere.

5 SUMMARY

We have introduced a new integrator, N-RING, to simulate vector resonant relaxation in stellar clusters around supermassive black holes. N-RING integrates Hamilton’s equations for N stars, averaged over the orbital period and apsidal precession. The code uses a multipole expansion (up to $\ell_{\text{max}} = 50$ in our experiments) of the averaged inter-particle potential. The code decomposes the evolution into pairwise interactions, integrates the averaged Hamiltonian exactly for each pairwise interaction, and iterates over all $\frac{1}{2}N(N-1)$

such interactions, thereby conserving the total angular momentum exactly. The coupling coefficients for different multipole moments are generally complicated functions of the semimajor axis and eccentricity, but can be calculated once and for all at the start of the integration.

We have shown how to make the algorithm time-reversible and n^{th} order accurate (up to $n = 8$ in our experiments). We constructed a parallelization scheme, and increased the efficiency using a time-block refinement and operator ordering. Using a small computer cluster of 32 cores, this integrator can accurately integrate the evolution of a cluster of $\sim 10^4$ stars with a large range of radii for ~ 10 relaxation times within 7 days.

The major challenges that limit the speed of the code include the following.

- (i) The coupling coefficients driving resonant relaxation can be strongly enhanced for orbits with nearly coincident periapsides or apoapsides (see bottom panels of Figure 1).
- (ii) For radially overlapping orbits the coupling coefficients decline relatively slowly, as ℓ^{-2} , implying that all multipoles up to $\ell \sim 1/I$ contribute equally to the motion for orbital inclination I .
- (iii) The precession frequency between two radially overlapping orbits diverges as their mutual inclination approaches zero.
- (iv) Gravitational N-body integrations of star clusters, galaxies, or large-scale structure benefit from the fact that most stars are at large distances ($N \sim r^3$) so their collective gravitational potential can be approximated by a few multipole moments; in contrast, in the averaged problem investigated by N-RING each star can interact strongly with all stars having radially overlapping orbits. Thus there are no simple ways to reduce the number of calculations per timestep below $O(N^2)$. However, parallel execution on N processors can reduce the computation time to $O(N)$.

We derived a stochastic model to describe a random walk with an arbitrary distribution of step sizes on the unit sphere. Expanding the probability distribution in spherical harmonics shows that the amplitudes of the spherical harmonics with $\ell > 0$ decay exponentially during a spherical random walk. The angular variance $V_\ell \equiv -2\ell^{-1}(\ell + 1)^{-1} \ln \langle P_\ell(\cos \alpha) \rangle$ grows linearly in time where α is the angular distance traversed by an orbit normal in time t and $P_\ell(\cdot)$ are Legendre polynomials.

We have investigated the long-term evolution of spherical stellar systems with up to 16k stars, spanning a factor of up to 100 in semimajor axis. The simulations confirm that the orbital orientation vectors initially evolve coherently ($V_\ell \propto t^2$) and then undergo a spherical random walk ($V_\ell \propto t$) until the system becomes fully mixed. The RMS step size of the random walk in our simulations is $\alpha_{\text{RMS}} \simeq 0.5$ –1 radians and full mixing requires $(\ln 3N)/\alpha_{\text{RMS}}^2$ timesteps where N is the number of stars.

In the initial coherent phase of vector resonant relaxation, the RMS torques can be calculated exactly (Appendix D and Figures 6 and 7). This confirmed the analytical scaling relations with semimajor axis, number density, and component mass, and showed perfect agreement with the simulations. In particular, the torque parameter

¹⁶ talk presented at Stars and Singularities, Benozio Center for Astrophysics Workshop Series, Rehovot, Israel, http://www.weizmann.ac.il/home/tal/Workshop09/talk_files/Kupi.pdf

¹⁷ Eilon et al. (2009) defined $f_{\text{vrr}} = 1/(A_\phi \beta_\Omega^2)$, where A_ϕ , set by the decoherence time in Eq. (80), was not determined.

is $\beta_T = 0.8\text{--}1.5$ (see Eq. 74 and Figure 6) for different eccentricities. The rate of re-orientation of the orbital plane follows a similar scaling with $\beta_\Omega = \beta_T/(1 - e^2)^{1/2}$ (Eq. 75). We found that the torques are generally weakly decreasing functions of the eccentricity in spherical clusters during vector resonant relaxation, and in particular for a thermal eccentricity distribution $\beta_T \simeq 1.05 - 0.3e$. The rate of re-orientation of the orbit axis is approximately independent of eccentricity for $e \lesssim 0.7$, and much faster only for $e \gtrsim 0.8$. The rate of re-orientation is smaller than has been observed in most¹⁸ N-body simulations by a factor ~ 3 , and most of this difference arises because the torque perpendicular to the angular-momentum vector is smaller when apsidal precession is rapid.

Our simulations confirm the formula for the vector resonant relaxation timescale derived from a model of the relaxation as a random walk on the sphere (Eq. 79) and imply that the parameter $f_{\text{vrr}} \simeq 0.5\text{--}2.1$ depending mainly on eccentricity (Figures 11 and 12). In a thermal distribution of eccentricities ($dN \propto 2e\,de$), we find that highly eccentric orbits $e \gtrsim 0.8$ relax faster by up to a factor 5; however, the vector resonant relaxation time for low- and moderate-eccentricity orbits with $e \lesssim 0.7$ is practically independent of eccentricity with $f_{\text{vrr}} \simeq 1.9 \pm 0.2$. The simulations also show that the decoherence time of vector resonant relaxation is roughly independent of eccentricity in the full eccentricity range. The angular-momentum vectors in the inner regions of our simulated cluster undergo a stochastic random walk already when the vectors in the outer parts of the cluster are still experiencing a coherent torque. For a cluster with a given number of stars, the relaxation rate is proportional to the RMS stellar mass of the stellar cluster. Thus the primary uncertainty in estimating the vector resonant relaxation near the Galactic centre is the mass function of stars, stellar remnants, gas clouds, etc.: the RMS stellar mass diverges even for a Salpeter mass function unless a maximum-mass cutoff is imposed, and the mass function in the Galactic centre is believed to be more top-heavy than in the solar neighbourhood (see KT11 and references therein).

We found that the Markovian random walk on a sphere gives a good approximate description of the long-term evolution under vector resonant relaxation. However, in some cases the temporal correlation function displays deviations from this model even after averaging over several mixing timescales (Figure 10), which possibly indicates some level of persistent long-term memory in these stellar systems. In the future we will use N-RING to examine resonant dynamical friction and vector resonant relaxation in anisotropic systems.

The purpose of this paper has been twofold: first, to develop an efficient and general numerical algorithm for simulating vector resonant relaxation, and second, to relate the simple analytic description of vector resonant relaxation to quantitative results from our simulations of model star clusters surrounding central black holes.

¹⁸ Except for the isochrone simulations of Rauch & Tremaine (1996) and Kupi & Alexander, as described in Section 4.3.

ACKNOWLEDGMENTS

BK was supported in part by the W.M. Keck Foundation Fund of the Institute for Advanced Study and NASA grants NNX11AF29G and NNX14AM24G. Simulations were run on the Harvard Odyssey, CfA/ITC, and IAS clusters.

REFERENCES

- Alexander R. D., Armitage P. J., Cuadra J., 2008, MNRAS, 389, 1655
 Antonini F., Merritt D., 2013, ApJ, 763, L10
 Bar-Or B., Alexander T., 2014, Classical and Quantum Gravity, 31, 244003
 Bar-Or B., Kupi G., Alexander T., 2013, ApJ, 764, 52
 Bartko H., Martins F., Fritz T., Genzel R., Levin Y., Perets H., Paumard T., Nayakshin S., Gerhard O., Alexander T., Dodds-Eden K., Eisenhauer F., Gillessen S., Mascetti L., Ott T., Perrin G., Pfuhl O., Reid M., 2009, ApJ, 697, 1741
 Bartko H., Martins F., Trippe S., Fritz T., Genzel R., Ott T., Eisenhauer F., Gillessen S., Paumard T., Alexander T., Dodds-Eden K., Gerhard O., Levin Y., Mascetti L., Nayakshin S., Perets H., Perrin G., Pfuhl O., 2010, ApJ, 708, 834
 Binney J., Tremaine S., 2008, Galactic Dynamics, 2nd Edition. Princeton University Press, Princeton NJ
 Byrd P., Friedman M., 1971, Handbook of Elliptic Integrals for Engineers and Scientists. Springer-Verlag, Berlin
 Casas F., Murua A., Nadinic M., 2012, Computer Physics Communications, 183, 2386
 Coffey W. T., Kalmykov Y. P., 2012, The Langevin Equation: With Applications to Stochastic Problems in Physics, Chemistry and Electrical Engineering (3rd Edition). World Scientific, Singapore
 Debye P., 1929, Polare Molekeln. Hirzel, Leipzig
 Eilon E., Kupi G., Alexander T., 2009, ApJ, 698, 641
 Gottwald G. A., Melbourne I., 2013, Proc. Nat. Acad. Sci., 110, 8411
 Gualandris A., Merritt D., 2009, ApJ, 705, 361
 Gürkan M., 2011, MNRAS, 411, L56
 Gürkan M., Hopman C., 2007, MNRAS, 379, 1083
 Hopman C., 2009, ApJ, 700, 1933
 Hopman C., Alexander T., 2006, ApJ, 645, 1152
 Ivanov P. B., Polnarev A. G., Saha P., 2005, MNRAS, 358, 1361
 Jackson J. D., 1998, Classical Electrodynamics, 3rd Edition. Wiley-VCH, New York
 Kocsis B., Tremaine S., 2011, MNRAS, 412, 187 (KT11)
 Kumar N., Harbola U., Lindenberg K., 2010, Phys. Rev. E, 82, 021101
 Latora V., Rapisarda A., Ruffo S., 1999, Phys. Rev. Lett., 83, 2104
 Löckmann U., Baumgardt H., Kroupa P., 2009, MNRAS, 398, 429
 Madigan A.-M., Hopman C., Levin Y., 2011, ApJ, 738, 99
 Merritt D., 2013, Dynamics and Evolution of Galactic Nuclei. Princeton University Press, Princeton NJ
 Merritt D., Alexander T., Mikkola S., Will C. M., 2010, Phys. Rev. D, 81, 062002
 Merritt D., Alexander T., Mikkola S., Will C. M., 2011, Phys. Rev. D, 84, 044024

- Merritt D., Vasiliev E., 2011, *ApJ*, 726, 61
Merritt D., Vasiliev E., 2012, *Phys. Rev. D*, 86, 102002
Perets H. B., Gualandris A., Kupi G., Merritt D., Alexander T., 2009, *ApJ*, 702, 884
Pfuhl O., Alexander T., Gillessen S., Martins F., Genzel R., Eisenhauer F., Fritz T. K., Ott T., 2014, *ApJ*, 782, 101
Rauch K., Tremaine S., 1996, *New Astr.*, 1, 149
Roberts P., Ursell H., 1960, *Phil. Trans. R. Soc. Lond. A*, 252, 317
Sabha N., Eckart A., Merritt D., Zamaninasab M., Witzel G., García-Marín M., Jalali B., Valencia-S. M., Yazici S., Buchholz R., Shahzamanian B., Rauch C., Horrobin M., Straubmeier C., 2012, *A&A*, 545, A70
Sadeghian L., Will C. M., 2011, *Classical and Quantum Gravity*, 28, 225029
Saha P., Tremaine S., 1994, *AJ*, 108, 1962
Schödel R., Eckart A., Alexander T., Merritt D., Genzel R., Sternberg A., Meyer L., Kul F., Moulata J., Ott T., Straubmeier C., 2007, *A&A*, 469, 125
Suzuki M., 1990, *Physics Letters A*, 146, 319
Suzuki M., 1994, *Physica A*, 205, 65
Touma J., Tremaine S., Kazandjian M., 2009, *MNRAS*, 394, 1085
Tremaine S., 2005, *ApJ*, 625, 143
Trotter H., 1959, *Proc. Amer. Math. Soc.*, 10, 545
Tuckerman M., Berne B., Martyna G., 1992, *Jour. Chem. Phys.*, 97, 1990
Yoshida H., 1990, *Physics Letters A*, 150, 262

APPENDIX A: APSIDAL PRECESSION

We calculate the apsidal precession rate Ω_{prec} of stellar orbits due to the gravitational field from a spherical near-Keplerian stellar system. For a stellar system with enclosed mass $M_*(r) \ll M_\bullet$ we have (Tremaine 2005)

$$\Omega_{\text{prec}} = \frac{\Omega}{\pi M_\bullet e} \int_0^\pi d\psi M_*[r(\psi)] \cos \psi \quad (\text{A1})$$

where $\Omega = (GM_\bullet)^{1/2} a^{-3/2}$ is the average orbital angular frequency, ψ is the true anomaly, and the radius is given by $r(\psi) = p/(1 + e \cos \psi)$, where e is the eccentricity, $p = a(1 - e^2)$ is the semi-latus rectum, and a is the semimajor axis. The precession is retrograde for any positive-definite spherical mass distribution (Tremaine 2005).

The integral can be simplified for power-law mass distributions of the form¹⁹ $M_*(r) = M_0(r/r_0)^s$. In this case (Ivanov et al. 2005)

$$\Omega_{\text{prec}} = \frac{\Omega}{\pi e} \frac{M_0}{M_\bullet} \left(\frac{p}{r_0}\right)^s \int_0^\pi \frac{\cos \psi d\psi}{(1 + e \cos \psi)^s} = \Omega \frac{M_0}{M_\bullet} \left(\frac{a}{r_0}\right)^s \frac{(1 - e^2)^{(s+1)/2}}{e^2} [P_{s-2}(\chi) - \chi P_{s-1}(\chi)] \quad \text{where } \chi \equiv \frac{1}{\sqrt{1 - e^2}}. \quad (\text{A2})$$

Here P_n denotes the Legendre function of order n . In terms of the density $\rho(r) = (4\pi r^2)^{-1} dM(r)/dr$, we have

$$\Omega_{\text{prec}} = \frac{4\pi G \rho(a)}{\Omega s} \frac{(1 - e^2)^{(s+1)/2}}{e^2} [P_{s-2}(\chi) - \chi P_{s-1}(\chi)] \quad \text{where } \chi \equiv \frac{1}{\sqrt{1 - e^2}}. \quad (\text{A3})$$

For $e \rightarrow 0$ and arbitrary $s > 0$,

$$\Omega_{\text{prec}} = -\frac{2\pi G \rho(a)}{\Omega} \left[1 + \left(\frac{1}{4} - \frac{5s}{8} + \frac{s^2}{8} \right) e^2 + \mathcal{O}(e^4) \right]. \quad (\text{A4})$$

For some values of s there are analytic expressions valid for all eccentricities (Merritt 2013):

$$\Omega_{\text{prec}} = -\frac{2\pi G \rho(a)}{\Omega} \sqrt{1 - e^2} \times \begin{cases} 1 & \text{if } \rho(r) \propto r^{-1}, \quad s = 2 \\ 2/(1 + \sqrt{1 - e^2}) & \text{if } \rho(r) \propto r^{-2}, \quad s = 1. \end{cases} \quad (\text{A5})$$

APPENDIX B: INTERACTION ENERGY

Here we simplify the orbit- and precession-averaged interaction energy between two stars (Eq. 4), which is a four-dimensional integral over the two annular surfaces. The evaluation of this integral depends on the radial geometry of the two annuli. In particular let R_1 and R_2 be the set of all radii occupied by the annuli of the two orbits (e.g., $R_1 = \{r \mid r_{p1} \leq r \leq r_{a1}\}$ where r_{p1} and r_{a1} are the periaapsis and apoapsis of orbit 1). We call the orbits “non-overlapping” if they occupy disjoint ranges of radius, $R_1 \cap R_2 = \emptyset$; we say that orbit 1 is “embedded” in orbit 2 if $R_1 \subset R_2$; we call the orbits “identical” if $R_1 = R_2$ (even if the orbits are mutually inclined); and we say the orbits are “overlapping” if $R_1 \cap R_2 \neq \emptyset$ but $R_1 \not\subset R_2$ and $R_2 \not\subset R_1$.

We show that the interaction energy can be reduced to a sum over a series of one-dimensional integrals in the general case, and to a sum over a series of closed analytic expressions for non-overlapping or identical orbits.

We need first to find the gravitational potential energy between two circular rings of radius r and r' , inclined by an angle I . We expand the inverse distance in spherical harmonics²⁰,

$$\frac{1}{\|\mathbf{r} - \mathbf{r}'\|} = \sum_{\ell=0}^{\infty} \frac{4\pi}{2\ell + 1} \frac{\min(r, r')^\ell}{\max(r, r')^{\ell+1}} Y_{\ell m}^*(\theta, \varphi) Y_{\ell m}(\theta', \varphi'). \quad (\text{B3})$$

We orient the coordinate systems such that the unprimed ring lies in the equator. Then averaging the inverse distance over this ring is equivalent to averaging over φ , and in this average all terms except $m = 0$ disappear. Thus

$$\left\langle \frac{1}{\|\mathbf{r} - \mathbf{r}'\|} \right\rangle_\phi = \sum_{\ell=0}^{\infty} \frac{\min(r, r')^\ell}{\max(r, r')^{\ell+1}} P_\ell(0) P_\ell(\cos \theta'). \quad (\text{B4})$$

¹⁹ For the Galactic centre $s = 1.8$ and 1.25 for $r \lesssim 0.2$ pc and $r \gtrsim 0.2$ pc, respectively (Schödel et al. 2007; Löckmann et al. 2009).

²⁰ We use the orthonormal definition for spherical harmonics (Jackson 1998)

$$Y_{\ell m}(\theta, \varphi) = \sqrt{\frac{2\ell + 1}{4\pi} \frac{(\ell - m)!}{(\ell + m)!}} P_\ell^m(\cos \theta) e^{im\varphi}, \quad (\text{B1})$$

where $P_\ell^m(x)$ are associated Legendre polynomials, defined by

$$P_\ell^m(x) = \frac{(-1)^m}{2^\ell \ell!} (1 - x^2)^{m/2} \frac{d^{\ell+m}}{dx^{\ell+m}} (x^2 - 1)^\ell. \quad (\text{B2})$$

In particular for $m = 0$, $P_\ell^0(x) = P_\ell(x)$ are Legendre polynomials.

Now $\cos \theta' = \sin I \sin \psi$ where ψ is the azimuthal angle in the primed ring, measured from the line of nodes with the unprimed ring. Then

$$\frac{1}{2\pi} \int_0^{2\pi} d\psi P_\ell(\sin I \sin \psi) = P_\ell(0)P_\ell(\cos I), \quad (\text{B5})$$

where for integer $\ell \geq 0$ $P_\ell(0)$ is given by Eq. (6). With this result the average becomes

$$\left\langle \frac{1}{\|\mathbf{r} - \mathbf{r}'\|} \right\rangle_{\phi, \psi} = \sum_{\ell=0}^{\infty} \frac{\min(r, r')^\ell}{\max(r, r')^{\ell+1}} |P_\ell(0)|^2 P_\ell(\cos I). \quad (\text{B6})$$

Now the dependence of the interaction energy (4) on the radial and angular variables separates,

$$H_{\text{RR}}^{(ij)} = -G \sum_{\ell=0}^{\infty} R_\ell \Phi_\ell \quad (\text{B7})$$

where

$$R_\ell \equiv R_\ell(a_i, a_j, e_i, e_j) = \int_{r_{pi}}^{r_{ai}} dr \int_{r_{pj}}^{r_{aj}} dr' \sigma_i(r) \sigma_j(r') r r' \frac{\min(r, r')^\ell}{\max(r, r')^{\ell+1}} \quad (\text{B8})$$

and

$$\Phi_\ell = 4\pi^2 [P_\ell(0)]^2 P_\ell(\cos I) \quad (\text{B9})$$

which vanishes for odd ℓ .

The radial integral R_ℓ is evaluated using Eq. (3) for the surface density:

$$R_\ell = \frac{m_i m_j}{4\pi^4 a_i a_j} S_\ell \quad (\text{B10})$$

where

$$S_\ell = \int_{r_{pi}}^{r_{ai}} dr \int_{r_{pj}}^{r_{aj}} dr' \frac{r}{\sqrt{r - r_{pi}} \sqrt{r_{ai} - r}} \frac{r'}{\sqrt{r' - r_{pj}} \sqrt{r_{aj} - r'}} \frac{\min(r, r')^\ell}{\max(r, r')^{\ell+1}}. \quad (\text{B11})$$

In the following three subsections the calculation of S_ℓ is done separately for orbits that are non-overlapping, identical, and overlapping or embedded in radius.

The quantity S_ℓ is related to the dimensionless parameter s_ℓ defined in Eq. (7) by

$$s_\ell = \frac{S_\ell}{\pi^2 \alpha^\ell a_{\text{in}}}, \quad (\text{B12})$$

where $\alpha = a_{\text{in}}/a_{\text{out}}$, $a_{\text{in}} = \min(a, a')$, and $a_{\text{out}} = \max(a, a')$.

B1 Non-overlapping orbits

As usual, in this subsection the subscripts ‘‘in’’ and ‘‘out’’ denote the orbits with the smaller and larger semimajor axis. If there is no radial overlap then $r_{a,\text{in}} < r_{p,\text{out}}$, and we may assume $r_{\text{in}} = r'$ and $r_{\text{out}} = r$ throughout the integration domain in Eq. (B11). Thus the integrals can be evaluated independently.

$$S_\ell = \int_{r_{p,\text{out}}}^{r_{a,\text{out}}} dr \frac{r^{-\ell}}{\sqrt{r - r_{p,\text{out}}} \sqrt{r_{a,\text{out}} - r}} \int_{r_{p,\text{in}}}^{r_{a,\text{in}}} dr' \frac{r'^{\ell+1}}{\sqrt{r' - r_{p,\text{in}}} \sqrt{r_{a,\text{in}} - r'}}. \quad (\text{B13})$$

We can transform the first integral to the same form as the second by introducing the variable $u = 1/r$:

$$\int_{r_{p,\text{out}}}^{r_{a,\text{out}}} dr \frac{r^{-\ell}}{\sqrt{r - r_{p,\text{out}}} \sqrt{r_{a,\text{out}} - r}} = \frac{1}{\sqrt{r_{p,\text{out}} r_{a,\text{out}}}} \int_{u_{a,\text{out}}}^{u_{p,\text{out}}} du \frac{u^{\ell-1}}{\sqrt{u - u_{a,\text{out}}} \sqrt{u_{p,\text{out}} - u}} \quad (\text{B14})$$

After this change of variables both integrals in Eq. (B13) have the same algebraic form with a non-negative integer exponent in the numerator for $\ell > 0$:

$$\int_{x_{\text{min}}}^{x_{\text{max}}} dx \frac{x^n}{\sqrt{x - x_{\text{min}}} \sqrt{x_{\text{max}} - x}} = \pi (x_{\text{max}} x_{\text{min}})^{n/2} P_n \left(\frac{x_{\text{max}} + x_{\text{min}}}{2\sqrt{x_{\text{max}} x_{\text{min}}}} \right). \quad (\text{B15})$$

Now we set $x_{\text{max},\text{min}} = a(1 \pm e)$ (for $x = r$) or $x_{\text{max},\text{min}} = 1/[a(1 \mp e)]$ (for $x = u$), and we obtain

$$S_\ell = \pi^2 \frac{a_{\text{in}}^{\ell+1} (1 - e_{\text{in}}^2)^{(\ell+1)/2}}{a_{\text{out}}^\ell (1 - e_{\text{out}}^2)^{\ell/2}} P_{\ell+1}(\chi_{\text{in}}) P_{\ell-1}(\chi_{\text{out}}) \quad \text{where} \quad \chi \equiv \frac{1}{\sqrt{1 - e^2}} \quad (\ell > 0). \quad (\text{B16})$$

For $\ell = 0$ we can directly use Eq. (B13), which can be evaluated using Eq. (B15) with $n = 0$ and 1 to yield $S_0 = \pi^2 a_{\text{in}}$.

B2 Identical orbits

Next we discuss the special case where $r_{p,\text{in}} = r_{p,\text{out}}$ and $r_{a,\text{in}} = r_{a,\text{out}}$, which also admits a closed-form solution. The technique introduced here may be generalized for the overlapping or embedded cases as we show in the following subsection.

In this case the integrals over $r < r'$ and $r > r'$ are identical. We calculate the contribution from $r < r'$. Change integration variables in Eq. (B11) $(r, r') \rightarrow (\phi, \phi')$ such that $r = a(1 + e \cos \phi)$

$$S_\ell = 2a \int_0^\pi d\phi \int_0^\phi d\phi' \frac{(1 + e \cos \phi)^{\ell+1}}{(1 + e \cos \phi')^\ell} \quad (\text{B17})$$

In this section we use the following shorthand notation to simplify the expressions

$$h \equiv \frac{1}{e}, \quad s \equiv \frac{1-e}{2e}. \quad (\text{B18})$$

First we evaluate the ϕ' integral. We may eliminate the ℓ dependence in the denominator by realizing that it is the $(\ell - 1)^{\text{th}}$ complete derivative with respect to h ,

$$\int_0^\phi d\phi' \frac{1}{(1 + e \cos \phi')^\ell} = \frac{(-1)^{\ell-1}}{(\ell - 1)!} h^\ell \frac{d^{\ell-1}}{dh^{\ell-1}} \int_0^\phi \frac{d\phi'}{h + \cos \phi'}. \quad (\text{B19})$$

This integral can be evaluated with a half-angle substitution

$$\int_0^\phi \frac{d\phi'}{h + \cos \phi'} = \frac{2}{\sqrt{h^2 - 1}} \arctan \left[\sqrt{\frac{h-1}{h+1}} \tan \left(\frac{\phi}{2} \right) \right]. \quad (\text{B20})$$

Substitute in Eq. (B17) and change to half angles $\phi \rightarrow \phi/2$, which gives

$$S_\ell = \frac{2^{\ell+4} a}{h} \frac{(-1)^{\ell-1}}{(\ell - 1)!} \frac{\partial^{\ell-1}}{\partial h^{\ell-1}} \int_0^{\pi/2} d\phi \frac{(s + \cos^2 \phi)^{\ell+1}}{\sqrt{h^2 - 1}} \arctan \left(\sqrt{\frac{h-1}{h+1}} \tan \phi \right). \quad (\text{B21})$$

Next, expand $(s + \cos^2 \phi)^{\ell+1}$ with the binomial identity

$$\int_0^{\pi/2} d\phi (s + \cos^2 \phi)^{\ell+1} \arctan \left(\sqrt{\frac{h-1}{h+1}} \tan \phi \right) = \sum_{n=0}^{\ell+1} \binom{\ell+1}{n} s^{\ell+1-n} \int_0^{\pi/2} d\phi \cos^{2n} \phi \arctan \left(\sqrt{\frac{h-1}{h+1}} \tan \phi \right) \quad (\text{B22})$$

where $\binom{\ell+1}{n} = (\ell+1)!/[n!(\ell+1-n)!]$. Switch variables to $x = \tan \phi$. The integral is then

$$\int_0^{\pi/2} d\phi \cos^{2n} \phi \arctan \left(\sqrt{\frac{h-1}{h+1}} \tan \phi \right) = \int_0^\infty \frac{dx}{(1+x^2)^{n+1}} \arctan \left(\sqrt{\frac{h-1}{h+1}} x \right). \quad (\text{B23})$$

The $n+1$ exponent in the denominator may be eliminated by expressing the integrand as the n^{th} derivative as follows:

$$= \lim_{\gamma \rightarrow 1} \frac{(-1)^n}{n!} \frac{\partial^n}{\partial \gamma^n} \int_0^\infty \frac{dx}{\gamma + x^2} \arctan \left(\sqrt{\frac{h-1}{h+1}} x \right) = \lim_{\gamma \rightarrow 1} \frac{(-1)^n}{n!} \frac{\partial^n}{\partial \gamma^n} \left[\frac{1}{\sqrt{\gamma}} \int_0^{\pi/2} d\theta \arctan \left(\sqrt{\frac{h-1}{h+1}} \tan \theta \right) \right] \quad (\text{B24})$$

where in the second step we changed integration variables to $x = \sqrt{\gamma} \tan \theta$. We can now define

$$F(h, \gamma) = \frac{1}{\sqrt{\gamma}} \int_0^{\pi/2} \arctan(q \tan \theta) d\theta = \frac{\chi_L(q) - \text{arctanh}(q) \ln(q)}{\sqrt{\gamma}} \quad \text{where } q \equiv q(h, \gamma) = \sqrt{\frac{h-1}{h+1}}. \quad (\text{B25})$$

where we have evaluated the integral using the Legendre- χ function

$$\chi_L(z) = \sum_{n=0}^{\infty} \frac{z^{2n+1}}{(2n+1)^2}. \quad (\text{B26})$$

Substituting back in Eq. (B22),

$$\int_0^{\pi/2} d\phi (s + \cos^2 \phi)^{\ell+1} \arctan \left(\sqrt{\frac{h-1}{h+1}} \tan \phi \right) = \lim_{\gamma \rightarrow 1} \sum_{n=0}^{\ell+1} \binom{\ell+1}{n} \frac{(-1)^n}{n!} s^{\ell+1-n} \frac{\partial^n}{\partial \gamma^n} F(h, \gamma). \quad (\text{B27})$$

The sum may be simplified using the following result, valid for any function F :

$$\sum_{n=0}^{\ell+1} \binom{\ell+1}{n} \frac{(-1)^n}{n!} s^{\ell+1-n} \frac{\partial^n}{\partial \gamma^n} F(h, \gamma) = \lim_{z \rightarrow 0} \frac{(-1)^{\ell+1}}{(\ell+1)!} \frac{\partial^{\ell+1}}{\partial z^{\ell+1}} \left[\frac{1}{1+sz} F \left(h, \gamma + \frac{z}{1+sz} \right) \right]. \quad (\text{B28})$$

Now we substitute back into Eq. (B21) and take the limit $\gamma \rightarrow 1$. The result may be simplified using the substitution $z = 2x$ and replacing h with $h + y$ where $y \rightarrow 0$, and then using $2s = h - 1$. We get

$$S_\ell = \lim_{\substack{x \rightarrow 0 \\ y \rightarrow 0}} \frac{2ae}{(\ell-1)!(\ell+1)!} \frac{\partial^{\ell+1}}{\partial x^{\ell+1}} \frac{\partial^{\ell-1}}{\partial y^{\ell-1}} G(h, x, y) \quad (\text{B29})$$

where $G(h, x, y)$ is

$$G(h, x, y) = \frac{4}{[(h-1)x+1](y+h+1)} \left[\frac{\chi_L(Q)}{Q} - \frac{\operatorname{arctanh}(Q)}{Q} \ln(Q) \right] \quad \text{where} \quad Q \equiv \sqrt{\left(\frac{(h+1)x+1}{(h-1)x+1} \right) \left(\frac{y+h-1}{y+h+1} \right)}. \quad (\text{B30})$$

$G(h, x, y)$ is a bivariate generating function of S_ℓ . This expression may be further manipulated to arrive at a more compact and symmetric form, using the substitutions $x \rightarrow (h_{\text{in}} - h)/(h^2 - 1)$, $y \rightarrow h_{\text{out}} - h$:

$$S_\ell = \lim_{\substack{h_{\text{in}} \rightarrow h \\ h_{\text{out}} \rightarrow h}} \frac{8a}{h} \frac{(h^2 - 1)^{\ell + \frac{3}{2}}}{(\ell - 1)!(\ell + 1)!} \frac{\partial^{\ell+1}}{\partial h_{\text{in}}^{\ell+1}} \frac{\partial^{\ell-1}}{\partial h_{\text{out}}^{\ell-1}} \frac{\chi_L(Q) - \operatorname{arctanh}(Q) \ln Q}{\sqrt{(h_{\text{in}}^2 - 1)(h_{\text{out}}^2 - 1)}} \quad \text{where} \quad Q \equiv \sqrt{\frac{(h+1)(h_{\text{in}} - 1)(h_{\text{out}} - 1)}{(h-1)(h_{\text{in}} + 1)(h_{\text{out}} + 1)}}. \quad (\text{B31})$$

Using

$$\frac{d\chi_L(q)}{dq} = \frac{\operatorname{arctanh} q}{q}, \quad \text{and} \quad \frac{d(\operatorname{arctanh} q)}{dq} = \frac{1}{2q} \left(\frac{1}{1-q} - \frac{1}{1+q} \right), \quad (\text{B32})$$

the result for $\ell \geq 3$ is

$$S_\ell = 4ae \left\{ 4A_\ell D_\ell \left[\chi_{\text{out}} \left(\sqrt{\frac{1-e}{1+e}} \right) + \frac{1}{2} \operatorname{arcsech}(e) \operatorname{arctanh}(e) \right] - \left[\left(\frac{1}{\ell} + \frac{1}{\ell+1} \right) \frac{1}{e} + B_\ell D_\ell \right] \operatorname{arctanh}(e) + C_\ell D_\ell + E_\ell \right\} \quad (\text{B33})$$

where A_ℓ , B_ℓ , C_ℓ , D_ℓ , and E_ℓ are

$$A_\ell = (-1)^{\ell+1} \sum_{i=0}^{\ell-1} P_{2i} P_{2\ell-2-2i} \left(\frac{1-e}{1+e} \right)^{i+\frac{1}{2}}, \quad (\text{B34})$$

$$B_\ell = (-1)^\ell \sum_{i=0}^{\ell-2} \sum_{n=0}^i \sum_{m=i}^{\ell-2} \frac{2 P_{2n} P_{2i-2n} P_{2m-2i} P_{2\ell-4-2m}}{m-n+1} \left(\frac{1-e}{1+e} \right)^{i+1}, \quad (\text{B35})$$

$$C_\ell = \sum_{i=0}^{\ell-3} \sum_{j=i}^{\ell-3} \sum_{n=0}^i \sum_{m=j}^{\ell-3} \frac{(-1)^{\ell+i-j} P_{2n} P_{2i-2n} P_{2m-2j} P_{2\ell-6-2m}}{(1+j-i)(\ell-1-m+n+j-i)} \left(\frac{1-e}{1+e} \right)^{i+1} \\ - \sum_{i=0}^{\ell-3} \sum_{j=0}^i \sum_{n=0}^j \sum_{m=i}^{\ell-3} \frac{(-1)^{\ell+j-i} P_{2n} P_{2j-2n} P_{2m-2i} P_{2\ell-6-2m}}{(1+i-j)(\ell-1-m+n+i-j)} \left(\frac{1-e}{1+e} \right)^{i+2}, \quad (\text{B36})$$

$$D_\ell = \sum_{n=0}^{\ell+1} \binom{\ell+1}{n} (-1)^n P_{2n}(0) \left(\frac{2e}{1-e} \right)^{n-1} \quad (\text{B37})$$

$$E_\ell = \sum_{i=0}^{\ell-2} \sum_{j=0}^i \sum_{n=i+1}^{\ell+1} \sum_{m=i+1}^n \binom{i}{j} \binom{\ell+1}{n} \frac{(-1)^{n+j} P_{2n-2m} P_{2m-2-2i}}{(\ell-1-j)m} \left[1 - \left(\frac{1-e}{1+e} \right)^{\ell-1-j} \right] \left(\frac{2e}{1-e} \right)^{n-i-2} \\ - \sum_{j=1}^{\ell-1} \binom{\ell-1}{j} \frac{(-1)^j}{j} \left[1 - \left(\frac{1-e}{1+e} \right)^j \right] \left[\frac{1}{2} \left(\frac{1}{\ell} + \frac{1}{\ell+1} \right) + \left(\frac{\ell+1}{\ell} - \frac{\ell}{(\ell+1)(j+1)} \right) \frac{1-e}{2e} \right] - \frac{1}{\ell+1} \quad (\text{B38})$$

where $P_{2n} \equiv P_{2n}(0)$ (see Eq. 6). However Eq. (B33) is numerically ill-behaved for $e > 0.5$ and $\ell \geq 35$, since in this case $D_\ell > 10^{15}$ and $E_\ell < -10^{14}$ in a way that the transcendental functions $A_\ell D_\ell [\chi_L(q) + \frac{1}{2} \operatorname{arcsech}(e) \operatorname{arctanh}(e)]$ cancel out the algebraic terms $C_\ell D_\ell + E_\ell$ to at least 14 significant digits.

Numerically we find that $S_\ell \propto \ell^{-1} \ln \ell$ as $\ell \rightarrow \infty$.

B3 Overlapping or embedded orbits

Finally we consider the most general case, in which the orbits overlap in radius. The derivation is similar to that of the previous subsection.

We start by changing the integration variables in Eq. (B11), $(r, r') \rightarrow (\phi_{\text{in}}, \phi_{\text{out}})$ such that $r_{\text{in}} = a_{\text{in}}(1 + e_{\text{in}} \cos \phi_{\text{in}})$ with a similar definition for ϕ_{out} and $a_{\text{in}} \leq a_{\text{out}}$:

$$S_\ell = \int_0^\pi d\phi_{\text{in}} \int_0^\pi d\phi_{\text{out}} \frac{\min(a_{\text{in}}(1 + e_{\text{in}} \cos \phi_{\text{in}}), a_{\text{out}}(1 + e_{\text{out}} \cos \phi_{\text{out}}))^{\ell+1}}{\max(a_{\text{in}}(1 + e_{\text{in}} \cos \phi_{\text{in}}), a_{\text{out}}(1 + e_{\text{out}} \cos \phi_{\text{out}}))^\ell}. \quad (\text{B39})$$

We may take a factor $(a_{\text{in}}/a_{\text{out}})^\ell$ outside of the integral as defined in Eq. (B12) to arrive at Eqs. (5)–(7) in the main text.

The integration domain can be separated into two parts depending on which $a_i(1 + e_i \cos \phi_i)$ is larger:

$$S_\ell = S_\ell^- + S_\ell^+, \quad \text{where} \quad S_\ell^+ = \frac{a_{\text{in}}^{\ell+1}}{a_{\text{out}}^\ell} \int \int_{\substack{0 \leq \phi_{\text{in}}, \phi_{\text{out}} < \pi \\ a_{\text{in}}(1 + e_{\text{in}} \cos \phi_{\text{in}}) < a_{\text{out}}(1 + e_{\text{out}} \cos \phi_{\text{out}})}} d\phi_{\text{in}} d\phi_{\text{out}} \frac{(1 + e_{\text{in}} \cos \phi_{\text{in}})^{\ell+1}}{(1 + e_{\text{out}} \cos \phi_{\text{out}})^\ell}, \quad (\text{B40})$$

and S_ℓ^- is obtained similarly, by switching the stellar indices “in” \leftrightarrow “out” in S_ℓ^+ . The quantity S_ℓ^+ gives the contribution to the interaction energy from the regions where the orbit with the larger semimajor axis has larger radius than the orbit with the smaller semimajor axis, and vice versa for S_ℓ^- . For non-overlapping orbits S_ℓ^- vanishes.

We follow the analysis of the previous subsection to convert S_ℓ^+ to a generating function. To this end we introduce a similar notation

$$h_{\text{out}} \equiv \frac{1}{e_{\text{out}}}, \quad s_{\text{in}} \equiv \frac{1 - e_{\text{in}}}{2e_{\text{in}}}. \quad (\text{B41})$$

First we simplify the denominator by differentiating with respect to h_{out} ,

$$S_\ell^+ = \frac{a_{\text{in}}^{\ell+1} (-1)^{\ell-1}}{a_{\text{out}}^\ell (\ell-1)!} h_{\text{out}}^\ell \frac{\partial^{\ell-1}}{\partial h_{\text{out}}^{\ell-1}} \int_0^\pi d\phi_{\text{in}} (1 + e_{\text{in}} \cos \phi_{\text{in}})^{\ell+1} \int_{\substack{0 \leq \phi_{\text{out}} < \pi \\ a_{\text{in}}(1+e_{\text{in}} \cos \phi_{\text{in}}) < a_{\text{out}}(1+e_{\text{out}} \cos \phi_{\text{out}})}} \frac{d\phi_{\text{out}}}{h_{\text{out}} + \cos \phi_{\text{out}}}. \quad (\text{B42})$$

Now make the substitutions $y = \sqrt{(h_{\text{out}} - 1)/(h_{\text{out}} + 1)} \tan(\phi_{\text{out}}/2)$ and $\phi_{\text{in}} \rightarrow \phi_{\text{in}}/2$

$$S_\ell^+ = \frac{(2e_{\text{in}}a_{\text{in}})^{\ell+1} (-1)^{\ell-1}}{a_{\text{out}}^\ell (\ell-1)!} h_{\text{out}}^\ell \frac{\partial^{\ell-1}}{\partial h_{\text{out}}^{\ell-1}} \int_0^{\pi/2} d\phi_{\text{in}} \frac{(s_{\text{in}} + \cos^2 \phi_{\text{in}})^{\ell+1}}{\sqrt{h_{\text{out}}^2 - 1}} \int_{\substack{0 \leq y < \infty \\ D(y)}} \frac{dy}{1 + y^2}. \quad (\text{B43})$$

where the domain $D(y)$ is defined such that

$$[(r_{p,\text{in}} - r_{a,\text{out}}) \tan^2 \phi_{\text{in}} + (r_{a,\text{in}} - r_{a,\text{out}})] \frac{h_{\text{out}} - 1}{h_{\text{out}} + 1} \leq [(r_{p,\text{out}} - r_{p,\text{in}}) \tan^2 \phi_{\text{in}} + (r_{p,\text{out}} - r_{a,\text{in}})] y^2; \quad (\text{B44})$$

the “in” and “out” indices in r_p and r_a continue to refer to the orbits with the smaller and larger semimajor axes. To carry out the integral we must express the integration bound explicitly for y . We introduce angles where the sign of the left-hand and right-hand sides changes in Eq. (B44):

$$\phi_l = \arctan \sqrt{\frac{r_{a,\text{in}} - r_{a,\text{out}}}{r_{a,\text{out}} - r_{p,\text{in}}}} \quad \text{if } r_{p,\text{in}} < r_{a,\text{out}} \leq r_{a,\text{in}}, \quad \phi_l = 0 \quad \text{if } r_{a,\text{in}} \leq r_{a,\text{out}}, \quad (\text{B45})$$

$$\phi_r = \arctan \sqrt{\frac{r_{a,\text{in}} - r_{p,\text{out}}}{r_{p,\text{out}} - r_{p,\text{in}}}} \quad \text{if } r_{p,\text{in}} < r_{p,\text{out}} \leq r_{a,\text{in}}, \quad \phi_r = 0 \quad \text{if } r_{a,\text{in}} \leq r_{p,\text{out}}, \quad \phi_r = \frac{\pi}{2} \quad \text{if } r_{p,\text{out}} \leq r_{p,\text{in}}. \quad (\text{B46})$$

Note that ϕ_l and ϕ_r are continuous across $r_{p,\text{out}} = r_{a,\text{in}}$ and $r_{a,\text{in}} = r_{a,\text{out}}$. It is easy to show that $\phi_l \leq \phi_r$. We also define the function

$$\Theta(t) = \sqrt{\frac{(r_{p,\text{in}} - r_{a,\text{out}})t^2 + (r_{a,\text{in}} - r_{a,\text{out}})}{(r_{p,\text{out}} - r_{p,\text{in}})t^2 + (r_{p,\text{out}} - r_{a,\text{in}})}}. \quad (\text{B47})$$

With these definitions, the integral over $D(y)$ can be carried separately over the individual regions

$$S_\ell^+ = 4 \frac{(2a_{\text{in}}e_{\text{in}})^{\ell+1} (-1)^{\ell-1}}{(a_{\text{out}}e_{\text{out}})^\ell (\ell-1)!} \frac{\partial^{\ell-1}}{\partial h_{\text{out}}^{\ell-1}} \left\{ \int_{\phi_l}^{\phi_r} d\phi_{\text{in}} \frac{(s_{\text{in}} + \cos^2 \phi_{\text{in}})^{\ell+1}}{\sqrt{h_{\text{out}}^2 - 1}} \arctan \left[\sqrt{\frac{h_{\text{out}} - 1}{h_{\text{out}} + 1}} \Theta(\tan \phi_{\text{in}}) \right] \right. \\ \left. + \int_{\phi_r}^{\pi/2} d\phi_{\text{in}} \frac{(s_{\text{in}} + \cos^2 \phi_{\text{in}})^{\ell+1}}{\sqrt{h_{\text{out}}^2 - 1}} \frac{\pi}{2} \right\} \quad (\text{B48})$$

We may turn this into a generating function by manipulations analogous to Eqs. (B21)–(B29). We find that

$$S_\ell^+ = \lim_{\substack{x \rightarrow 0 \\ y \rightarrow 0}} \frac{1}{(\ell-1)!(\ell+1)!} \frac{\partial^{\ell+1}}{\partial x^{\ell+1}} \frac{\partial^{\ell-1}}{\partial y^{\ell-1}} G_+(x, y) \quad (\text{B49})$$

where $G_+(x, y) \equiv G_+(x, y; r_{p,\text{in}}, r_{a,\text{in}}, r_{p,\text{out}}, r_{a,\text{out}})$ is a bivariate generating function of S_ℓ^+ given by

$$G_+(x, y) = \frac{4}{\sqrt{(y + r_{a,\text{out}})(y + r_{p,\text{out}})} \sqrt{(1 + r_{p,\text{in}}x)(1 + r_{a,\text{in}}x)}} \left\{ \int_{\theta_l(x)}^{\theta_r(x)} \arctan \{Q_2(y) \Theta[Q_1(x) \tan \theta]\} d\theta + \frac{\pi}{2} \left[\frac{\pi}{2} - \theta_r(x) \right] \right\} \quad (\text{B50})$$

where

$$Q_1(x) = \sqrt{\frac{1 + r_{a,\text{in}}x}{1 + r_{p,\text{in}}x}}, \quad Q_2(y) = \sqrt{\frac{y + r_{p,\text{out}}}{y + r_{a,\text{out}}}}, \quad (\text{B51})$$

$$\theta_l(x) = \begin{cases} 0 & \text{if } r_{a,\text{in}} \leq r_{a,\text{out}}, \\ \arctan \left[\sqrt{\frac{r_{a,\text{in}} - r_{a,\text{out}}}{r_{a,\text{out}} - r_{p,\text{in}}}} / Q_1(x) \right] & \text{if } r_{p,\text{in}} < r_{a,\text{out}} \leq r_{a,\text{in}}, \end{cases} \quad (\text{B52})$$

$$\theta_r(x) = \begin{cases} 0 & \text{if } r_{a,\text{in}} \leq r_{p,\text{out}}, \\ \arctan \left[\sqrt{\frac{r_{a,\text{in}} - r_{p,\text{out}}}{r_{p,\text{out}} - r_{p,\text{in}}}} / Q_1(x) \right] & \text{if } r_{p,\text{in}} < r_{p,\text{out}} \leq r_{a,\text{in}}, \\ \frac{1}{2}\pi & \text{if } r_{p,\text{out}} \leq r_{p,\text{in}}. \end{cases} \quad (\text{B53})$$

The analogous generating function $G_-(x, y)$ for S_ℓ^- is obtained by switching the indices “in” \leftrightarrow “out” in $G_+(x, y)$.

Note that the generating function for S_ℓ^+ in Eq. (B50) is not unique. In particular, $c^{\ell+1}d^{\ell-1}G_+(cx, dy)$ is also a generating function of S_ℓ^+ for arbitrary constants c and d .²¹ We use this property to arrive at a more compact and symmetric form analogous to Eq. (B31)

$$S_\ell^+ = \frac{a_{\text{in}}^{\ell+1}}{a_{\text{out}}^\ell} (1 - e_{\text{in}}^2)^{\ell+\frac{3}{2}} \frac{h_{\text{in}}^{\ell+2} h_{\text{out}}^\ell}{(\ell+1)! (\ell-1)!} \frac{\partial^{\ell+1}}{\partial h_{\text{in}}^{\ell+1}} \frac{\partial^{\ell-1}}{\partial h_{\text{out}}^{\ell-1}} \frac{4}{\sqrt{(h_{\text{in}}^2-1)(h_{\text{out}}^2-1)}} \left\{ \int_{\theta'_l(h_{\text{in}})}^{\theta'_r(h_{\text{in}})} \arctan \left\{ Q(h_{\text{out}}) \Theta \left[\frac{Q(h_{\text{in}})}{Q(1/e_{\text{in}})} \tan \theta' \right] \right\} d\theta' + \frac{\pi}{2} \left(\frac{\pi}{2} - \theta'_r(h_{\text{in}}) \right) \right\} \quad (\text{B55})$$

where $h_{\text{in}} = 1/e_{\text{in}}$ and we have introduced

$$Q(x) = \sqrt{\frac{x-1}{x+1}}, \quad (\text{B56})$$

and

$$\theta'_l(h_{\text{in}}) = \begin{cases} 0 & \text{if } r_{a,\text{in}} \leq r_{a,\text{out}}, \\ \arctan \left[\sqrt{\frac{r_{a,\text{in}} - r_{a,\text{out}}}{r_{a,\text{out}} - r_{p,\text{in}}} \frac{Q(1/e_{\text{in}})}{Q(h_{\text{in}})}} \right] & \text{if } r_{p,\text{in}} \leq r_{a,\text{out}} \leq r_{a,\text{in}}, \end{cases} \quad (\text{B57})$$

$$\theta'_r(h_{\text{in}}) = \begin{cases} 0 & \text{if } r_{a,\text{in}} \leq r_{p,\text{out}}, \\ \arctan \left[\sqrt{\frac{r_{a,\text{in}} - r_{p,\text{out}}}{r_{p,\text{out}} - r_{p,\text{in}}} \frac{Q(1/e_{\text{in}})}{Q(h_{\text{in}})}} \right] & \text{if } r_{p,\text{in}} \leq r_{p,\text{out}} \leq r_{a,\text{in}}, \\ \frac{1}{2}\pi & \text{if } r_{p,\text{out}} \leq r_{p,\text{in}}. \end{cases} \quad (\text{B58})$$

Note the distinction between e_{in}^{-1} and h_{in} : while the two are equal, $\partial/\partial h_{\text{in}}$ does not act on e_{in}^{-1} . Here $Q(1/e_{\text{in}}) = \sqrt{r_{p,\text{in}}/r_{a,\text{in}}}$.

Equations (B48), (B49)–(B50), and (B55) are valid for all eccentricities $0 < e_i < 1$ ($i = \text{in}$ or out) in both the overlapping/embedded and non-overlapping cases. We may recover the special cases derived for non-overlapping and identical orbits as follows. For identical orbits $a_{\text{in}} = a_{\text{out}}$, $e_{\text{in}} = e_{\text{out}}$, so $h_{\text{in}} = h_{\text{out}} = 1/e$, $\theta'_l = 0$, $\theta'_r = \frac{1}{2}\pi$, and $\Theta(\cdot)$ is the identity function (see Eq. B47), and we recover Eqs. (B25) and (B31) given that $S_\ell = S_\ell^+ + S_\ell^- = 2S_\ell^+$ in this case. For non-overlapping orbits $\theta'_l = \theta'_r = 0$ and so the integration domain in Eq. (B55) is empty. Then the quantity in braces in Eq. (B55) is just $\pi^2/4$ and S_ℓ^- vanishes. The evaluation of S_ℓ using Eq. (B55) reduces to finding the derivatives of $1/\sqrt{h^2-1}$. These generate the Legendre polynomials,

$$\frac{x^{\ell+1}}{\ell!} \frac{\partial^\ell}{\partial x^\ell} \frac{1}{\sqrt{x^2-1}} = \frac{(-1)^\ell}{(1-x^{-2})^{(\ell+1)/2}} P_\ell \left(\frac{1}{\sqrt{1-x^{-2}}} \right) \quad (\text{B59})$$

and we recover Eq. (B16) for non-overlapping orbits.

B4 Classification of orbits

The generating function (B49)–(B50) is useful to understand the behavior of the interaction energy shown in Figure 1. This function generates the functions S_ℓ^+ and S_ℓ^- that determine the resonant relaxation Hamiltonian H_{RR} ; these are piecewise smooth functions of the periaapsis and apoapsis distances $\{r_{p_i}, r_{a_i}, r_{p_j}, r_{a_j}\}$ and have discontinuous derivatives for special values of $\{r_{p_i}, r_{a_i}, r_{p_j}, r_{a_j}\}$. We may classify the orbits accordingly as follows. For simplicity we assume that the labels are chosen so that orbit i is the “smaller” orbit; here “smaller” means the smaller periaapsis, $r_{p_i} \leq r_{p_j}$, or if the periaapsides are equal the smaller apoapsis.

There are 14 topologically different radial configurations where the interaction energy behaves differently, with distinct large- ℓ asymptotics. These are defined by the relative radial locations of the singularities in the radial density function $\sigma(r)$ in Eq. (3), i.e., r_{p_i} , r_{a_i} , r_{p_j} , and r_{a_j} . Three of the 14 configurations have a nonzero measure, i.e.

- (i) $r_{p_i} < r_{a_i} < r_{p_j} < r_{a_j}$: non-overlapping orbits, $r_i < r_j$ everywhere, with $S_\ell^- = 0$ and $S_\ell = S_\ell^+$,
- (ii) $r_{p_i} < r_{p_j} < r_{a_i} < r_{a_j}$: overlapping orbits,
- (iii) $r_{p_i} < r_{p_j} < r_{a_j} < r_{a_i}$: embedded orbits with $r_j \subset r_i$,

There are 11 pathological configurations of zero measure when at least two of $\{r_{p_i}, r_{a_i}, r_{p_j}, r_{a_j}\}$ coincide—six configurations where exactly two coincide, two configurations where two distinct pairs coincide (i.e., $r_{p_i} = r_{p_j} < r_{a_i} = r_{a_j}$, $r_{p_i} = r_{a_i} < r_{p_j} = r_{a_j}$), two configurations where three coincide, and one configuration where all four coincide. Six of the 11 pathological

²¹ Another transformation that preserves S_ℓ is the one introduced in Eq. (B14), which reverses the roles of the orbits, i.e.

$$G(x, y; r_{p,\text{in}}, r_{a,\text{in}}, r_{p,\text{out}}, r_{a,\text{out}}) \leftrightarrow \sqrt{\frac{r_{p,\text{in}} r_{a,\text{in}}}{r_{p,\text{out}} r_{a,\text{out}}}} G(x, y; r_{a,\text{out}}^{-1}, r_{p,\text{out}}^{-1}, r_{a,\text{in}}^{-1}, r_{p,\text{in}}^{-1}) \quad (\text{B54})$$

is also a generating function of S_ℓ that satisfies Eq. (B49). The roles of h_{in} and h_{out} are reversed in the corresponding Eq. (B31) for the transformed orbits.

configurations involve circular orbits. In particular, 4 have one circular and one eccentric orbit, 1 has two distinct circular orbits, and 1 has two circular orbits with the same radius.

The configurations (i)–(iii) with non-zero measure are the most important. The behavior of S_ℓ is different in these three regions as shown in Figure 1 in the main text. As a function of the semimajor axis ratio $\alpha < 1$, S_ℓ has a plateau for overlapping/embedded orbits and local maxima at the edges of the overlapping/embedded regions where two of the radial turning points coincide. Once the orbits are non-overlapping, S_ℓ decays quickly as α decreases, i.e., $S_\ell \propto \alpha^\ell$. The figure shows that S_ℓ varies continuously as a function of α , but at the transition between overlapping and non-overlapping orbits its first derivatives with respect to α are (approximately) discontinuous, especially for large ℓ .

This classification scheme does not distinguish cases where the semimajor axes coincide ($\alpha = 1$); however the interaction energy is typically a smooth function of a_i/a_j across $a_i = a_j$ for eccentric orbits.

B5 Convergence

How many terms of the infinite sum must one account for to accurately calculate the interaction Hamiltonian? We use the following asymptotic properties of Legendre polynomials:

$$P_\ell(\cos \theta) = \left(\frac{\theta}{\sin \theta} \right)^{1/2} J_0[(\ell + \frac{1}{2})\theta][1 + \mathcal{O}(\ell^{-1})], \quad 0 \leq \theta \leq \frac{1}{2}\pi \quad (\text{B60})$$

$$P_\ell\left(\frac{1}{\sqrt{1-e^2}}\right) = \left(\frac{\xi}{\sinh \xi}\right)^{1/2} I_0[(\ell + \frac{1}{2})\xi][1 + \mathcal{O}(\ell^{-1})], \quad \xi \equiv \tanh^{-1} e. \quad (\text{B61})$$

Here J_0 and Y_0 are Bessel functions and I_0 is a modified Bessel functions. In evaluating these expressions the following properties of Bessel functions are useful:

$$J_0(x) = \left(\frac{2}{\pi x}\right)^{1/2} \left[\cos\left(x - \frac{1}{4}\pi\right) + \mathcal{O}(x^{-1})\right] \quad (\text{B62})$$

$$I_0(x) = \frac{e^x}{\sqrt{2\pi x}} [1 + \mathcal{O}(x^{-1})]. \quad (\text{B63})$$

From these results, or from Eq. (6) and Stirling's formula, it is straightforward to show that $P_{2\ell}(0)^2 \rightarrow 1/(\pi\ell)$ for large ℓ ; Substituting in Eqs. (8) and (10) for non-overlapping or marginally overlapping orbits, we find that the coupling coefficients in the Hamiltonian asymptotically satisfy

$$\mathcal{J}_\ell^{\text{asympt}} = \frac{Gm_{\text{in}}m_{\text{out}}}{\pi^2\ell^2} \frac{r_{a,\text{in}}^\ell}{r_{p,\text{out}}^{\ell+1}} \frac{[(1+e_{\text{in}})(1-e_{\text{out}})]^{3/2}}{(e_{\text{in}}e_{\text{out}})^{1/2}} [1 + \mathcal{O}(\ell^{-1})] \quad \text{if } \ell \gtrsim \max\left(\frac{5}{e_{\text{in}}}, \frac{5}{e_{\text{out}}}\right), \quad r_{p,\text{out}} \geq r_{a,\text{in}}, \quad \text{and } \ell \text{ even.} \quad (\text{B64})$$

If one or both orbits are circular, the asymptotic decay of \mathcal{J}_ℓ is slower by factors of $\ell^{1/2}$ and ℓ , respectively. Note that $\mathcal{J}_\ell \propto \ell^{-2}$ for marginally overlapping orbits where $r_{p,\text{out}} = r_{a,\text{in}}$.

For overlapping or embedded orbits, we may derive the asymptotic form of the coupling coefficients using the stationary phase approximation. For large ℓ the double integral in Eq. (B40) is dominated by the region where $a_{\text{in}}(1+e_{\text{in}}\cos\phi_{\text{in}}) \approx a_{\text{out}}(1+e_{\text{out}}\cos\phi_{\text{out}})$. We define $\phi_* \equiv \phi_*(\phi_{\text{out}})$ to satisfy $a_{\text{in}}(1+e_{\text{in}}\cos\phi_*) = a_{\text{out}}(1+e_{\text{out}}\cos\phi_{\text{out}})$, and replace the integration variable ϕ_{in} with $\phi_* + \Delta$. After substituting in Eq. (B40) and expanding $\cos(\phi_* + \Delta)$ to first order in Δ we get

$$S_\ell^+ = a_{\text{out}} \int_{\phi_l}^{\phi_r} d\phi_{\text{out}} \int_0^{\Delta_{\text{max}}} d\Delta (1 + e_{\text{out}} \cos \phi_{\text{out}}) \left[1 - \frac{a_{\text{in}} e_{\text{in}} \sin \phi_*(\phi_{\text{out}})}{a_{\text{out}} (1 + e_{\text{out}} \cos \phi_{\text{out}})} \Delta \right]^{\ell+1}, \quad (\text{B65})$$

where

$$\phi_l = \arccos\left(\frac{r_{a,\text{in}} - a_{\text{out}}}{a_{\text{out}} e_{\text{out}}}\right) \quad \text{and} \quad \phi_r = \arccos\left(\frac{r_{p,\text{in}} - a_{\text{out}}}{a_{\text{out}} e_{\text{out}}}\right) \quad (\text{B66})$$

if both are real, and $\phi_l = 0$ and/or $\phi_r = \pi$ otherwise. For large ℓ , the integrand decays exponentially as a function of Δ , so we can extend the integration domain to $0 \leq \Delta < \infty$. Approximate the bracket in Eq. (B65) using $\lim_{n \rightarrow \infty} (1 + x/n)^n = e^x$, carry out the Δ integral, and change the integration variable to simplify the result:

$$S_\ell^+ \approx \frac{1}{\ell} \frac{a_{\text{out}}^2}{a_{\text{in}}} \int_{\phi_l}^{\phi_r} d\phi_{\text{out}} \frac{(1 + e_{\text{out}} \cos \phi_{\text{out}})^2}{e_{\text{in}} \sin \phi_*(\phi_{\text{out}})} = \frac{1}{\ell} \int_{\max(r_{p,\text{in}}, r_{p,\text{out}})}^{\min(r_{a,\text{in}}, r_{a,\text{out}})} \frac{r^2 dr}{\sqrt{(r - r_{p,\text{in}})(r - r_{p,\text{out}})(r_{a,\text{in}} - r)(r_{a,\text{out}} - r)}}. \quad (\text{B67})$$

Note that the integral in Eq. (B67) is independent of ℓ . It can be evaluated in a closed form using a Möbius transform²²

²² <http://math.stackexchange.com/questions/669301/closed-form-integral-int-bc-fracx2-sqrtx-ax-bc-xd-x-dx>

(Byrd & Friedman 1971):

$$I^{(2)}(a, b, c, d) = \int_b^c \frac{r^2 dr}{\sqrt{(r-a)(r-b)(c-r)(d-r)}} = (c-b) \sqrt{\frac{k^2 - \lambda^2}{1 - \lambda^2}} \left\{ \begin{array}{l} K(k) \left(\frac{c+b}{c-b} \right)^2 \\ + \frac{2}{\lambda} [K(k) - (1 - \lambda^2)\Pi(\lambda^2, k)] \left(\frac{c+b}{c-b} \right) \\ + K(k) + \frac{1 - \lambda^2}{\lambda^2 - k^2} [E(k) - (1 - k^2)\Pi(\lambda^2, k)] \end{array} \right\} \quad (\text{B68})$$

for $a < b < c < d$, where

$$\lambda = \frac{\Lambda}{1 + \sqrt{1 - \Lambda^2}}, \quad \Lambda = \frac{\tilde{a} + \tilde{d}}{1 + \tilde{a}\tilde{d}}, \quad \tilde{a} = \frac{2a - (b+c)}{c-b}, \quad \tilde{d} = \frac{2d - (b+c)}{c-b}, \quad k = \frac{1 - \lambda\tilde{d}}{\tilde{d} - \lambda}, \quad (\text{B69})$$

and $K(k)$, $E(k)$, and $\Pi(k)$ are complete elliptic integrals²³. Similarly, it may be shown that S_ℓ^- and S_ℓ^+ are asymptotically equal for overlapping or embedded orbits with distinct periapsides and apoapsides. After substituting in Eqs. (B7) and (9)–(10) we arrive at the asymptotic form for overlapping or embedded orbits

$$\mathcal{J}_\ell^{\text{asympt}} = \frac{4}{\pi^3 \ell^2} \frac{Gm_{\text{in}}m_{\text{out}}}{a_{\text{in}}a_{\text{out}}} I^{(2)}(r_{p<}, r_{p>}, r_{a<}, r_{a>}) \quad \text{if } r_{p>} < r_{a<}, r_{p<} \neq r_{p>}, r_{a<} \neq r_{a>}, \ell \gtrsim \frac{2r_{p>}}{r_{a<} - r_{p>}} \text{ and } \ell \in \text{even}, \quad (\text{B71})$$

where $r_{p<} = \min(r_{p,\text{in}}, r_{p,\text{out}})$, $r_{p>} = \max(r_{p,\text{in}}, r_{p,\text{out}})$, and similarly for $r_{a<}$ and $r_{a>}$.

Using a combination of analytic arguments and numerical experiments, we find that the terms in the sum over ℓ comprising the Hamiltonian (Eq. 9) decrease asymptotically for the different configurations defined in Appendix B4 as follows²⁴.

- $\ell^{-2.5} \alpha^\ell \cos(\ell I) / \sqrt{\sin I}$ for non-coplanar, non-overlapping or marginally overlapping, eccentric orbits, where $\alpha \equiv r_{a,\text{in}}/r_{p,\text{out}} < 1$;
- $\ell^{-2} \alpha^\ell$ for coplanar, non-overlapping or marginally overlapping, eccentric orbits;
- $\ell^{-2} \alpha^\ell \cos(\ell I) / \sqrt{\sin I}$ for non-coplanar, non-overlapping orbits, one circular and one eccentric;
- $\ell^{-1.5} \alpha^\ell$ for coplanar, non-overlapping orbits, one circular and one eccentric;
- $\ell^{-1.5} \alpha^\ell \cos(\ell I) / \sqrt{\sin I}$ for non-coplanar circular orbits with different radii;
- $\ell^{-1} \alpha^\ell$ for coplanar circular orbits with different radii;
- $\ell^{-2.5} \cos(\ell I) / \sqrt{\sin I}$ for non-coplanar overlapping or embedded orbits;
- ℓ^{-2} for coplanar overlapping or embedded orbits;
- $\ell^{-2.5} \ln \ell / \sqrt{\sin I}$ for non-coplanar embedded orbits where the periapsides or the apoapsides coincide ($r_{p,\text{in}} = r_{p,\text{out}}$ or $r_{a,\text{in}} = r_{a,\text{out}}$);
- $\ell^{-2} \ln \ell$ for coplanar embedded orbits where the periapsides or the apoapsides coincide;
- $\ell^{-2} \cos(\ell I) / \sqrt{\sin I}$ for non-coplanar orbits, one circular and one eccentric, with the same peri- or apoapsides ($r_{a,\text{in}} = r_{p,\text{out}} = r_{a,\text{out}}$);
- $\ell^{-1.5}$ for coplanar orbits, one circular and one eccentric, with the same peri- or apoapsides ($r_{p,\text{in}} = r_{a,\text{in}} = r_{p,\text{out}}$ or $r_{a,\text{in}} = r_{p,\text{out}} = r_{a,\text{out}}$);
- $\ell^{-1.5} \cos(\ell I) / \sqrt{\sin I}$ for non-coplanar circular orbits with the same radii ($r_{p,\text{in}} = r_{a,\text{in}} = r_{p,\text{out}} = r_{a,\text{out}}$);
- ℓ^{-1} for coplanar circular orbits with the same radii ($r_{p,\text{in}} = r_{a,\text{in}} = r_{p,\text{out}} = r_{a,\text{out}}$).

The interaction energy sum in Eq. (B86) converges for all but the last of these cases, in which the interaction energy has a logarithmic singularity in $a_{\text{out}} - a_{\text{in}}$. Figure B1 shows examples of \mathcal{J}_ℓ for orbits with eccentricities 0.2 and 0.8. The asymptotic relations for non-overlapping or marginally overlapping orbits (Eq. B64) approximate \mathcal{J}_ℓ to within 50% already at $\ell = 2$.

The rate of convergence for an asymptotic scaling ℓ^{-k} is related to the Riemann ζ function of order k . The absolute error when neglecting $\ell \geq \ell_0$ is then typically proportional to

$$\sum_{\ell=\ell_0}^{\infty} \frac{1}{\ell^k} = \zeta(k, \ell_0). \quad (\text{B72})$$

For all overlapping or embedded orbits other than a set of measure zero, we have $k = 2$ for coplanar orbits and $k = \frac{5}{2}$ for non-coplanar orbits, so the relative error from neglecting $\ell_0 \geq 10$ is of order $\zeta(2, 10)/\zeta(2) = 0.064$ for coplanar orbits and

²³ We use the definitions

$$K(k) = \int_0^1 \frac{dz}{\sqrt{(1-z^2)(1-k^2z^2)}}, \quad E(k) = \int_0^1 \sqrt{\frac{1-k^2z^2}{1-z^2}} dz, \quad \text{and} \quad \Pi(\eta, k) = \int_0^1 \frac{dz}{(1-\eta z^2)\sqrt{(1-z^2)(1-k^2z^2)}}. \quad (\text{B70})$$

²⁴ In all of these equations $\cos \ell I$ is shifted by a phase of order $-\pi/4$ not shown for simplicity, see Eqs. (B60) and (B62).

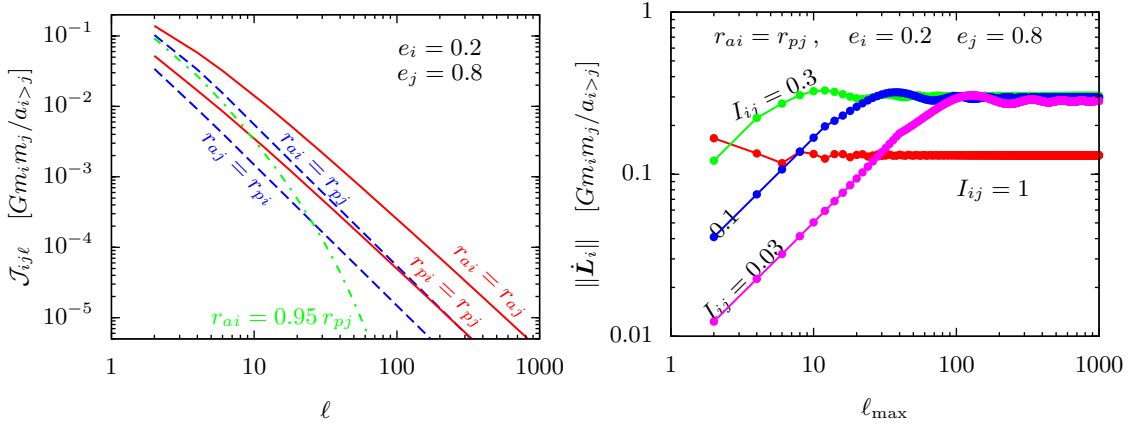


Figure B1. *Left:* Asymptotic behavior of the coupling coefficients of the Hamiltonian as a function of the (even) multipole order ℓ , for orbit pairs with $e_i = 0.2$ and $e_j = 0.8$. Red solid curves show marginally embedded orbits, $r_{pi} = r_{pj}$ and $r_{ai} = r_{aj}$ respectively, which scale asymptotically as $\ell^{-2} \ln \ell$. Blue dashed curves show marginally overlapping orbits, $r_{pi} = r_{aj}$ and $r_{pj} = r_{ai}$ respectively, which scale asymptotically as ℓ^{-2} . The green dash-dotted curve shows a non-overlapping orbit, $r_{aj} = 0.95 r_{pi}$, for which the coupling coefficient declines exponentially at high ℓ . The coupling coefficients are continuous functions of the orbital parameters, so the coefficients of all overlapping orbits with these eccentricities lie in between the red and blue curves shown, and all non-overlapping orbits lie below the blue curves. *Right:* The torque on star i due to star j as a function of ℓ_{\max} , for different inclinations as marked in radians. The orbits are marginally overlapping, $r_{ai} = r_{pj}$. As the inclination tends to zero, an accurate evaluation of the torque requires more and more ℓ multipoles.

$\zeta(\frac{5}{2}, 10)/\zeta(\frac{5}{2}) = 0.017$ for non-coplanar orbits. Thus, the error in calculating the Hamiltonian should be only of order a few percent if we account for at least the first four non-zero multipoles in the interaction. Similarly, multipoles up to and including $\ell = 12$ and 60 must be accounted for in order to reach 1% accuracy for the non-coplanar and coplanar cases, respectively, and $\ell = 60$ and 600 for 0.1% accuracy. The convergence rate is exponentially faster for non-overlapping orbits; for example, if $r_{a,\text{in}}/r_{p,\text{out}} \leq 0.3$ then by including all multipoles up to $\ell = 10$ we expect to achieve an accuracy of 10^{-7} – 10^{-8} .

The equations of motion converge more slowly. In Eq. (13) we found that

$$\dot{\mathbf{L}}_i = \boldsymbol{\Omega}_i \times \mathbf{L}_i, \quad \text{where} \quad \boldsymbol{\Omega}_i = - \sum_{j\ell} \frac{\tilde{J}_{ij\ell}}{L_i L_j} P'_\ell(\hat{\mathbf{L}}_i \cdot \hat{\mathbf{L}}_j) \mathbf{L}_j. \quad (\text{B73})$$

From Eqs. (B60) and (B62) we get

$$P'_\ell(\cos \theta) = \frac{\ell \theta^{1/2}}{\sin^{3/2} \theta} \{ J_1[(\ell - \frac{1}{2})\theta] + \mathcal{O}(\ell^{-1}) \} \quad (\text{B74})$$

$$= \sqrt{\frac{2\ell}{\pi \sin^3 \theta}} \{ \cos[(\ell + \frac{1}{2})\theta - \frac{3}{4}\pi] + \mathcal{O}(\ell^{-1}) \} \quad \text{if} \quad \ell \gtrsim \frac{2}{\theta}. \quad (\text{B75})$$

This shows that non-coplanar orbits precess around their total angular momentum vector, with an angular velocity that is convergent if $\tilde{J}_{ij\ell} < C_{ij} \ell^{-1.5}$ for large ℓ for some C_{ij} constant. This condition is generally met by all non-overlapping orbits and also by overlapping or embedded eccentric orbits. However, for nearly coplanar overlapping or embedded eccentric orbits, the sum over the multipoles converges more slowly. The right panel of Figure B1 shows the convergence of the precession rate by truncating the torque sum at different ℓ_{\max} for different inclinations, when the orbits have $e_i = 0.2$ and $e_j = 0.8$ and $r_{ai} = r_{pj}$. For overlapping or embedded orbits truncating the sum at some ℓ_{\max} leads to an accurate evaluation of the torque unless the orbits are nearly parallel or antiparallel, with mutual inclination $I < \frac{1}{2}\pi/\ell_{\max}$ or $I > \pi - \frac{1}{2}\pi/\ell_{\max}$. For non-overlapping orbits with $r_{a,\text{in}}/r_{p,\text{out}} < 0.3$, $\ell_{\max} = 10$ is sufficient for a tolerance of 10^{-6} at arbitrary inclinations.

B6 Extrapolating to $\ell \rightarrow \infty$

Neglecting the contribution of terms with $\ell > \ell_{\max}$ in the equations of motion is equivalent to an effective gravitational softening. Alternatively, the asymptotic relations we have derived may be used to extrapolate the contribution of terms in the equations of motion with $\ell \leq \ell_{\max}$ to $\ell \rightarrow \infty$. We start by rewriting the second of Eqs. (B73) as

$$\boldsymbol{\Omega}_i = \boldsymbol{\Omega}_i^{\text{asympt}} + (\boldsymbol{\Omega}_i - \boldsymbol{\Omega}_i^{\text{asympt}}) = \boldsymbol{\Omega}_i^{\text{asympt}} - \sum_{j\ell} \frac{\tilde{J}_{ij\ell}}{L_i L_j} P'_\ell(\hat{\mathbf{L}}_i \cdot \hat{\mathbf{L}}_j) \mathbf{L}_j \quad (\text{B76})$$

where

$$\tilde{\mathcal{J}}_{ij\ell} = \mathcal{J}_{ij\ell} - \frac{\ell^2 \mathcal{J}_{ij\ell}^{\text{asympt}}}{(\ell+1)(\ell+2)} \quad (\text{B77})$$

$$\Omega_i^{\text{asympt}} = - \sum_{j\ell} \frac{\ell^2 \mathcal{J}_{ij\ell}^{\text{asympt}}}{(\ell+1)(\ell+2)L_i L_j} P'_\ell(\hat{\mathbf{L}}_i \cdot \hat{\mathbf{L}}_j) \mathbf{L}_j \quad (\text{B78})$$

and $\mathcal{J}_{ij\ell}^{\text{asympt}}$ is defined in Eq. (B71); note that the numerator $\ell^2 \mathcal{J}_{ij\ell}^{\text{asympt}}$ is independent of ℓ for overlapping or embedded orbits (Eq. B71) or proportional to α^ℓ for non-overlapping orbits (Eq. B64). We now use the generating function of the Legendre polynomial $(1-2\alpha z + \alpha^2)^{-1/2} = \sum_{\ell=0}^{\infty} \alpha^\ell P_\ell(z)$. Integrating this expression twice with respect to α and taking the even part in z gives the identity

$$\sum_{\ell > 0, \text{even}} \frac{\alpha^\ell}{(\ell+1)(\ell+2)} P_\ell(z) = \frac{g(\alpha, z) + g(\alpha, -z)}{2\alpha^2}, \quad (\text{B79})$$

where we have used the fact that $P_\ell(z)$ is an even function of z if ℓ is even, and odd if ℓ is odd. We have introduced the function

$$g(\alpha, z) = 1 - \frac{\alpha^2}{2} - \sqrt{1 + \alpha^2 - 2\alpha z} + (\alpha - z) \ln \left(\frac{\alpha - z + \sqrt{1 + \alpha^2 - 2\alpha z}}{1 - z} \right). \quad (\text{B80})$$

We differentiate Eq. (B79) with respect to z and then substitute in Eq. (B78) with $z = \hat{\mathbf{L}}_i \cdot \hat{\mathbf{L}}_j$. Next we replace $\mathcal{J}_{ij\ell}^{\text{asympt}}$ with the expressions from Eqs. (B64) and (B71) for non-overlapping and overlapping/embedded orbits. We obtain

$$\begin{aligned} \Omega_i^{\text{asympt}} = & - \sum_{\substack{j \in \text{overlapping} \\ / \text{embedded}}} \frac{8}{\pi^2 P_i M_\bullet} \frac{m_j}{M_\bullet} \frac{I^{(2)}(r_{p<}, r_{p>}, r_{a<}, r_{a>})}{a_j (1 - e_i^2)^{1/2}} g_2(1, \hat{\mathbf{L}}_i \cdot \hat{\mathbf{L}}_j) \hat{\mathbf{L}}_j \\ & - \sum_{j \in \text{non-overlapping}} \frac{2}{\pi P_i M_\bullet} \frac{m_j}{M_\bullet} \frac{[(1 + e_{\text{in}})(1 - e_{\text{out}})]^{3/2}}{[e_i e_j (1 - e_i^2)]^{1/2}} \frac{a_i r_{p,\text{out}}}{r_{a,\text{in}}^2} g_2\left(\frac{r_{a,\text{in}}}{r_{p,\text{out}}}, \hat{\mathbf{L}}_i \cdot \hat{\mathbf{L}}_j\right) \hat{\mathbf{L}}_j \end{aligned} \quad (\text{B81})$$

where $g_2(\alpha, z) \equiv \frac{1}{2} \frac{d}{dz} [g(\alpha, z) + g(\alpha, -z)]$ is a closed-form combination of elementary analytic functions²⁵. Since $\tilde{\mathcal{J}}_{ij\ell}$ decays to zero as $\ell \rightarrow \infty$ much more quickly than $\mathcal{J}_{ij\ell}$, using Eq. (B76) yields much more accurate results than (B73) if the sum over ℓ in the second term is truncated at $\ell_{\text{max}} \gg 1$.

As shown in Section 3.1, the dynamical interaction of each i - j pair is a precession of $\mathbf{K}_{ij} = (\mathbf{L}_i - \mathbf{L}_j)/2$ around their total angular-momentum vector $2\mathbf{J}_{ij} = \mathbf{L}_i + \mathbf{L}_j$ with angular velocity Ω_{ij} , while $\hat{\mathbf{L}}_i \cdot \hat{\mathbf{L}}_j$, $\|\mathbf{K}_{ij}\|$, and \mathbf{J}_{ij} are fixed. The angular velocity Ω_{ij} is obtained from Ω_i by replacing \mathbf{L}_j by $2\mathbf{J}_{ij}$ (Eqs. 13 and 17). Summing over ℓ gives asymptotically

$$\Omega_{ij}^{\text{asympt}} = \begin{cases} - \frac{4}{\pi^3 M_\bullet} \frac{I^{(2)}(r_{p<}, r_{p>}, r_{a<}, r_{a>})}{a_{\text{in}}^{3/2} a_{\text{out}}^{3/2} [(1 - e_{\text{in}}^2)(1 - e_{\text{out}}^2)]^{1/2}} g_2(1, \hat{\mathbf{L}}_i \cdot \hat{\mathbf{L}}_j) (\mathbf{L}_i + \mathbf{L}_j) & \text{overlapping, } r_{a,\text{in}} > r_{p,\text{out}}, \\ - \frac{1}{\pi^2 M_\bullet} \frac{r_{p,\text{out}}}{r_{a,\text{in}}^2} \frac{[(1 + e_{\text{in}})(1 - e_{\text{out}})]^{3/2}}{[a_{\text{in}} a_{\text{out}} (1 - e_{\text{in}}^2)(1 - e_{\text{out}}^2) e_{\text{in}} e_{\text{out}}]^{1/2}} g_2\left(\frac{r_{a,\text{in}}}{r_{p,\text{out}}}, \hat{\mathbf{L}}_i \cdot \hat{\mathbf{L}}_j\right) (\mathbf{L}_i + \mathbf{L}_j) & \text{non-overlapping, } r_{a,\text{in}} \leq r_{p,\text{out}}. \end{cases}$$

In practice, the high ℓ terms contribute most significantly if the mutual inclination I_{ij} is small or near π and if the orbits are overlapping or embedded²⁶, since then $g_2(1, \cos I) \simeq 1/(2I)$ or $1/[2(\pi - I)]$. For nearly parallel overlapping or embedded orbits, the instantaneous precession of i due to j in Eq. (B81) simplifies to

$$\Omega_i^{\text{asympt}} \approx - \frac{4}{\pi^2 P_i M_\bullet} \frac{m_j}{M_\bullet} \frac{I^{(2)}(r_{p<}, r_{p>}, r_{a<}, r_{a>})}{a_j (1 - e_i^2)^{1/2}} \frac{\hat{\mathbf{L}}_j}{I_{ij}} \quad \text{if } I_{ij} \ll 1 \text{ and if } i \text{ and } j \text{ are overlapping or embedded.} \quad (\text{B83})$$

For nearly coplanar orbits orthogonal to the z -axis, we may approximate $\hat{\mathbf{L}}_{iz} \approx 1$ and so $\hat{\mathbf{L}}_i \approx \hat{e}_z + \hat{L}_{xi} \hat{e}_x + \hat{L}_{yi} \hat{e}_y$. The angular-momentum vectors are approximately confined to a plane, and the mutual inclination is approximately the Euclidean distance between the angular-momentum vectors in the plane, $I_{ij} = \|\hat{\mathbf{L}}_i - \hat{\mathbf{L}}_j\|$. Thus,

$$\dot{\hat{\mathbf{L}}}_i \approx - \sum_j \frac{4}{\pi^2 P_i M_\bullet} \frac{m_j}{M_\bullet} \frac{I^{(2)}(r_{p<}, r_{p>}, r_{a<}, r_{a>})}{a_j (1 - e_i^2)^{1/2}} \frac{\hat{\mathbf{L}}_j \times \hat{\mathbf{L}}_i}{\|\hat{\mathbf{L}}_i - \hat{\mathbf{L}}_j\|} \quad \text{for a thin stellar disk of overlapping/embedded orbits.} \quad (\text{B84})$$

²⁵ For overlapping or embedded orbits $\alpha = 1$ and

$$\begin{aligned} g_2(1, z) &= \frac{1}{4} \left(\sqrt{\frac{2}{1-z}} - \sqrt{\frac{2}{1+z}} + \frac{1}{1 + \sqrt{(1-z)/2}} - \frac{1}{1 + \sqrt{(1+z)/2}} \right) + \frac{1}{2} \ln \left[\left(\frac{1 + \sqrt{(1+z)/2}}{1 + \sqrt{(1-z)/2}} \right) \sqrt{\frac{1-z}{1+z}} \right] \\ &= \frac{1}{4} \left(\frac{1}{s} + \frac{1}{1+s} + 2 \ln \frac{s}{1+s} \right) - \frac{1}{4} \left(\frac{1}{c} + \frac{1}{1+c} + 2 \ln \frac{c}{1+c} \right), \end{aligned} \quad (\text{B82})$$

where in the second line $s = \sin(I/2)$, $c = \cos(I/2)$, and $z = \cos I$. In particular for $0 < I \ll 1$, $s \approx I/2$, $c \approx 1$, and so $g_2(1, \cos I) \approx 1/(2I)$. Similar scaling relations apply if $I \approx \pi$.

²⁶ Note that $P'_\ell(1) = \ell(\ell+1)/2$ and $\mathcal{J}_{ij\ell}^{\text{asympt}} \propto \ell^{-2}$ for overlapping or embedded orbits.

These equations are similar to the equations of motion for a point vortex system on the sphere, where the torque is proportional to $\sum_j (\hat{\mathbf{L}}_j \times \hat{\mathbf{L}}_i) / \|\hat{\mathbf{L}}_i - \hat{\mathbf{L}}_j\|^2$.

B7 Summary

Now we can substitute the radial and the azimuthal integral (B8) into the interaction energy (B7).

For non-overlapping orbits, $r_{\text{pout}} > r_{\text{ain}}$,

$$H_{\text{RR}} = -\frac{Gm_{\text{in}}m_{\text{out}}}{a_{\text{out}}} - \frac{Gm_{\text{in}}m_{\text{out}}}{a_{\text{in}}a_{\text{out}}} \sum_{\ell=2}^{\infty} \frac{b_{\text{in}}^{\ell+1}}{b_{\text{out}}^{\ell}} P_{\ell}(0)^2 P_{\ell+1}(\chi_{\text{in}}) P_{\ell-1}(\chi_{\text{out}}) P_{\ell}(\cos I). \quad (\text{B85})$$

where $b_i = a_i \sqrt{1 - e_i^2}$ is the semiminor axis, $\chi_i = a_i/b_i = 1/\sqrt{1 - e_i^2}$ is the aspect ratio, and the sum is over even ℓ . For identical orbits, the generating function of the radial integral for each multipole is a combination of transcendental functions (Eq. B30), and the closed-form formula is a lengthy expression given by Eqs. (B33)–(B38). In the general case of overlapping or embedded orbits, we have derived the generating function of the radial integral in two parts S_{ℓ}^+ and S_{ℓ}^- . The generating function is a one-dimensional integral (B49)–(B50). Equivalent expressions for S_{ℓ}^+ are Eqs. (B48) or (B55). S_{ℓ}^- can be calculated with these equations by reversing the indices in \leftrightarrow out. The interaction energy is then

$$H_{\text{RR}} = -\frac{Gm_{\text{in}}m_{\text{out}}}{a_{\text{out}}} \sum_{\ell=0}^{\infty} P_{\ell}(0)^2 s_{\ell} \alpha^{\ell} P_{\ell}(\cos I). \quad (\text{B86})$$

where s_{ℓ} is related to $S_{\ell} = S_{\ell}^+ + S_{\ell}^-$ by Eq. (B12). Note that s_{ℓ} is dimensionless, and hence independent of the overall dimensional scale, and $s_{\ell} = 1$ for circular non-overlapping orbits. The sum over ℓ converges for all cases except for a set of measure zero. The asymptotic form of the multiplicative prefactor of $P_{\ell}(\cos I)$ is given in closed form by Eqs. (B64) and (B71) for non-overlapping and overlapping/embedded orbits respectively. The corresponding asymptotic precession rate is given by Eq. (B83).

APPENDIX C: RANDOM WALK ON A SPHERE

Here we derive the eigenfunctions and eigenvalues of the stochastic random walk on a unit sphere, as used in Section 4. Let us assume an initial probability $\rho_0(\mathbf{r})$, and that \mathbf{r} moves an angle α in a random direction on the sphere at each step of the walk. Thus, the probability density after the n^{th} step is set by the probability density of the preceding step as

$$\rho_n(\mathbf{r}) = \int_{S_2} d\mathbf{r}' p_{\mathbf{r},\mathbf{r}'} \rho_{n-1}(\mathbf{r}'). \quad (\text{C1})$$

where $p_{\mathbf{r},\mathbf{r}'}$ is the transition probability between two points \mathbf{r} and \mathbf{r}' . The transition probability must vanish if $\cos \gamma \equiv \mathbf{r} \cdot \mathbf{r}'$ differs from $\mu \equiv \cos \alpha$, and must satisfy $\int_{S_2} d\mathbf{r}' p_{\mathbf{r},\mathbf{r}'} = 1$ for all \mathbf{r} to conserve probability. These conditions require that

$$p_{\mathbf{r},\mathbf{r}'} = \frac{1}{2\pi} \delta(\cos \gamma - \mu). \quad (\text{C2})$$

Next we will use the following identities of the Legendre polynomials,

$$\delta(\cos \gamma - \mu) = \sum_{\ell=0}^{\infty} \frac{2\ell+1}{2} P_{\ell}(\cos \gamma) P_{\ell}(\mu), \quad (\text{C3})$$

$$P_{\ell}(\cos \gamma) = \frac{4\pi}{2\ell+1} \sum_{m=-\ell}^{\ell} Y_{\ell m}(\mathbf{r}) Y_{\ell m}^*(\mathbf{r}'). \quad (\text{C4})$$

where $Y_{\ell m}(\mathbf{r})$ are orthonormal spherical harmonics²⁷. Substituting into Eq. (C2) gives

$$p_{\mathbf{r},\mathbf{r}'} = \sum_{\ell=0}^{\infty} \sum_{m=-\ell}^{\ell} P_{\ell}(\mu) Y_{\ell m}(\mathbf{r}) Y_{\ell m}^*(\mathbf{r}'). \quad (\text{C6})$$

Next we substitute in Eq. (C1):

$$\rho_n(\mathbf{r}) = \sum_{\ell=0}^{\infty} \sum_{m=-\ell}^{\ell} P_{\ell}(\mu) Y_{\ell m}(\mathbf{r}) \int_{S_2} d\mathbf{r}' Y_{\ell m}^*(\mathbf{r}') \rho_{n-1}(\mathbf{r}'). \quad (\text{C7})$$

²⁷ We use the definition in Eq. (B1) for $Y_{\ell m}(\mathbf{r})$ which satisfies

$$\int_{S_2} Y_{\ell m}(\mathbf{r}) Y_{\ell' m'}^*(\mathbf{r}) d\mathbf{r} = \delta_{\ell \ell'} \delta_{m m'} \quad \text{if } \ell \geq 0 \text{ and } -\ell \leq m \leq \ell \text{ and similarly for } \ell' \text{ and } m'. \quad (\text{C5})$$

In particular, if $\rho_{n-1}(\mathbf{r}') = Y_{LM}(\mathbf{r}')$ for some $L \geq 0$ and $-L \leq M \leq L$, then $\rho_n(\mathbf{r}) = P_L(\mu)Y_{LM}(\mathbf{r})$ by the orthonormal property of the spherical harmonics. Thus the spherical harmonics are eigenfunctions of the linear operator (C1) or (48) with eigenvalue $P_L(\mu)$.

APPENDIX D: TORQUE PARAMETER

If each star in the cluster has the same semimajor axis and the cluster is spherical, the dimensionless torque parameter for star i , defined in Eq. (73) simplifies to

$$\beta_T = \frac{2\pi a}{Gm_i m_{\text{RMS}}} \left\langle \sum_{\ell} \frac{\ell(\ell+1)}{2\ell+1} \mathcal{J}_{ij\ell}^2 \right\rangle_j^{1/2}, \quad (\text{D1})$$

where the average is over the distribution of stars j . If there is a distribution of semimajor axes, we replace $N \rightarrow dN/d \ln a$ —as we did in going from Eq. (71) to Eq. (74) or from Eq. (79) to (81)—so Eq. (D1) becomes

$$\beta_T = \frac{2\pi a}{Gm_i m_{\text{RMS}}} \left(\frac{d \ln N}{d \ln a} \right)^{-1/2} \left\langle \sum_{\ell} \frac{\ell(\ell+1)}{2\ell+1} \mathcal{J}_{ij\ell}^2 \right\rangle_j^{1/2}. \quad (\text{D2})$$

Here $a \equiv a_i$. Now substitute $\mathcal{J}_{ij\ell}$ from Eq. (10). If the number of stars in the range $[a, a + da]$, $[e, e + de]$, and $[m, m + dm]$ is $dN = 4\pi a^2 n(a, e, m) da de dm$ then

$$\beta_T = \frac{2\pi a}{m_{\text{RMS}} (dN/d \ln a)^{1/2}} \left\{ \sum_{\ell > 0, \text{even}} \frac{\ell(\ell+1)}{2\ell+1} [P_{\ell}(0)]^4 \int_0^{\infty} dm' \int_0^1 de' \int_0^{\infty} da' 4\pi (a')^2 n(a', e', m') \frac{[\min(a, a')]^{2\ell}}{[\max(a, a')]^{2\ell+2}} \right. \\ \left. \times (m')^2 s_{\ell}^2(\alpha, e_{\text{in}}, e_{\text{out}}) \right\}^{1/2} \quad (\text{D3})$$

Here $s_{\ell}^2(\alpha, e_{\text{in}}, e_{\text{out}})$ is defined in Eq. (7), $\alpha = \min(a, a')/\max(a, a')$, $(e_{\text{in}}, e_{\text{out}}) = (e', e)$ if $a' \leq a$, and $(e_{\text{in}}, e_{\text{out}}) = (e, e')$ for $a' \geq a$. Now let us assume that the a - e - m distribution is separable as $n(a, e, m) = f(m)f(e)n(a)$, where the distribution functions $f(m)$ and $f(e)$ have unit integrals. Changing integration variable to α we get

$$\beta_T = 2\pi \left\{ \frac{1}{n(a)} \sum_{\ell > 0, \text{even}} \frac{\ell(\ell+1)}{2\ell+1} [P_{\ell}(0)]^4 \int_0^1 de' f(e') \int_0^1 d\alpha [\alpha^2 n(a\alpha) s_{\ell}^2(\alpha, e', e) + \alpha^{-2} n(a/\alpha) s_{\ell}^2(\alpha, e, e')] \alpha^{2\ell} \right\}^{1/2} \quad (\text{D4})$$

For a power-law density profile $n(a) \propto a^{-\gamma}$,

$$\beta_T = 2\pi \left\{ \sum_{\ell > 0, \text{even}} \frac{\ell(\ell+1)}{2\ell+1} [P_{\ell}(0)]^4 \int_0^1 de' f(e') \int_0^1 d\alpha [\alpha^{2-\gamma} s_{\ell}^2(\alpha, e', e) + \alpha^{\gamma-2} s_{\ell}^2(\alpha, e, e')] \alpha^{2\ell} \right\}^{1/2} \quad (\text{D5})$$

Generally, the terms in the sum scale as ℓ^{-3} for overlapping or embedded eccentric orbits, and $\ell^{-3}\alpha^{2\ell}$ for eccentric non-overlapping orbits. The lowest order (i.e. quadrupole) terms dominate β_T in a spherical cluster. Note that β_T is independent of the stellar mass m , the RMS stellar mass m_{RMS} and the semimajor axis a (for a power-law density), but it may depend on the exponent of the power law γ , the eccentricity e of the test star, and the distribution $f(e)$ of the eccentricities of the cluster stars. For circular orbits $e = e' = 0$, $s_{\ell}(\alpha, 1, 1) = 1$ and we find that β_T is between 1.507 and 1.526 if $1 < \gamma < 3$. We find a weak γ dependence for general eccentric orbits as well. For eccentric overlapping or embedded orbits we find that β_T is systematically smaller for all $1 < \gamma < 3$ and $f(e')$ as shown in Figure 6.